UNESP – UNIVERSIDADE ESTADUAL PAULISTA
CAMPUS DE PRESIDENTE PRUDENTE
FACULDADE DE CIÊNCIAS E TECNOLOGIA
PROGRAMA DE PÓS-GRADUAÇÃO EM CIÊNCIAS CARTOGRÁFICAS

ANA LUCIA CHRISTOVAM DE SOUZA

GNSS SINGLE FREQUENCY IONOSPHERIC MODEL FOR EQUATORIAL PLASMA BUBBLES DETECTION IN THE BRAZILIAN REGION

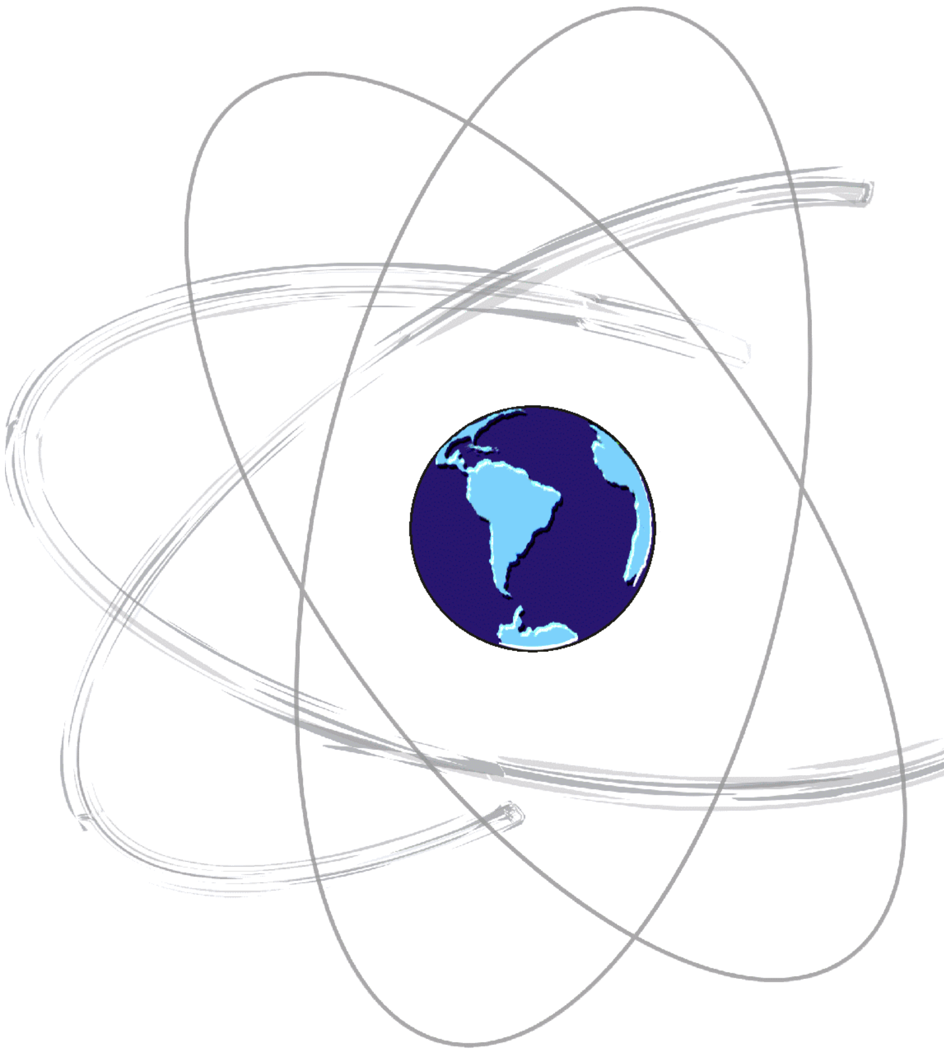

PRESIDENTE PRUDENTE
2023

ANA LUCIA CHRISTOVAM DE SOUZA

GNSS SINGLE FREQUENCY IONOSPHERIC MODEL FOR EQUATORIAL PLASMA BUBBLES DETECTION IN THE BRAZILIAN REGION

Thesis presented to "Programa de Pós-Graduação em Ciências Cartográficas" at São Paulo State University – UNESP School of Technology and Sciences.

Supervisor: Dr. Paulo de Oliveira Camargo
Co-Supervisor: Dr. Fabricio dos Santos Prol
Co-Supervisor: Dr. Manuel Hernández-Pajares

PRESIDENTE PRUDENTE

2023

S729g

Souza, Ana Lucia Christovam de
GNSS Single Frequency model for equatorial plasma bubbles detection in the Brazilian region / Ana Lucia Christovam de Souza. -- Presidente Prudente, 2023
94 f.

Tese (doutorado) - Universidade Estadual Paulista (Unesp), Faculdade de Ciências e Tecnologia, Presidente Prudente
Orientador: Paulo de Oliveira Camargo
Coorientador: Fabricio dos Santos Prol

1. GNSS. 2. Ionospheric Modeling. 3. Ionospheric plasma bubbles. 4. TEC single frequency. I. Título.

Sistema de geração automática de fichas catalográficas da Unesp. Biblioteca da Faculdade de Ciências e Tecnologia, Presidente Prudente. Dados fornecidos pelo autor(a).

Essa ficha não pode ser modificada.

unesp **UNIVERSIDADE ESTADUAL PAULISTA**

Câmpus de Presidente Prudente

CERTIFICADO DE APROVAÇÃO

TÍTULO DA TESE: GNSS SINGLE FREQUENCY IONOSPHERIC MODEL FOR EQUATORIAL PLASMA BUBBLES DETECTION IN THE BRAZILIAN REGION

AUTORA: ANA LUCIA CHRISTOVAM DE SOUZA
ORIENTADOR: PAULO DE OLIVEIRA CAMARGO
COORIENTADOR: MANUEL HERNANDEZ PAJARES
COORIENTADOR: FABRICIO DOS SANTOS PROL

Aprovada como parte das exigências para obtenção do Título de Doutora em Ciências Cartográficas, área: Aquisição, Análise e Representação de Informações Espaciais pela Comissão Examinadora:

Prof. Dr. PAULO DE OLIVEIRA CAMARGO (Participaçao Presencial)
Departamento de Cartografia / Faculdade de Ciencias e Tecnologia de Presidente Prudente

Prof. Dr. JOÃO FRANCISCO GALERA MONICO (Participaçao Presencial)
Departamento de Cartografia / Faculdade de Ciencias e Tecnologia de Presidente Prudente

Dr. ALISON DE OLIVEIRA MORAES (Participaçao Virtual)
Centro Técnico Aeroespacial / Instituto de Aeronáutica e Espaço

Prof. Dr. MARCIO TADEU DE ASSIS HONORATO MUELLA (Participaçao Virtual)
Instituto de Pesquisa e Desenvolvimento / Universidade do Vale do Paraíba

Dr. JONAS RODRIGUES DE SOUZA (Participaçao Virtual)
Coordenação Geral de Ciências Espaciais e Atmosféricas / Instituto Nacional de Pesquisas Espaciais

Presidente Prudente, 16 de junho de 2023

ACKNOWLEDGMENTS

I would like to thank my supervisor, Prof. Paulo O. Camargo, who was the main motivator of this research. I would also like to thank Fabricio S. Prol from Finnish Geospatial Research Institute (FGI) for their support and contributions as co-supervisors. I am also grateful to Prof. Manuel Hernández-Pajares from Universitat Politècnica de Catalunya (UPC) for kindly sharing his knowledge about ionospheric modeling and geodetic positioning during the internship supervision.

This study was financed in part by the Coordenação de Aperfeiçoamento de Pessoal de Nível Superior - Brasil (CAPES) - Finance Code 001. Ph.D. scholarship from 03/2019 to 02/2023 (Grant: 88882.433958/2019-01) and from 03/2023 to 05/2023 (Grant: 88887.817768/2023-00). Internship abroad at Universitat Politècnica de Catalunya Capes-PrInt (PrInt - *Programa Institucional De Internacionalização*) from 11/2022 to 01/2023 (Grant: 88887.569761/2020-00).

This works was also supported by:

GNSS in Support of Air Navigation (INCT GNSS-NavAer), funded by CNPq (Grant: 465648/2014-2), FAPESP (Grant: 2017/50115-0) and CAPES (Grant: 88887.137186/2017-00).

Postgraduate program in Cartographic Sciences, São Paulo State University (UNESP) – School of Technology and Sciences.

Department of Mathematics at the Universitat Politècnica de Catalunya, Barcelona, Spain.

ABSTRACT

The ionospheric layer can be considered difficult to model due to the high variation in electron density presents in the upper atmosphere. In regions of low latitude, such as Brazilian region, the ionosphere presents a peculiar dynamic, considerably affecting communication systems and global navigation satellite systems (GNSS). Total Electron Content (TEC) is the main parameter capable of describing the ionospheric layer. Therefore, ionospheric models based on TEC values become critical for monitoring space weather and the ionospheric layer. However, in low latitude regions, the performance of these models degrades due to the high sensitivity of the global positioning system (GPS) L2 frequency to ionospheric scintillation. In an effort to overcome this problem, this thesis investigates the potential of utilizing only GPS L1 frequency for imaging the ionospheric bubbles during ionospheric scintillation. Two methods for estimating TEC using single frequency are presented. The first one is based on the calibration method, i.e., information retrieved by external ionospheric models are used to correct the TEC using single frequency measurements. The second one is based on independent regional ionospheric model to calibrate GPS using single frequency measurements. Both methods successfully detected plasma bubbles by mapping TEC using single frequency. In addition, single frequency model presented similar accuracy to the dual frequency models and, at the same time, provided less observations affected by ionospheric scintillations. These results demonstrate the feasibility of using single frequency GNSS data to develop ionospheric models and to improve GNSS positioning in low latitudes.

Keywords: Ionosphere; spherical harmonics; TEC; single frequency; plasma bubbles; airglow images.

RESUMO

A camada ionosférica pode ser considerada de difícil modelagem devido à alta variação na densidade de elétrons presente na atmosfera superior. Em regiões de baixa latitude, como a região brasileira, a ionosfera apresenta uma dinâmica peculiar, afetando consideravelmente os sistemas de comunicação e os sistemas GNSS (Global Navigation Satellite System). O Conteúdo Total de Elétrons (TEC) é o principal parâmetro capaz de descrever a camada ionosférica. Portanto, os modelos ionosféricos baseados em valores de TEC tornam-se essenciais para o monitoramento do clima espacial e da camada ionosférica. No entanto, em regiões de baixa latitude, o desempenho desses modelos é prejudicado devido à alta sensibilidade da frequência L2 do GPS (Global Positioning System) à cintilação ionosférica. Em um esforço para superar esse problema, esta tese investiga o potencial de utilizar apenas a frequência L1 do GPS para obter imagens das bolhas ionosféricas durante a cintilação ionosférica. São apresentados dois métodos para estimar o TEC utilizando simples frequência. O primeiro método é baseado na calibração do TEC, ou seja, as informações obtidas por modelos ionosféricos externos são usadas para corrigir o TEC usando medições de simples frequência. O segundo método, baseia-se em um modelo ionosférico regional independente para calibrar o GPS usando medições de simples frequência. Ambos os métodos detectaram com sucesso bolhas de plasma mapeando o TEC usando frequência única. Além disso, o modelo de simples frequência apresentou precisão semelhante à dos modelos de dupla frequência e, ao mesmo tempo, forneceu menos observações afetadas pelas cintilações ionosféricas. Esses resultados demonstram a viabilidade do uso de dados GNSS de simples frequência para desenvolver modelos ionosféricos e melhorar o posicionamento GNSS em baixas latitudes.

CONTENTS

CHAPTER 1
INTRODUCTION

CHAPTER 2
ASSESSMENT OF GPS POSITIONING PERFORMANCE USING DIFFERENT SIGNALS IN THE CONTEXT OF IONOSPHERIC SCINTILLATION

CHAPTER 3
SINGLE FREQUENCY TEC CALIBRATION TO DETECT EQUATORIAL PLASMA BUBBLES

CHAPTER 4
PPP AT LOW LATITUDES WITH IONOSPHERIC MODEL EXCLUSIVELY BASED ON SINGLE FREQUENCY GNSS MEASUREMENTS

CHAPTER 5
PPP AT LOW LATITUDES WITH IONOSPHERIC MODEL EXCLUSIVELY BASED ON SINGLE FREQUENCY GNSS MEASUREMENTS

CHAPTER 6
FINAL REMARKS

CHAPTER 1
INTRODUCTION

1 OVERVIEW AND MOTIVATION

The ionosphere is a layer of the Earth's atmosphere, located at approximately 50 to 1000 km altitude, characterized by a high concentration of ionized particles. The propagation of radio signals through the ionosphere with irregularities in the electron density distribution may produce phase and amplitude scintillations in radio frequency (RF) signals (Aarons, 1982; Yeh and Liu, 1982). These scintillations degrade the accuracy of navigation and positioning applications based on Global Navigation Satellite Systems (GNSS). Several authors point out (Skone et al., 2001; Sreeja et al. 2012; Vani et al. 2019; Guo et al 2019; 2020) that rapid phase variations lead to a higher probability of cycle slip. Depending on its severity, scintillation is capable of leading to the loss of satellite signal tracking. These extreme phenomena are more usual near the equatorial and low-latitude regions. In such regions, several electrodynamics processes may lead to large-scale plasma depletions in the F region of the ionosphere, called as Equatorial Plasma Bubbles (EPBs). The EPBs are large-scale ionospheric structures characterized by depleted electron density in comparison to the surrounding ionosphere, developed after the local sunset at the magnetic equator (Li et al., 2021; Bhattacharyya, 2022). The pre-reversal enhancement in the evening zonal electric field causes an increase in the eastward electric field that causes initial plasma depletions to rise to higher altitudes. This uplift contributes to an increase in the vertical growth of the magnetic aligned plasma-depleted structures formed by the Rayleigh–Taylor instability mechanism. (de Paula et al. 2007; Kelley, 2009; Hasse et al. 2010; Abdu 2016; Muella et al. 2017; Moraes et al., 2018b; Barros et al. 2018; Bhattacharyya, 2022). During the development of the EPBs, they tend to extend to latitudes of larger background plasma density in the Equatorial Ionization Anomaly (EIA), located at around 15°- 20° north and south of the magnetic equator (Muella et al., 2017; Li et al., 2021).

Several researches describing the dynamics of the ionosphere and the ionospheric scintillation-producing irregularities are supported by GNSS data(for example see Mannucci et al. 1993; de Paula et al., 2007; Haase et al. 2010; Spogli et al., 2013; Guo et al., 2019; Macho et al., 2022). The GNSS simultaneous information in multiple frequencies can be used as a tool for ionospheric sounding, due to the dispersive medium of the ionosphere. From GNSS data, it is possible to perform ionospheric modeling using the total electron content (TEC) parameter capable to describe the properties of the ionosphere. TEC is the integral of electron density along the signal path counted passing through the ionosphere. The TEC is calculated in a column along a signal path between a satellite based GNSS transmitter and a receiver, typically ground-based (Seeber, 2003; Leick, 2004). Therefore, if the signal path from transmitter to receiver is known, the differential delay by two signals can be used to derive the TEC along the signal path. As the ionospheric delay is in very good approximation (better than 99.9%) proportional to TEC (see for instance Hernández-Pajares et al. 2014), combinations of signal frequencies and GNSS observables can be performed to obtain a relationship with ionospheric delay. Considering dual frequency measurements, TEC can be obtained using a linear combination, since the non-frequency dependent terms are cancelled out. The eliminated terms in the geometric-free combination are the geometric distance between the receiver and the satellite, the satellite and receiver clocks, and the tropospheric delay. If only single frequency is available, TEC can be eliminated or estimated using combinations between GNSS observables, for instance, the GRoup and Phase Ionosphere Correction (GRAPHIC), proposed by Yunck (1992), and the Code-Minus-Carrier (CMC) proposed by Xia (1992). Both combination exploits the opposite sign of the ionospheric error in the pseudorange and carrier-phase. The GRAPHIC combination is computed by the arithmetic mean of the code and carrier phases, removing the TEC term; while the CMC is given by differencing the pseudorange and carrier-phase measurements, all geometry-dependent components are cancelled. However, the main problem about these combinations are the multipath and noise of the pseudorange. It is worthwhile to highlight that the dual frequency ionosphere-free combinations for pseudorange and carrier-phase are only constructed from observations of the same type. In contrast to the GRAPHIC and CMC combinations, the dual frequency combinations are constructed from different observables, they maintain their basic characteristic properties and can be processed similarly to the original uncombined observations except for the increased noise (Teunissen; Montenbruck, 2017; Hernández-Pajares et al, 2018).

Techniques and algorithms are being continuously developed and evaluated to improve the accuracy and resolution of TEC estimates. Accurately determining TEC values continues to be a challenging, particularly in low latitude regions and especially during ionospheric scintillation events. Prol et al. (2018a), for instance, evaluated the performance of TEC calibration procedures by analyzing the improvement in single frequency PPP (Precise Point Positioning) considering several latitudes. The authors have found a worse PPP performance in low latitudes, mainly due to the ionospheric variability associated with the EIA and ionospheric scintillation. According to Moraes et al. (2018b) the distribution of plasma bubble irregularities in relation to the geomagnetic field configuration can amplify the effects of scintillation. In low latitude regions, such as the Brazilian region, the geomagnetic field configuration, characterized by a large magnetic declination angle, provides a particular and favorable condition for the occurrence of such effects. The authors showed a correlation between the intensified scintillation occurrence and Global Positioning System (GPS) signals that propagated through plasma bubbles aligned to the magnetic field's direction. In addition, the authors showed large PPP errors due to these events in such regions. Several authors (Delay et al. 2015, Spogli et al. 2016; Xiong et al.2016; Moraes et al. 2017; Souza et al. 2022) showed a close relationship between the occurrences of EPBs and severe ionospheric scintillations at different radio bands at low latitudes. In such regions, the lack of TEC data especially obtained using dual frequency measurements, can be associated with disruptions in the received signal caused by ionospheric plasma bubbles under ionospheric scintillation, which are zones with high electron density variability (Li et al. 2021). During ionospheric scintillation, the GPS L2 signal presents greater ionospheric interference when compared to the GPS L1 signal. Therefore, during the presence of ionospheric scintillation, it is expected that a single frequency can provide better alternative for ionospheric plasma bubbles imaging. Since the single GPS L1 frequency is supposed to minimize the loss of synchronism, ionospheric models based on GPS L1 frequency should improve the imaging of ionospheric bubbles.

To enhance the imaging of ionospheric bubbles during ionospheric scintillation in low latitude regions, this work aims to develop and analyze a regional single frequency ionospheric model for TEC estimation.

1.1 Objectives

The main goal of this research is to develop a methodology capable to detect equatorial plasma bubbles using only GPS single frequency measurements. In this regard, the Ph.D. research has the following specific objectives:

(1) investigate which GPS signal frequency is the best one to detect equatorial plasma bubble;

(2) develop an ionospheric regional model exclusively based on single-frequency GPS measurements;

(3) understand if plasma bubbles can be detected using single frequency GPS measurements;

(4) verify if the single frequency precise point positioning (PPP) based on single frequency ionospheric regional model can provide a comparable level to those ionospheric models obtained by dual frequency GPS measurements.

1.2 Content and Contributions

The thesis can be summarized in two purposes: First, we evaluate and understand which GPS signal has the best capability of ionospheric bubble imaging and whether it is possible to detect the ionospheric plasma bubbles using only a single frequency GNSS measurements. Second, we present an ionospheric model for the Brazilian region using a single frequency and evaluate its quality.

Chapter 2 shows the study developed by Souza et al. (2022). The authors presented an assessment of GPS positioning performance using different signals in the context of ionospheric scintillation. Chapters 3 and 4 are devoted to investigating the feasibility of detecting ionospheric plasma bubbles using GNSS single frequency measurements, i.e., it answers if it is possible to detect ionospheric plasma bubbles using single frequency TEC maps. In Chapter 3, we present a technique for TEC single frequency calibration, and we use a previously estimated TEC to generate ionospheric maps. As a result, ionospheric plasma bubbles are successfully detected using single frequency data. However, the calibration method uses external ionospheric models based on dual frequency data. Therefore, in order to use only single frequency data in all steps, Section 4, also summarized in Christovam et al. (2023a), shows a methodology based on a regional model to calibrate GNSS single frequency measurements and derive ionospheric maps with no external information. In Chapter 5, Christovam et al. (2023b) present an evaluation of a new regional model by means of single frequency precise point positioning (PPP), comparing the positioning results against the correction using dual-frequency GPS signals, as well as compared to the corrections provided by global ionospheric models produced by the international GNSS service (IGS).

CHAPTER 2

ASSESSMENT OF GPS POSITIONING PERFORMANCE USING DIFFERENT SIGNALS IN THE CONTEXT OF IONOSPHERIC SCINTILLATION

2 SCOPE

This Chapter presents the results of a quantitative analysis of the scintillation amplitude of GPS signals at L1, L2, and L5 frequencies (Souza et al. 2022). This work aims to evaluate the impact of the ionospheric scintillation on the different GPS frequencies.

2.1 Overview

The atmosphere has a great influence on Global Navigation Satellite Systems (GNSS) signal propagation. The GNSS signals that pass through the Earth's atmosphere are disrupted, especially due to events occurring in the ionospheric layer (Seeber, 2003; Zolesi and Cander 2014). The error caused by the ionospheric layer is directly proportional to the Total Electron Content (TEC) and inversely proportional to the squared frequency. Therefore, higher frequencies are supposed to be less affected by the ionosphere when compared with lower frequencies (Zolesi and Cander 2014; Langley et al., 2017).

Ionospheric scintillation is caused by spatial and temporal variations in the electron density of the ionospheric layer. This effect is defined as rapid changes in the phase and/or amplitude of a radio signal as it propagates through small-scale plasma density irregularities in the ionosphere (Conker et al., 2003). The scintillation is related to smaller-scale irregularities coexisting with the Equatorial Plasma Bubbles (EPBs) (de Paula et al.,2007; Moraes et al., 2017). The ionospheric scintillation in general occurs after sunset until midnight, sometimes also extending for a few hours in the post-midnight period (Conker et al., 2003; Seeber, 2003).

The occurrence and intensity of scintillations vary according to several factors, such as solar activity, the epoch of the year, geographic location, and local time. Scintillation occurs dominantly at high latitudes and between equatorial and low latitudes. (Walter et al., 2010; Vani et al., 2017). As the Brazilian region is within the equatorial and low latitudes, ionospheric scintillation is a serious threat to satellite navigation and communication. Severe ionospheric scintillation can cause errors and losses of lock in GNSS positioning, resulting in degraded performance and signal unavailability (Conker et al., 2003) (Conker et al., 2003). The scintillation effect can be measures by some indices, such as S_4 and Sigma-phi. S_4 is a scintillation intensity index which measures the relative magnitude of amplitude fluctuations. The S_4 index is the standard deviation of the signal strength, normalized by its mean. Sigma-phi is a phase scintillation index, which measures the magnitude of carrier phase fluctuations (Walter, 2010).

As previously mentioned, the ionospheric error is directly proportional to TEC and inversely proportional to the squared frequency, so it is expected that the severity of ionospheric effects, such as ionospheric scintillation, follows the same relationship with signal frequency. The GPS modernization program introduced two new civil navigation signals, on L2 (L2C) and L5. In this case, the new navigation signals, which have lower frequencies, would be more susceptible to the ionospheric effects compared to the L1 signal. The same performance from GPS L1 frequency cannot directly be transferred to the new signals that use different frequencies, mainly in low latitudes due to scintillation.

Several studies have been conducted in this context. Usually, the S_4 scintillation index is analyzed on the GNSS primary frequencies (for instance, the GPS L1 frequency). However, these indices can also be estimated on the other available GNSS frequencies. Hegarty et al. (2001) and Peng et al. (2011) defined functions that allow the scintillation indices to be mapped from the L1 frequency to obtain an expected value at L2 and L5 frequencies. Delay et al. (2015) presented a statistical analysis of GPS tracking performance under ionospheric scintillation using the S_4 index for L1, L2, and L5 frequencies. The results indicated a higher probability of signal loss at lower frequencies than at higher ones. Moraes et al. (2017) conducted a study to analyze the variability of low latitude ionospheric amplitude and phase scintillation detected by a triple-frequency GPS receiver. Based on an empirical quantification, the results showed the frequency dependence of scintillation, indicating that the lower frequencies L2 and L5 suffer more intense scintillation than the L1 signal.

Considering the new GPS signals performance on positioning, Engel (2008) evaluated the theoretical performance of GPS signals in terms of positioning accuracy. The author showed that when using a single frequency, the positioning accuracy is almost the same for all satellite signals, with L2 and L5 signals leading to worse performance than the L1 signal. Andrade and Alves (2016) analyzed static and kinematic positioning improvement obtained by the introduction of the GPS new signals L2 and L5. The results showed that the use of new frequencies causes faster convergence on kinematic positioning. The improvement rate in the positioning using the three frequencies was about 61% compared to a single frequency (L1).

Considering the current availability of the new signals, it is possible to perform a more detailed analysis of the dispersive behavior of the ionospheric layer. In addition, the new signals can be used to improve the positioning solution, so it is necessary to evaluate how they are influenced by scintillation and which signal is less affected. In this context, this Chapter presents a quantitative analysis of the impact of ionospheric amplitude scintillation on GPS frequencies, with a focus on low-latitude regions. Moreover, since ionospheric scintillation can potentially reduce positioning accuracy, we offer an assessment of GPS Precise Point Positioning (PPP) at L1, L2, and L5 frequencies.

2.2 Methodology

The experiments used data from the São José dos Campos (SJCE) station (23.21° S, 45.95° W), located near the southern crest of the equatorial ionization anomaly (EIA). This region is known for the occurrence of intense amplitude scintillations, which are associated with the heightened background electron density resulting from the influence of the Equatorial Ionization Anomaly (EIA). The SJCE station has a triple-frequency (L1, L2, and L5) receiver (Septentrio PolaRxS). The data were continuously collected for a period of 30 days, from November 3 to December 3, 2014. This time frame coincided with a high occurrence of scintillation due to increased ionospheric activity influenced by the maximum of solar cycle 24.

The parameter used was the amplitude scintillation index (S_4), which is the main statistical measure indicating the intensity of the amplitude scintillations. It was considered the same limits used by Muella (2009) for the S_4 index classification: weak level $0.2 < S_4 \leq 0.4$; moderate level $0.4 < S_4 \leq 0.6$; strong level $0.6 < S_4 \leq 1.0$; and saturated level $1.0 < S_4 \leq 1.4$. According to Muella (2009), saturated levels can be attributed to the effects of multiple scattering and means that the S_4 is not due to a single scatter of the radio wave. The S_4 index was obtained using the ISMR Query Tool (Vani et al., 2017). The S_4 measurements were taken at the three GPS frequencies: L1 (1575.42 MHz), L2 (1227.60 MHz), and L5 (1176.45 MHz). The values were limited to measurements from satellites with elevation angle higher than 20°, considered above the level of noise and multipath effects.

For the PPP experiments, the data were processed in kinematic and static modes using the online software CSRS-PPP (Canadian Spatial Reference System – Precise Point Positioning) developed by NRCan (Natural Resources Canada) available in <https://webapp.geod.nrcan.gc.ca/geod/tools-outils/ppp.php>. We used Receiver Independent Exchange Format (RINEX v.2.11) files with 24 hours of data, only GPS satellites, with a cutoff angle using 20° and 15 seconds sampling rate. It is important to emphasize that there is a difference between the number of satellites that provide the new signals (L2C and L5), due to the different generations of GPS satellites currently available. During the analyzed period, 31 satellites transmitted L1 signal, 15 transmitted L2C, and 8 satellites transmitted L5. Considering the number of satellites tracked per epochs transmitting L2C signal (~5 satellites), and the ones transmitting L2P signal (~8 satellites), the L2P was used for the positioning assessment. The kinematic positioning processing was performed using 5 configurations: L1 signal (L1C), L2P signal (L2P), L1-L2P signals (L1C and L2P), L1-L5 signals (L1C and L5) and L1-L2P-L5 signals (L1C, L2P and L5). The static mode was processed with the three frequencies and used as reference values. The editions of the RINEX files were performed using TEQC (Translation, Editing and Quality Checking) software from UNAVCO (Estey and Meertens, 1999). The single frequency positioning using the L5 signal was not possible due to the low number of satellites transmitting L5 frequency or a limitation in the software used. Results from the kinematic positioning in each configuration were compared to the static positioning. With the discrepancies obtained from the results of the kinematic positioning and the reference values, the root mean square error (RMSE) was obtained.

2.3 Results and Discussion

2.3.1 Quantitative analysis of the ionospheric scintillation impact on GPS frequencies

In order to show the behavior of the S_4 index for each GPS signal frequency, a visual comparison of the index values for each frequency is presented in Figure 2.1. It is worth highlighting that, for the chosen period, just three satellites had data collected on the L5 frequency with a higher number of epochs (PRN 24, PRN25 and PRN 27).

Figure 2.1– S_4 index at L1, L2 and L5 signals on November 27, 2014 for PRN 24 (top panel), PRN 25 (middle panel) and PRN 27 (bottom panel).

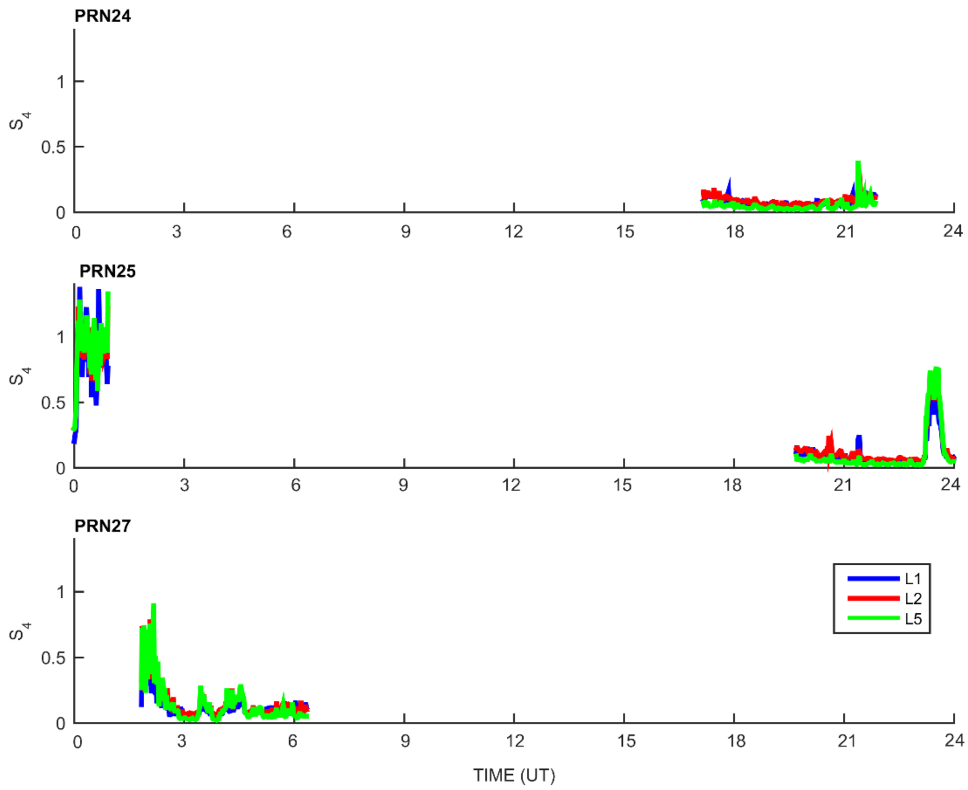

According to Figure 2.1, in all satellites, the difference between L1, L2 and L5 signals is small during the undisturbed conditions. However, at the peak of the scintillation events, the difference between the three signals becomes larger. Considering the PRN 24, the data were collected from ~17h – 22h UT, in which there was no presence of ionospheric scintillation, with S_4 values lower than 0.2. The PRN 25 presented two periods of collected data (~ 0h – 1h UT and 20h – 24h UT). In the first period, the scintillation level can be classified as moderated to a saturated level, the S_4 index varied from 0.6 to 1.4. The second period could be classified as undisturbed conditions until 23h UT, with values smaller than 0.2, after this period, the values increased, leading to a moderate scintillation level classification, considering the L1 signal and strong scintillation level for the L5 signal. In PRN 27, the data were collected from period ~2h – 7h UT, the scintillation level can be considered weak to strong, the values with index values were between 0.2 and 0.8 until the values decrease to an undisturbed level. Summarizing the S_4 behavior for each frequency, when the scintillation is classified as weak to strong levels, the data from the L1 frequency are less affected when compared to the other GPS frequencies. This behavior is observed when there are long continuous data and the ionospheric scintillation is classified as weak to strong levels. This behavior is shown in Figure 2.1(middle panel) in the second period of data. The L5 signal was classified as strong while the L1 was classified moderated level. Considering all the days selected, indices presented similar behavior under ionospheric scintillation, data from L1 frequency was less affected, when compared to L2 and L5 frequencies.

In order to show the influence of the scintillation in the S_4 values Figure 2.2 shows one example of the slant TEC estimated and the S_4 values at the L1, L2 and L5 signals for PRN 25 on November 27, 2014 (DOY 331). The slant TEC was obtained using calibration procedures such as Ciraolo et al. (2007) and Prol et al. (2018a).

Figure 2.2 – Comparison between STEC and S_4 during plasma bubble occurrence for PRN 25 on November 27, 2014; Top panel correspond to STEC values and the bottom panel represents S_4 values for L1, L2 and L5 signals.

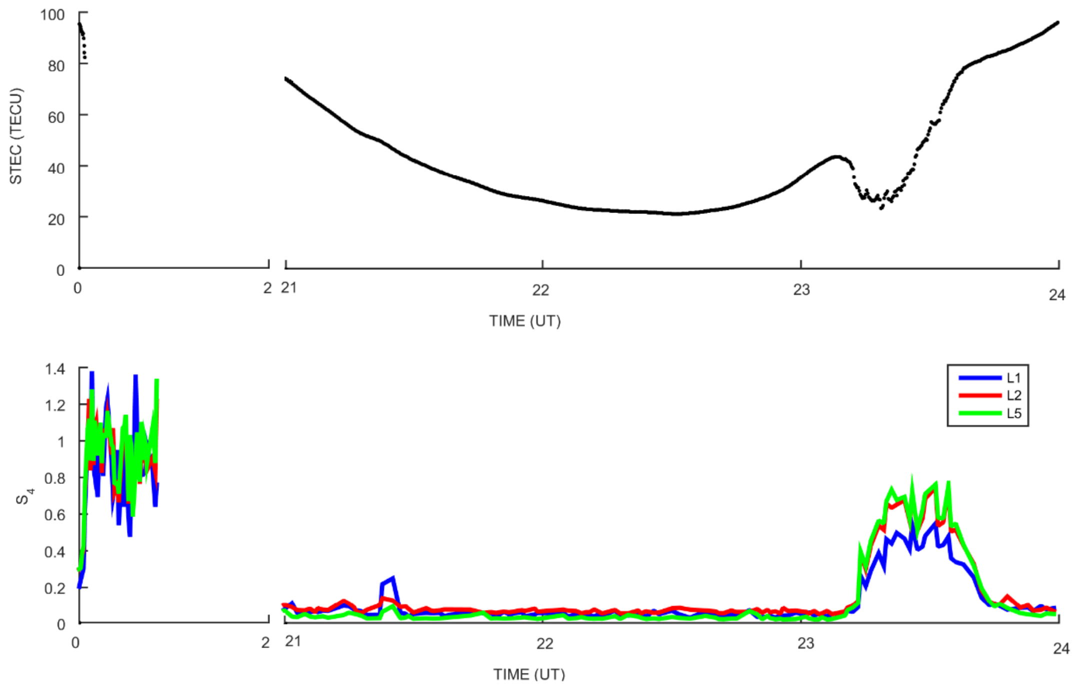

From Figure 2.2, it can be noted a correspondence between the presence of the ionospheric bubble and the occurrence of strong scintillations. It is worth mentioning that, the presence of two data periods is due to the period of satellite visibility. In the first period, the receiver was unable to estimate STEC due to intense scintillation, as shown in Figure 2.2 (top panel), resulting in a loss of lock. In the second period, between 23h – 24h

UT, the S4 values were classified as moderate to strong levels. It can be observed that the STEC values were strongly depleted, indicating that the signals received are crossing an irregular plasma structure. The STEC depletions also suggest that the ionosphere is disturbed by ionospheric plasma. These results revealed a close relationship between the occurrence of ionospheric scintillation and the presence of plasma bubbles.

After understanding the correspondence between ionospheric plasma bubble occurrence and ionospheric scintillation, it was investigated the occurrence rate for each intensity level of scintillation. In this analysis, all the available S_4 values were taken into account during the days analyzed. The percentages of occurrence for each frequency considering the S_4 classification levels are summarized in Table 2.1. The highest percentages of occurrence were observed in the undisturbed level, due to the ionospheric scintillation's occurrence at specific times of the day (after the sunset up to midnight, sometimes extending for a few hours). It is important to consider that the scintillation occurrence, especially in strong scintillation levels, may lead to a loss of lock between satellite and receiver, reducing the positioning accuracy. For the undisturbed and moderated scintillation levels, the three signals presented a similar behaviour, i.e. with no statistical differences observed between them. For weak, strong and saturated scintillations levels, the percentage of occurrences increased as GPS frequencies decreased. In addition, for the strong and saturated levels, the percentage of occurrences observed at the L1 frequency (0.6%) was approximately half the values observed for the frequencies L2 and L5.

Table 2.1 – Percentage of occurrences for each carrier frequency considering the S_4 classification levels, for 24 hours of data.

S_4	L1	L2	L5
<0.2	89.8%	87.5%	87.1%
$0.2 < S_4 \leq 0.4$	4.2%	4.7%	5.0%
$0.2 < S_4 \leq 0.6$	2.4%	2.3%	2.2%
$0.6 < S_4 \leq 1.0$	2.9%	4.2%	4.3%
$1.0 < S_4 \leq 1.4$	0.6%	1.3%	1.4%

To perform a quantitative analysis, we considered the S_4 data classified in each scintillation level to identify which frequencies suffer the greatest and the least impact.

In other words, greatest and least impact means that the signal presents the highest and least S_4 values compared to the other signals. Figure 2.3 presents the percentage of the epochs in which each frequency suffered the greatest and the least impact, the sum for each frequency must be 100%.

Figure 2.3 – Percentage of epochs in which the GPS frequencies suffered least and highest impact considering S_4 classification level. The top left panel represents undisturbed level; Top middle panel represents weak level; Top right panel represents moderated level; Bottom left panel represents strong level; and bottom right panel represents saturated level.

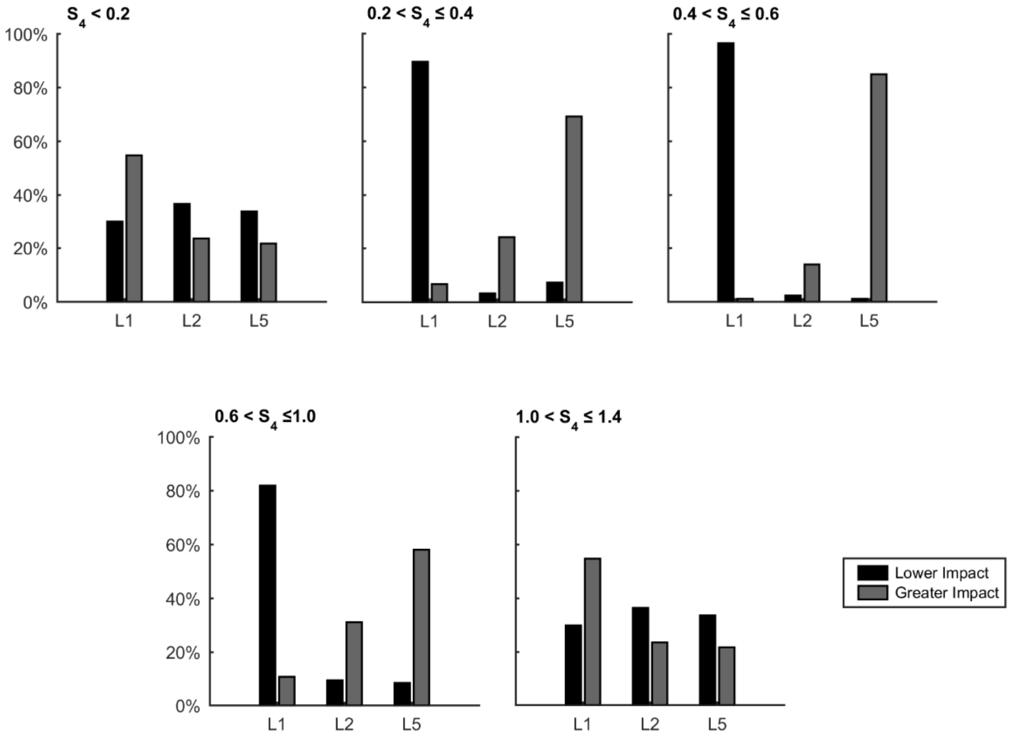

In general, the weak level (top middle panel in Figure 2.3), the moderated level (top right panel in Figure 2.3), and the strong level (bottom left panel in Figure 2.3) presented a similar behavior. The L1 signal suffered the least impact while the L5 frequency suffered the greatest impact, that is, in most of the epochs, the L1 signal presented the least S_4 values compared to the other signals, while the L5 signals presented the highest values. This behavior indicates that during scintillation presence, the L1 signal is less affected by the ionospheric layer. The undisturbed level (top left panel in Figure 2.3) presented a different behavior. The L5 signal suffered the least impact, while the L2 frequency suffered the greatest impact. With the saturated level (bottom right panel in Figure 2.3), considering the least impact, the three frequencies showed a similar percentage. Considering the greatest impact, the L1 frequency was more affected than the other frequencies. To summarize the analysis, we estimated the mean S_4 values and corresponding standard deviation, considering the S_4 classification levels, presented in Table 2.2

Table 2.2 – Mean and standard deviation for the GPS satellites PRN 24, 25 and 27, for 03 November to 03 December 2014, considering the S_4 classification levels.

S_4	Frequencies	Mean of S_4	Std. dev. of S_4
$S_4 \leq 0.2$	L1	0.076	0.038
	L2	0.091	0.046
	L5	0.052	0.029
$0.2 < S_4 \leq 0.4$	L1	0.275	0.138
	L2	0.342	0.187
	L5	0.344	0.194
$0.4 < S_4 \leq 0.6$	L1	0.369	0.246
	L2	0.490	0.329
	L5	0.516	0.346
$0.6 < S_4 \leq 1.0$	L1	0.778	0.395
	L2	0.907	0.456
	L5	0.930	0.466
$1.0 < S_4 \leq 1.4$	L1	1.104	0.011
	L2	1.025	0.025
	L5	1.042	0.023

The mean values and standard deviations confirm the analysis presented in Figure 2.3. For the undisturbed level, the L2 frequency presented the highest mean value and standard deviation, indicating that it is more affected. Considering the weak, moderated, and strong levels, the mean values and standard deviations indicate that the L1 signal is less impacted by ionospheric scintillation, followed by L2 and L5, respectively. In addition, the mean and standard deviation values for the L2 and L5 signals are very similar. Therefore, these results suggest that both signals behave similarly during ionospheric scintillation. Due to the dispersive nature of the ionospheric layer, it was expected that losses of lock would affect the L1, L2, and L5 signals differently. The results confirm the expected behavior. The severity of ionospheric effects follows the same relation considering the signal frequency. The L2 and L5 signals are more likely to suffer from the loss of lock. This performance also can be explained by deep power fades associated with scintillation presence. Considering the saturated level, the L2 signal is less impacted followed by L5 and L1 signals.

In general, we observed that during ionospheric scintillation, the magnitude of scintillations is smaller for the L1 signal and larger for the L5 signal. Despite the fact that the L5 signal is dedicated to safety applications, the results reveal a significant problem for this type of application, particularly in disturbed ionospheric scenarios. As the L5 signal is the most affected under ionospheric scintillation, it may suffer more than other signals, causing positioning errors, loss of lock, and consequently leading to performance degradation and unavailability of service in receivers.

2.3.2 Assessment of GPS point positioning at different frequencies

Considering the positioning experiments, this section presents the Root Mean Squared Error (RMSE) obtained by the comparison between the static and kinematic PPP, considering the GPS signals and their combinations. The aim is to assess each frequency performance during the PPP processing. Regarding the satellites available by epoch, on average, there were 10 satellites transmitting the L1 signal, 8 transmitting L2P and 2 satellites transmitting L5 signal. Figure 2.4 presents the RMSE results in 5 different configurations using the three GPS frequencies, considering all epochs of the day.

Figure 2.4 – RMSE results for PPP processing considering different configurations, for SJCE station level. The top panel represents the positioning considering single frequency L1 (light grey color) and L2 (dark color). The bottom panel represents the positioning considering multi-frequency: L1-L2 (light grey color), L1-L5 (dark grey color) an d L1-L2-L5 (black color).

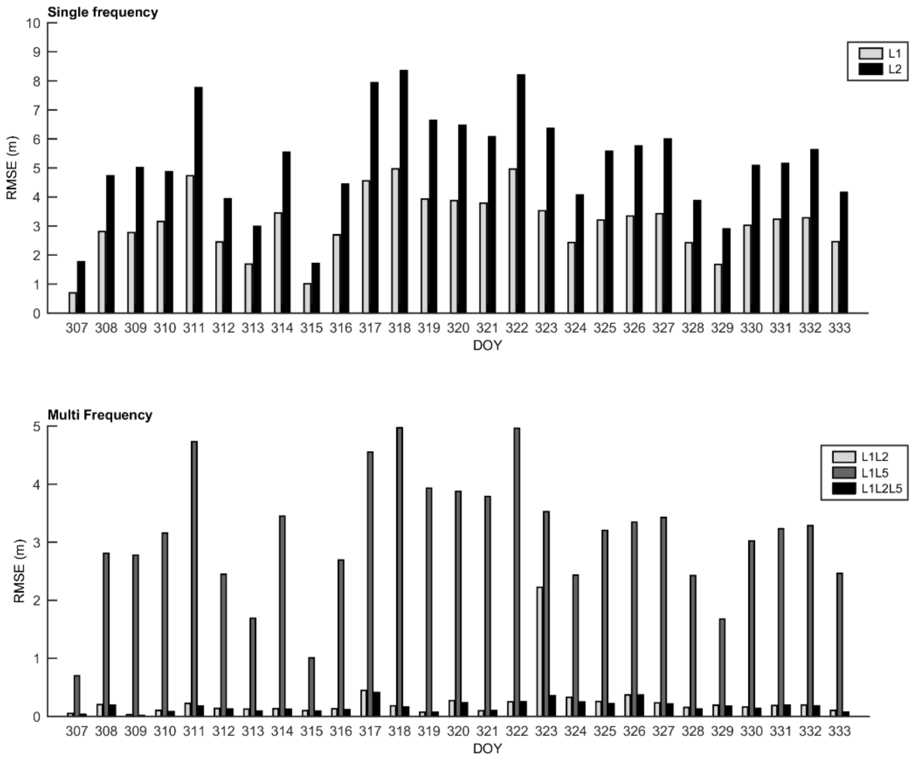

The influence of the use of single or multi-frequency data in the positioning can be noticed in all obtained results. The RMSE values considering single frequency positioning are twice the RMSE values considering the dual frequency positioning. Concerning the single frequency positioning the RMSE obtained from the L2P signal (dark color) presented larger errors compared to the L1 signal (light grey color). This behavior can be explained due to the ionospheric error, which is inversely proportional to the squared frequency. Considering the multi-frequency positioning of the RMSE obtained from L1-L5 (dark grey color), they presented larger errors compared to L1-L2P (light grey color) and L1-L2P-L5. This can be explained due to the use of the linear combination of multi-frequency observables, which cancel out the ionospheric first-order influence. In addition, the RMSE obtained by the L1-L2P and L1-L2P-L5 presented similar values, except for DOY 323. In order to summarize the results, we estimated the mean of RMSE considering the different GPS frequencies. The results are presented in Table 2.3.

Table 2.3 – Mean of RMSE, in meters, considering the GPS frequencies combinations.

GPS frequencies combinations	Mean of RMSE (m)
L1	3.576
L2P	6.037
L1-L2P	0.258
L1-L5	3.580
L1-L2P-L5	0.250

From Table 2.3, in all the considered cases, the RMSE values for the positioning using only L1 signal, are lower when compared with the RMSE value using L2P frequency. Considering the similar number of satellites transmitting both frequencies, the results indicate that L1 frequency is more accurate when compared with L2P frequency. As previously mentioned, this behavior was expected due to the dispersive nature of the ionospheric layer. Thus, L2 signal is more susceptible to loss of lock, which results in a loss of performance for precision applications. For multi-frequency positioning, it can be noted that RMSE values of L1-L5 signals positioning are similar to a single frequency (L1) positioning. Furthermore, it is noted that the RMSE values of L1-L2P signals positioning are also similar when using the three frequencies positioning (L1-L2P-L5). This behavior can be explained by the small number of satellites that transmits the L5 signal for the period when the experiment was performed. On November 19, 2014 (DOY 323) the multi-frequency positioning (L1-L2P and L1-L2P-L5) presented higher RMSE values when compared with the other days. This behavior can be explained by the ionospheric scintillation, the S_4 index behavior over this day is presented in Figure 2.5. It can be noted that the highest S_4 values were observed for DOY 323.

Figure 2.5 – S_4 index from DOY 321 to 325 for SJCE station

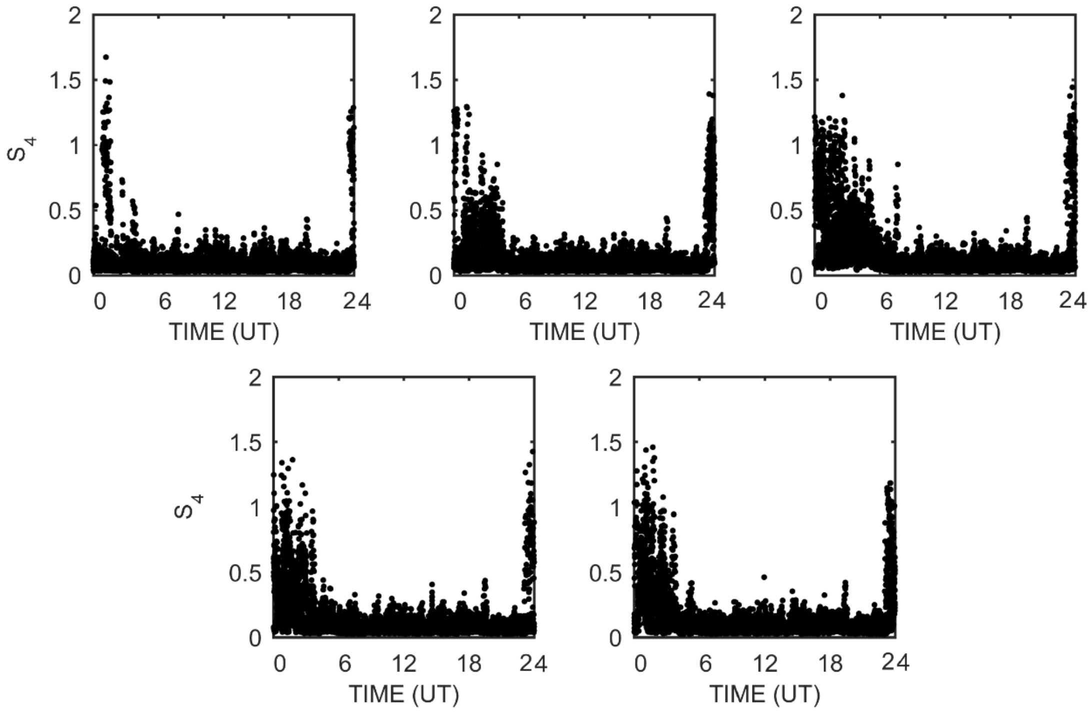

2.4 Conclusion

This Section presented a quantitative analysis of the scintillation amplitude and the performance evaluation of the point positioning considering three different signal frequencies from GPS. The data used were collected over 30 days, for the SJCE station, located in a Brazilian region characterized by strong scintillation occurrence.

In a preliminary analysis, it was shown a visual comparison of the index values for each frequency. The results showed that when the scintillation is classified from weak to strong levels, the data from the L1 frequency are less affected when compared to the other GPS frequencies. In addition, STEC values and S_4 values were compared. It was possible to observe a good correspondence between the occurrence of ionospheric bubbles and the increase in S_4 index values. The results indicate a strong relationship between the occurrence of ionospheric scintillation and the presence of plasma bubbles. It investigated the occurrence rate for each intensity level of scintillation. The results showed that the greatest number of occurrences are obtained for undisturbed scintillation levels at the L1 signal when compared to the other frequencies. Also, there is a bigger number of occurrences with strong and saturated scintillation levels for the L2 and L5 signals.

Considering the quantitative analysis, the S_4 data was classified in scintillation levels to identify which frequency suffers the greatest and the least impact. In general, the weak, moderated, and strong levels presented a similar behavior, the magnitude of scintillations is small for the L1 signal and larger for L5. For the undisturbed scintillation level, the L5 signal suffered the least impact and L2 signal the greatest impact. In the saturated level, the three frequencies suffered a similar impact for the least impact. Therefore, the results confirmed that lower frequencies (L2-L5) suffer more impact of intense scintillation than L1.

Considering the positioning, it was observed that multi-frequency is more accurate than single frequency positioning. For the multi-frequency positioning, the lower RMSE values were obtained using the three frequencies. With dual-frequency, it was observed that PPP using L1-L2P provided more accurate positioning when compared with L1-L5. Furthermore, it was noted that similar RMSE values were obtained with three frequencies and L1-L2P positioning. This behavior can be explained by the small number of satellites transmitting the L5 signal (~ 2 satellites) during the period used. Regarding the positioning considering single frequency, lower RMSE values were obtained with L1 signal when compared to the L2P frequency. Therefore, the results indicate that the L1 signal frequency is more robust than the other frequencies, even under ionospheric scintillation. It can be concluded that not only is the highest frequency less affected by the ionospheric delay, but it is also less affected by ionospheric irregularities such as ionospheric scintillation, except for the scenario of saturated levels of scintillation.

CHAPTER 3

SINGLE FREQUENCY TEC CALIBRATION TO DETECT EQUATORIAL PLASMA BUBBLES

3 SCOPE

Chapter 3 answer if it is possible to detect plasma bubbles using single frequency measurements of GNSS. In this Chapter, a TEC using single frequency calibration procedure is developed to detect the equatorial plasma bubbles.

3.1 Overview

TEC represents the number of free electrons in the column of unit area along which the signal travels between the receiver and satellite (Leick, 2004). TEC is the main parameter capable to describe the properties of the ionosphere. Therefore, it can be considered as an important parameter for many applications, including satellite navigation and communication systems. For instance, ionospheric delay contributes to the absolute positioning error of GNSS-based applications. Autonomous receivers that operate on two or more frequencies can eliminate up to 99.9% of the ionospheric delay by using the so-called ionospheric free combination. However, single frequency receivers cannot reach this precision, requiring TEC calibration techniques or models to compensate for the ionospheric delay (Rovira-Garcia et al., 2020; Aragon-Angel et al, 2021).

TEC estimation procedures are being constantly improved. Global or regional ionospheric models can be utilized for the estimation procedure of ionospheric delay. Initial efforts for TEC estimation based on ionospheric models have been developed by Georgiadiou (1994) and Wild (1994). After GPS constellations became operational, IGS established the IGS Ionosphere Working Group (IGS IonoWG) in 1998 with the purpose of continuous ionospheric monitoring (Hernández-Pajares et al. 2009). GPS receiver data are the input data for producing the official IGS ionospheric models (Feltens 1998; Mannucci et al. 1998; Hernández-Pajares et al. 1999; Schaer 1999) and the results are made available in the form of Global Ionospheric Models (GIMs). Simultaneously to global models, Regional Ionospheric Models (RIMs) were developed such as La Plata Ionospheric Model (Brunini et al, 2004), ModIon (Camargo et al. 2000), and more recently, the model by the Brazilian National Institute for Space Research (INPE – Instituto Nacional de Pesquisas Espaciais) (Takahashi et al 2016). TEC estimation procedure based on the development ionospheric models offers the benefit of ambiguity estimation. In addition, it can be considered an independent method, meaning it does not require external information about the ionosphere to perform TEC estimation. However, many stations are required to effectively implement this method.

An alternative to estimate TEC with less computational effort than ionospheric modeling is performing TEC calibration procedures. Several studies have used TEC calibration methods (Ciraolo et al. 2007; Arikan et al. 2008; Montenbruck et al. 2014; Prol and Camargo 2014; Prol et al. 2018a). In summary, the TEC calibration method involves determining the receiver and satellite hardware biases for each individual station. Usually, the GNSS biases are determined using external ionospheric models. Besides requiring less computational effort, one of the benefits of the TEC calibration method is that it enables estimation for a single station without relying on a dense GNSS network.

Although the GNSS networks provide dense information about the ionosphere, there is still a considerable computational limitation and a lack of TEC data. This lack of data can be associated with the low number of stations, and with disruptions in the received signal caused by ionospheric plasma bubbles under ionospheric scintillation, mainly in the low latitude regions, which are zones with high electron density variability (Li et al. 2021). Several studies have presented a close relationship between the presence of ionospheric plasma bubbles and severe ionospheric scintillations at different radio signals observed at low latitudes (e.g., Spogli et al. 2016; Xiong et al.2016 Morares et al. 2018; Christovam et al. 2022). The scattering of radio signals is caused by variations in the refractive index of the ionosphere, which are directly related to fluctuations in electron density. Higher frequency radio signals present smaller changes due to inverse dependence on the ionospheric refractive index compared to lower frequency signals (Yeh and Liu, 1982; Bhattacharyya, 2022). As a result, lower frequency radio signals are more susceptible to stronger ionospheric scintillations than higher frequency signals. Therefore, considering the GPS signals, it is expected that the GPS L2 and L5 signals will suffer greater ionospheric interference when compared to the GPS L1 signal.

In this regard, a single frequency TEC calibration method can be considered a viable alternative for imaging ionospheric bubbles in the presence of ionospheric scintillation. Aiming to investigate whether ionospheric plasma bubbles could be identified using single frequency measurements, a procedure for TEC calibration using single frequency data is developed in this section. The proposed methodology is assessed through a statistical comparison of TEC values obtained with single and dual frequency signals, as well as analyzing ionospheric maps obtained in the Brazilian region.

3.2 TEC Calibration

TEC calibration is an alternative way to obtain the ionospheric delay with less computational effort when compared to complete ionospheric models. Several studies have utilized calibration procedures for TEC estimation, such as Ciraolo et al. (2007), Montenbruck et al. (2014), and Prol et al. (2018a). In the current work, the calibration method used to estimate TEC dual frequency is based on Prol et al. (2018a) and modified for single frequency. The calibration method is developed in two steps. The first one estimates the bias terms. The second estimates the TEC values. The bias terms over one arc of data with no cycle slips can be computed by means of a linear combination corrected by TEC values retrieved by global ionospheric maps (GIMs). Once the biases term is estimated for all continuous arcs, the TEC in a single epoch is obtained. The method is implemented for single and dual frequency. The main difference is related to GNSS measurement combinations. For the single frequency, the combination between the observables $P1 - L1$ so-called Code-Minus-Carrier (CMC) is used since it eliminates all geometry-dependent components. Considering dual-frequency data, the calibration is performed by the geometry-free combination $L_1 - L_2$. It eliminates all the terms independent on the frequencies, such as the tropospheric delay, clocks, and geometric distance. The TEC using dual frequency (TEC_{DF}) and single frequency (TEC_{SF}) for each epoch are computed using the following equation, respectively:

$$TEC_{DF} = F \times ((L_1\lambda_1 - L_2\lambda_2) - B_{DF}) \tag{3.1}$$

$$TEC_{SF} = K \times ((P_1 - L_1\lambda_1) + B_{SF}) \tag{3.2}$$

where P_i and L_i are the GNSS pseudorange and carrier phase for frequency f_i, respectively; λ_i is the wavelength in meters; K and F terms convert meters of delay to the electrons/m^2 units, being $K = \left({f_{L1}}^2/(2 \times 40.3)\right)$ and $F = f_{L1}^2 f_{L2}^2/40.3 \times (f_{L1}^2 - f_{L2}^2)$, respectively. B_{DF} and B_{SF} represent the bias terms and the residual errors for single and dual frequency, respectively. A bias term for dual (B_{DF}) or single frequency (B_{SF}) over one arc of data with no cycle slips are estimated using TEC^{inx} retrieved by global ionospheric models (GIMs), as following:

$$B_{DF} = \frac{1}{n_{obs}} \sum_{j=1}^{n_{obs}} (L_1\lambda_1 - L_2\lambda_2) - \frac{TEC^{inx}}{F} \tag{3.3}$$

$$B_{SF} = \frac{1}{n_{obs}} \sum_{j=1}^{n_{obs}} (L_1\lambda_1 - P_1) + \frac{TEC^{inx}}{K} \tag{3.4}$$

where n_{obs} represents the number of observations in arc with continuous data.

3.3 Results

3.3.1 Comparison between single and dual frequency STEC values

To perform a validation of the TEC calibration procedure, the STEC values with single and dual frequency are compared. Three representative stations are chosen to cover different latitudinal regions of the ionosphere, belonging to RBMC (Brazilian Network for Continuous GNSS Monitoring). The selected stations are BELE (1.4° S, 48.5° W), CHPI (22.7° S, 45.0° W); and POAL (30.1° S, 51.1° W). BELE station is located near the geomagnetic equator, CHPI is located near the southern crest of the equatorial anomaly whereas POAL is closer to the mid-latitude region. The STEC data are computed for day 006 of 2014 (DOY 006), with clear ionospheric plasma bubble occurrence. In addition, it is considered a 30° cut-off elevation angle to avoid multipath errors.

Figure 3.1 shows a comparative example of STEC values obtained by the calibration procedure with single (left panel) and dual frequency (right panel). The values are expressed in TEC Units (TECU – 10^{16} el/m²). It can be noted that daily behavior between the results is similar. The STEC values present maximum and minimum values at 14 h LT and 5h LT (UT = LT+3), respectively, due to the gradual variations in the electronic density over the day. As expected, the STEC values obtained with single frequency are noisier than the dual frequency values, due to the observable (pseudorange) in the CMC model.

Figure 3.1 – STEC values estimated for each GPS satellite for DOY 006 of 2014 at CHPI station. The left panel shows the STEC values obtained with single frequency whereas the right panel presents with dual frequency. The different colors represent different satellites.

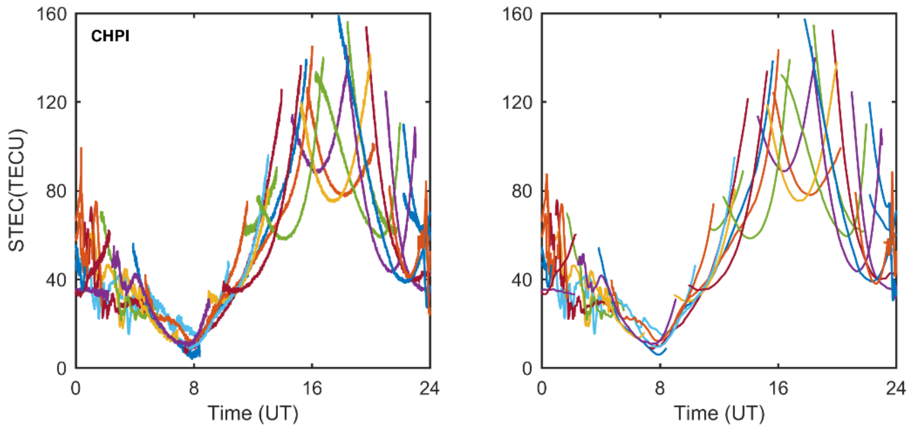

Figure 3.2 shows a visual comparison of STEC values for one arc of data obtained with single and dual frequency at CHPI station for GPS PRNs 2 and 19. According to visual comparison, the single-frequency TEC data agree with dual frequency data. The main difference between the STEC values is that the values derived from single frequency are noisier than the dual frequency values. The discrepancies vary between ±2.5 TECU, where this difference corresponds to the overall noise level and multipath of code measurements. The largest errors can be associated with low satellite elevations. In addition, the STEC depletions of the satellite PRN 19 indicate that the ionosphere is disturbed by ionospheric plasma bubble irregularities. A maximum STEC depletion of approximately 50 TECU occurred between 02:00-03:00 UT. Additionally, it is evident that the differences between the STEC measurements obtained through single and dual frequency methods are slightly larger during the occurrence of ionospheric bubbles.

Figure 3.2 – Visual comparison of STEC (left panel) and discrepancies (right panel) between single and dual frequency for DOY 006 of 2014 at CHPI station for GPS PRNs 2 and 18. Black and red lines present the STEC values obtained with single and dual frequency, respectively.

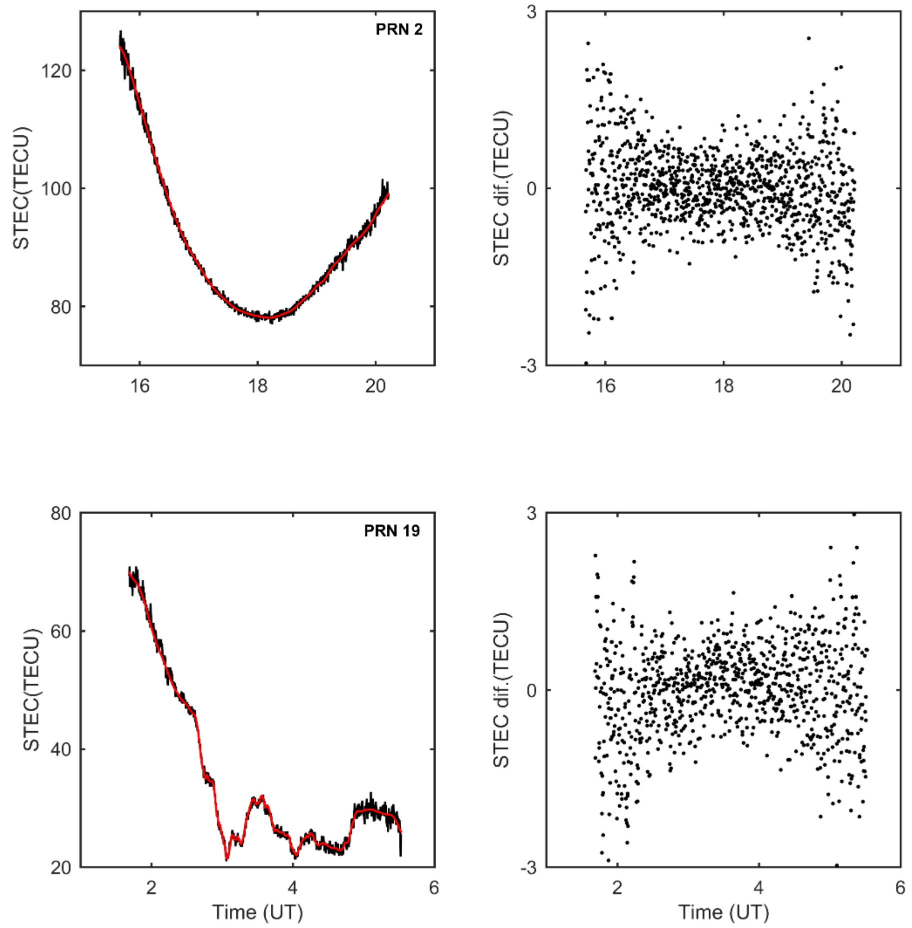

Figure 3.3 shows the STEC values obtained with single and dual frequency for different latitudes. The discrepancies between the STEC values are also presented (right panel). The STEC values obtained with single and dual frequency showed a similar behavior. The discrepancies vary between ±2.5 TECU where this difference corresponds to the noise level of pseudorange measurements. The largest discrepancies are obtained for CHPI, reaching up ± 5 TECU, followed by BELE station. CHPI is located under the EIA south crest, region with the highest ionospheric variability, whereas BELE is located in the trough of EIA. Due to seasonal variations, during the solstice months (summer), the ambient electron density and the plasma density gradients are more intense to produce ionospheric irregularities, with much higher variabilities in the latitude of CHPI. These irregularities cause higher variability in CHPI when compared to the BELE station closer to the geomagnetic equator. The smallest discrepancies in TEC values were observed for

POAL, located outside ow southward of the IEA crest. A summary of the statistical information of the discrepancies considering all available satellites is listed in Table 3.1.

Figure 3.3 – STEC estimated for each GPS satellite for DOY 006 of 2014 for CHPI, POAL and BELE stations. The left and central panels show the STEC obtained with single and dual frequency, respectively. The right panel shows the discrepancies between the dual and single frequency.

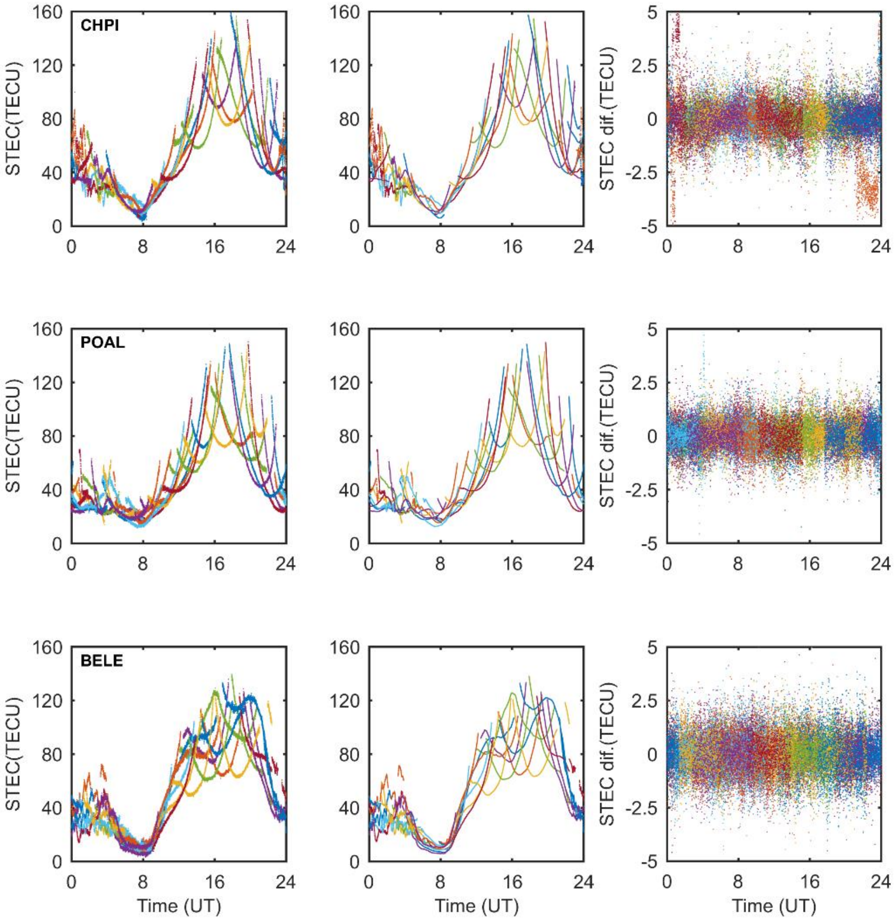

Three parameters are used to evaluate the discrepancies between single and dual frequency obtained with the calibration method: mean, standard deviation (STD), and the root mean- square (RMS) of the difference. The statistical values computed considering 32 GPS satellites are presented in Table 3.1. In general, the mean discrepancy tends to zero, which means that there is no systematic difference between the methods for representing the daily behavior of STEC. The statistical information confirms the results presented in Figure 3.3. The higher discrepancies were obtained for CHPI followed by BELE and POAL stations. In terms of STD and RMSD, the POAL and BELE stations presented similar statistical values, whereas the CHPI showed approximately twice as many values. The STEC values obtained with single frequency were acceptable, with the discrepancies corresponding the random noise level.

Table 3.1 – Mean, standard deviation, and root mean square of the difference between single and dual frequency for DOY003, 2014. The statics values are presented in TECU.

Stations	Mean (TECU)	STD (TECU)	RMS (TECU)
POAL	0.0001	0.5850	0.5850
CHPI	0.0782	1.5431	1.5452
BELE	0.0003	0.7393	0.7393

3.3.2 Ionospheric Maps

To answer if it is possible to detect the ionospheric plasma bubbles using single frequency measurements, this section presents a visual inspection over the generated maps. We present the single frequency maps and compare them with dual single frequency. For the ionospheric maps, GNSS data from 189 stations from IGS, RBMC, RAMSAC (Red Argentina de Monitoreo Satelital Continuo), CIGALA/CALIBRA (Countering GNSS high Accuracy applications Limitations due to Ionospheric disturbances in Brazil), and LISN (Low latitude Ionospheric Sensor Network) networks are used. The location of GNSS stations used for the regional maps is shown in Figure 3.4 (left panel). The ionospheric maps are estimated based on the calibrated STEC values with single and dual frequencies. Figure 3.4 (right panel) provides an idea of the spatial distribution of the IPPs available for DOY 032 of 2014 at 1.8 h UT. The IPPs are obtained assuming an ionospheric peak height at 450 km altitude. It can be noted a low number of IPPs in the Amazon Forest, that impairs the spatial resolution in this area. In addition, the ionospheric plasma bubble can be seen aligned with the geomagnetic equator, located at 50° W and 20º S, which is characterized by the depletion surrounded by higher VTEC values.

For the ionospheric maps, it was adopted a grid with a horizontal resolution of 1° in latitude and 1° in longitude. Since the IPPs are irregularly distributed, a spatial interpolation is carried out over the region of interest. To cover the entire area with VTEC values, the inverse distance interpolation is applied over the IPPs.

Figure 3.4 – Location of GNSS stations used in ionospheric maps (left panel). The dashed line represents the Magnetic Equator. The right panel shows the IPPs spatial distribution for DOY 032 of 2014, at 1.8 h TU.

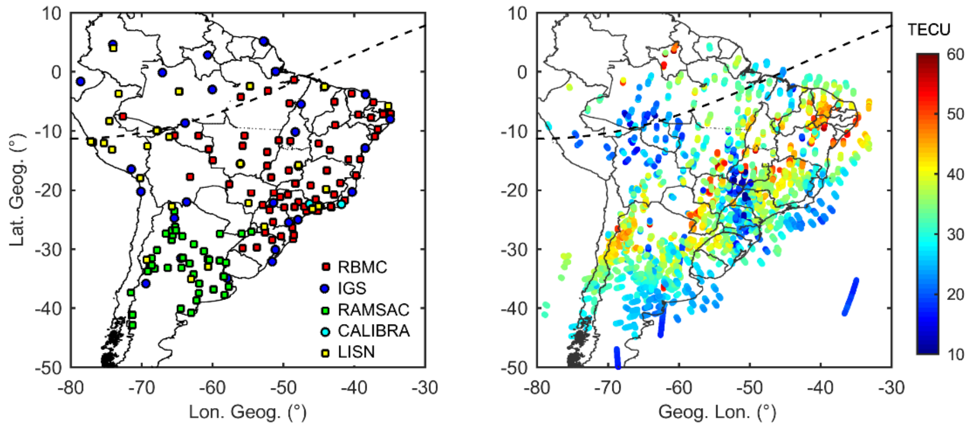

Figure 3.5 shows the interpolation method adopted to map the ionospheric plasma bubbles. To perform the interpolation method, it is necessary a minimum of three IPPs within the search window. Initially, in the first panel of Figure 3.5 only one IPP was found in the search window (red) not reaching the criteria for the interpolation process. In the second panel of Figure 3.5 the search window is expanded to two cells, where two IPPs are found, not reaching the criteria. Then, the search window is expanded to three cells, where only two IPPs are found, failing in the adopted criterion. Since the criteria of this example is reached in no previous steps, the cells are filled with the null value. This process aims to mitigate the irregular distribution of IPPs. In areas with low density in terms of sample points, the IPPs are eliminated avoiding the generalization in the maps. In areas with high density, the ionospheric representation shows more details, since the grid is narrow, and the smoothing effect of the interpolation is less significant.

Figure 3.5 – IPPs interpolations method. The colored points represent the different IPP in the grid. The search window is represented in red.

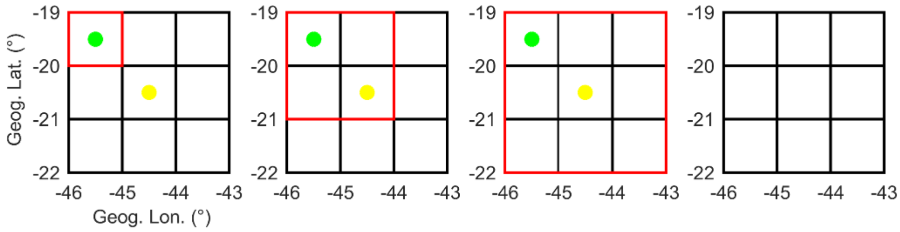

To evaluate the TEC maps obtained with single frequency, the maps obtained with single and dual frequency are compared. Figure 3.6 shows a sequence of VTEC maps for DOY 032 of 2014 with single and dual frequency with a temporal evolution of 6 min, as well as the difference obtained with the maps. It can be noted that the ionospheric maps are similar. The bottom panel in Figure 3.6 shows that the discrepancies are around $\pm$ 2 TECU, however, the largest differences are centered on zero. The largest discrepancies are in the EIA region, due to the higher ionospheric variability. In this region, the high level of ionospheric irregularities is responsible for the generation of ionospheric scintillations in the GNSS signals, which produces GNSS loss of lock and reinitializations of the TEC calculation. VTEC mapping for single and dual frequency provide large-scale coverage of the plasma bubbles. In both maps, it can be seen the formation and evolution progress of the two plasma bubbles. Although the TEC data obtained with single frequency is noisier than the dual frequency data, it is possible to successfully observe the ionospheric plasma bubbles.

Figure 3.6 – Comparison of VTEC maps, for DOY 032 of 2014 between 1.0 UT to 1.8 UT. The top and central panel represents the TEC maps obtained with TEC dual and single frequency, respectively. The bottom panel shows the difference between single and dual frequency.

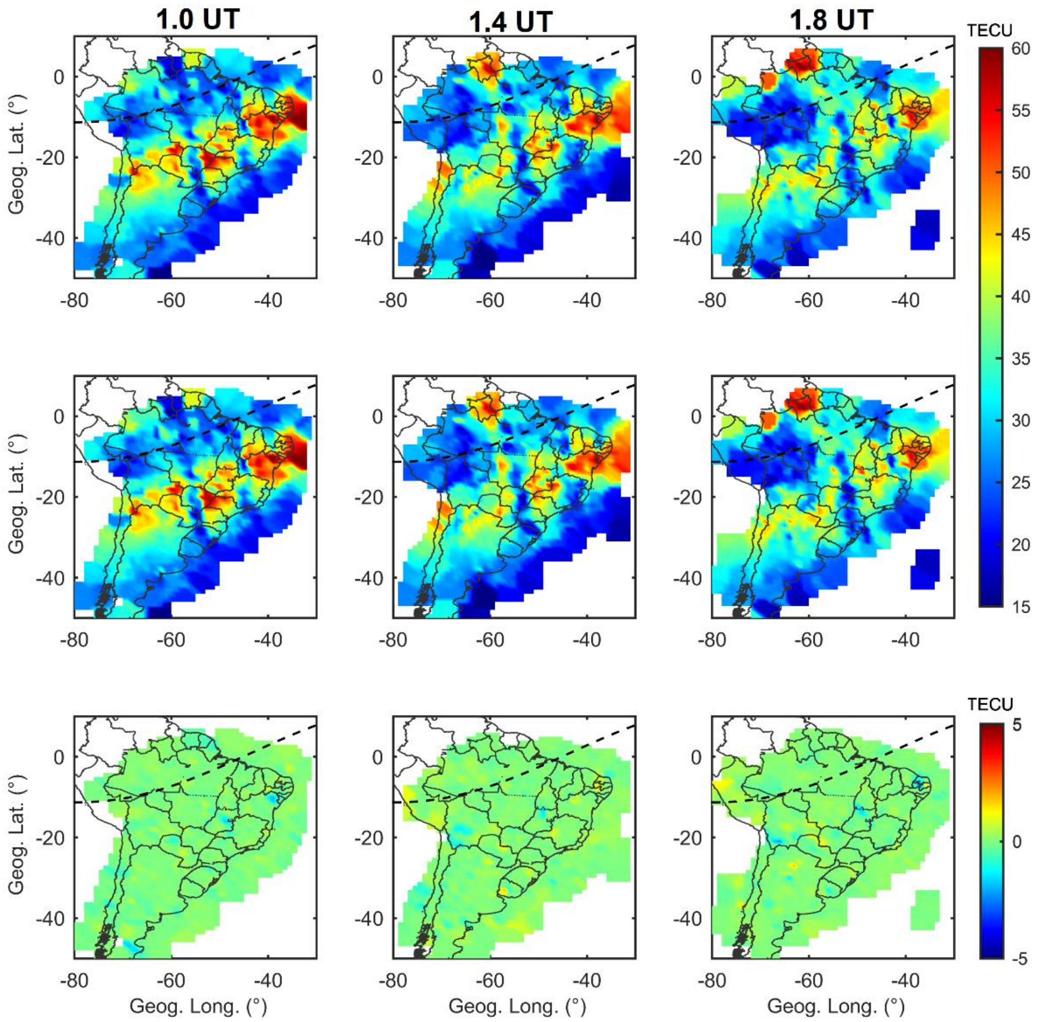

3.4 Conclusion

The calibration method, for single frequency TEC estimation to detect ionospheric plasma bubbles was presented. For the comparison purpose, TEC dual frequency values were also estimated. The single and dual frequency TEC data showed quite similar values. The discrepancies were around ± 2.5 TECU, except for the CHPI station which showed a discrepancy higher than 5 TECU. The station CHPI is located near the EIA south crest, which presents high ionospheric variabilities. As expected, TEC values obtained with single frequency were noisier than those obtained with dual frequency. The main difference between the single and dual frequency TEC values corresponds to the overall noise level and multipath coming from the GNSS combination based on pseudorange measurements. In terms of statistical analysis, the mean, STD, and RMS differences between single and dual frequency also confirmed that discrepancies correspond to the pseudorange random noise.

Analyzing the VTEC maps, it was confirmed the possibility to detect the ionospheric plasma bubbles based on single frequency GNSS TEC data. The ionospheric maps obtained from single frequency data presented a good imaging of the plasma bubbles. It is important to mention that the code noise issues from the CMC combination were not able to impair the plasma bubble imaging. The greatest discrepancies between the single and dual frequency VTEC maps were found along the southern EIA crest. Since this region is more susceptible to ionospheric effects, reinitializations of the TEC estimation were observed.

The proposed method to calibrate the TEC single frequency was revealed as an efficient tool for mapping the ionospheric plasma bubbles. This approach can provide new opportunities, particularly for ionospheric sounding in the real-time, as it is faster than traditional TEC models. Another relevant applicability of the TEC single frequency calibration is that during the last decade, the number of low-cost GNSS receivers has been continuously increasing, especially with growing number of cell phones that make single-frequency GPS receivers with performance available for positioning (Gikas and Perakis 2016, Hernandez-Pajares et al. 2018). In future, it would be relevant to evaluate the capabilities of the proposed calibration method with low-cost cell phone data.

CHAPTER 4

PLASMA BUBBLE IMAGING BY SINGLE FREQUENCY GNSS MEASUREMENTS

4 SCOPE

Chapter 4 summarizes the ionospheric model developed by Christovam et al (2023a). This chapter presents a methodology based on a regional model to calibrate GNSS single frequency measurements and derive ionospheric maps showing plasma bubbles in one of the most challenging conditions, the Brazilian region. The results were validated by the comparison between airglow and TEC single frequency maps in terms of keograms and drift velocities of the ionospheric plasma bubbles.

4.1 Overview

Equatorial plasma bubbles are large-scale depletions in the ionospheric plasma density developed due to ionospheric plasma irregularity. They are mainly caused by the postsunset electrodynamic process. In the equatorial region, shortly after sunset, an increase in the eastward electric field causes initial plasma depletions to rise to higher altitudes. This uplift contributes to an increase in the vertical growth of the plasma-depleted magnetic flux tubes and forms large depleted structures by the Rayleigh–Taylor instability mechanism (de Paula et al. 2007; Hasse et al. 2010; Abdu 2016; Muella et al. 2017; Barros et al. 2018).

According to Nishioka et al. (2008), there are other physical factors that must be considered to understand the behavior of plasma depletions, such as postsunset zonal wind, low atmospheric disturbances, and meridional/transequatorial gradients. These atmospheric disturbances govern the local instability mechanisms; however, the plasma bubbles are also associated with ionospheric temporal variations. Sobral (1985) showed that the plasma bubble occurrence presents a seasonal maximum centered around the summer solstice month. Sahai et al. (2000) and Agyei-Yeboah et al. (2019) showed a strong correlation between plasma depletions and solar activity. Makaela et al. (2004) and Burke et al. (2003) presented seasonal-longitudinal variability, and Fagundes et al. (2005) showed variation during several days as well as day-to-day variation. Despite these significant advances in the understanding of the characteristics of the plasma bubbles, this is a phenomenon not fully understood.

Plasma bubble imaging can bring relevant new knowledge about the characteristics of depletions. Takahashi et al. (2015), for instance, performed plasma bubble imaging by TEC maps and 630 nm airglow images. They have found plasma bubble longitudinal widths on the order of a few hundred kilometers, typically extended along the magnetic field lines to magnetic latitudes of about ±20°. The authors showed that both TEC and airglow images can detect the spatial and temporal evolution of plasma bubbles. However, optical imaging has a better spatial resolution, but TEC maps have an advantage in spatial coverage and continuous monitoring (day and night). Oliveira et al. (2020) presented a methodology to create TEC keograms. The results were validated by comparing them with results from other geophysical instruments, such as all-sky imagers, digital ionosondes, and scintillation monitors. The authors concluded that TEC maps are effective in supplying information not available from other sources. Prol et al. (2018b) showed the first results of a tomographic reconstruction technique for imaging ionospheric bubbles using radio-occultation and ground-based GNSS data. The 3-D maps estimated by tomography allowed to describe both horizontal and vertical structures of the ionospheric plasma bubbles. The authors concluded that the presented technique is more efficient in lower latitudes where the plasma bubbles present larger dimensions. In the region with the highest ionospheric variability, such as around the crests of the equatorial ionization anomaly (EIA), the technique showed the lowest rate of success. The authors explain that GNSS loss of locks and tracking reinitializations provided too few observations to obtain good performance in plasma bubble imaging.

Based on the previous works, it can be concluded that equatorial plasma bubble imaging is a hard task since the all-sky imagers present a limitation related to plasma bubble monitoring due to the dependence on favorable weather conditions, i.e., when there are no clouds or sources of light noise. Airglow images also have a low coverage area, with approximately 1600 km in latitude and longitude, which corresponds to about 15°. However, the plasma bubbles can reach sizes up to 3 times larger than the coverage area of the imagers. Besides the all-sky imagers, there are other techniques to detect the plasma bubbles, such as VHF radars (Tsuonda, 1981; Abdu et al., 2009), satellite in situ measurements (Easters et al. 2019; Aa et al. 2020; Karan et al. 2020), ionosondes (Abdu 2003, 2012; Lee, 2005) and GNSS receivers (Takahashi et al. 2014, 2015; Souza et al. 2021), but they also have spatial/temporal limitations.

Another issue is the lack of continuous GNSS data tracking to generate TEC maps, which is mainly related to the presence of ionospheric scintillations. Indeed, during scintillation events, the receiver can completely fail to track the GNSS signals (Moraes et al. 2018). Delay et al. (2015) presented a statistical analysis of the GPS L1, L2, and L5 signal performance during ionospheric scintillation events using the amplitude scintillation index. The results indicated that the probability of interrupted tracking was larger on L2 and L5 than on the L1 signal. Similarly, Moraes et al. (2017) also showed that the scintillation occurrence increased as GPS frequencies decreased when the receiver was not enabled to estimate TEC with dual frequency observations during the period of intense scintillations. During strong ionospheric scintillation events, the L1 signal is less sensitive to loss of locks than using dual frequency. Even though this is important for mapping plasma bubble structures, single-frequency TEC data has never been used before this work to detect plasma bubbles.

The main problem with using single frequency TEC is that there is the possibility the plasma bubbles cannot be detected due to the noise in the code measurements. To further analyze this point, this Chapter aims to understand if plasma bubbles can be detected using single frequency GNSS measurements. To this end, it was developed a regional model to calibrate the single-frequency GNSS measurements and derive TEC values. Then, the efficiency of TEC maps in detecting plasma bubbles is shown. Simultaneous observations of all-sky images were used as a reference to the validations. Main comparisons were performed using keograms obtained from single frequency TEC and airglow data. The drift velocities of the ionospheric plasma bubbles detected by keograms using TEC and airglow data are also discussed.

4.2 TEC estimation using single frequency data by regional modeling

The main goal in the TEC using single frequency estimation is to provide a feasible data source to map the plasma bubbles. The mathematical formulation to extract TEC data using single frequency GNSS observations is developed in three stages. In the first stage, the conversion of single-frequency GNSS observations to non-calibrated TEC data is performed. The second refers to ambiguity estimation by spherical harmonic modeling of the VTEC. The third stage is related to the regional interpolation of the vertical TEC (VTEC) values in order to detect the plasma bubble structures.

The model is performed using single frequency data from approximately 200 ground-based receivers from the continuous operating GNSS stations throughout America. The data from RBMC, IGS, CIGALA/CALIBRA, LISN, and RAMSAC are used. The stations are chosen to cover all latitudes, with a particular interest in South America since it is the region of interest to our plasma bubble detection. The locations of the GNSS stations are presented in Figure 4.1.

Figure 4.1 – GNSS single frequency stations used in the model. The colored dots represent the location of the stations for the different networks. The dashed line shows the geomagnetic equator.

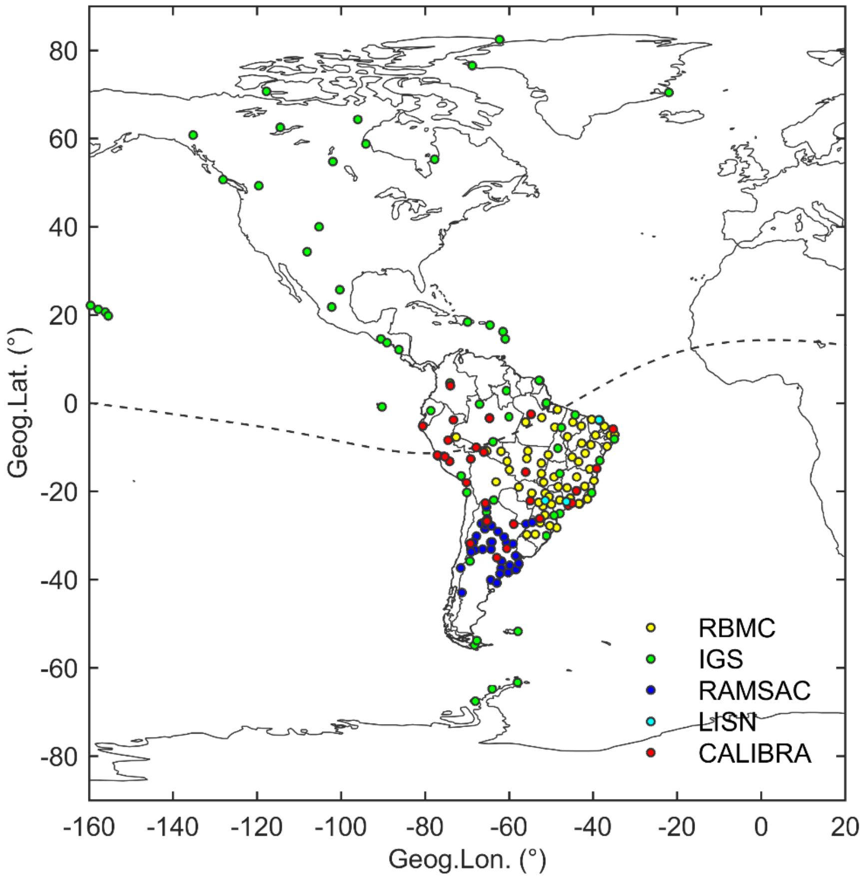

4.2.1 Conversion of single frequency GNSS observations to non-calibrated TEC data

In the first stage, carrier phase and pseudorange measurements obtained by GNSS receivers are used as main observations to derive the non-calibrated TEC data. The raw mathematical representation of the observations, in meters, can be summarized as follows:

$$P_i = \rho + c(dt_r - dt^s) + I_i + T + M_i + D_i + \varepsilon_P \tag{4.1}$$

$$L_i = \phi_i \lambda_i = \rho + c(dt_r - dt^s) - I_i + T + m_i + N\lambda_i + b_i + \varepsilon_\phi \tag{4.2}$$

where P_i and L_i or ϕ_i are the GNSS pseudorange and carrier phase for frequency f_i, respectively, λ_i is the wavelength in meters, ρ represents the geometric distance between the satellite and receiver, c is speed of light in a vacuum, dt_r and dt^s are clock error in receiver and satellite, respectively, I and T represent the ionospheric and tropospheric delay, respectively, M and m represent the multipath delays for pseudorange and carrier phase respectively, N is the integer ambiguity of the carrier phase, D_i and b_i correspond to the code and phase instrumental delays, ε_P and ε_ϕ are the residual error in the code and carrier measurements, respectively. The subscript i represent the signal frequency.

TEC data is typically estimated using dual-frequency GNSS measurements by the geometry-free combinations $P_1 - P_2$ and $L_1 - L_2$. This procedure eliminates all the terms independent on the frequencies, such as troposphere, clocks, and geometric distance, but includes a dependence on the P_2 and L_2 measurements. As shown by Delay et al. (2015) and Moraes et al. (2017), the P_2 and L_2 measurements are more susceptible to ionospheric scintillations, which motivated us to perform the TEC estimation by the single frequency GNSS measurements P_1 and L_1. When using one frequency (f_{L1}), the combination between the observables named Code-Minus-Carrier (CMC) is typically used since it eliminates all geometry-dependent components, as follows (Schuler and Oladipo 2013; Hein et al. 2016; Cooper et al. 2019, Tongkasem et al. 2022):

$$CMC = P_1 - L_1\lambda_1 = 2I_1 - N\lambda + D_1 - b_1 + \Delta\varepsilon \tag{4.3}$$

where the ionospheric delay on L1 signal can be expressed by:

$$I_1 = \frac{40{,}3}{{f_{L1}}^2} TEC \tag{4.4}$$

which leads to the following relation between the TEC values and CMC observations:

$$TEC_R = k \times (CMC + N\lambda_1) \tag{4.5}$$

with

$$k = \frac{{f_{L1}}^2}{2 \times 40,3} \tag{4.6}$$

being a term that converts meters of delay to the electrons/m^2 units.

The relative TEC (TEC_R) values provided by (4.5) are biased, i.e., there is the ambiguity, instrumental delay and multipath term, B. As a consequence, the estimated value can be referred as non-calibrated TEC. This non-calibrated TEC is much noisier than typical dual-frequency TEC since the pseudorange noise, due to the inherent precision of the observable and the typically important multipath M, remains in the CMC combination. Therefore, the TEC accuracy obtained by the CMC combination is limited by the code noise and multipath error level.

4.2.2 Bias term estimation by Spherical Harmonic Modeling

The non-calibrated TEC represents the main combined ambiguity and instrumental delay term among the multipath ones, which remain mostly constant and need to be solved. In the second stage, this problem is solved using the spherical harmonic expansion model. The main goal is to determine the harmonic coefficients and ambiguity terms related to non-calibrated TEC. The order of spherical harmonics expansion depends on the coverage area. For the regional, continental, and global size, normally, it uses 4th, 8th, and 15th order, respectively. For instance, the Center for Orbit Determination in Europe (CODE) uses order fifteen of spherical harmonic functions to describe the global total electron content of the earth's ionosphere every one or two hours. In this work, it is adopted the same spherical harmonic developed as Schaer (1999); however, it used all GNSS data collected 24 hours in local time (LT) and latitude reference frame. Then, the model gets the necessary coverage to estimate the spherical harmonic coefficients with high harmonic order. In this regard, the bias terms can be computed with the following equation:

$$MF \times [k \times (CMC + N\,\lambda_1)] = \sum_{n=0}^{n_{max}} \sum_{m=0}^{n} \tilde{P}_{nm}\left(sen\varphi_m^{ip}\right)\left[A_{nm}\cos\left(m\lambda_s^{ip}\right) + B_{nm}\sin\left(m\lambda_s^{ip}\right)\right] \tag{4.7}$$

where φ_m^{ip} is the latitude of the ionospheric pierce point (IPP), λ_s^{ip} is the longitude of IPP in terms of LT, n_{max} is the maximum degree of expansion, A_{nm} and B_{nm} are the ionosphere model coefficients, $\tilde{P}_{nm}$ are the normalized Legendre polynomials of degree n and order m, and MF is the standard mapping function (Schaer, 1999). The number of parameters is calculated by (n_{max}+1)^2, where A_{nm}, B_{nm} and N are unknown parameters to be estimated by the least square method. For the experiments, the order of spherical harmonics expansion is equal to 15.

Cycle slips and gross errors in the carrier phase observations should be removed before using the CMC in the spherical harmonic model. To this end, TEC values obtained with the single-frequency GNSS measurements were used to detect cycle slips and gross errors. The non-calibrated TEC values between two epochs are compared. If the difference between the epochs is higher than the threshold, a new arc of data is created. It used a threshold equal to 4 TEC Units (TECU), being 1 TECU = 10^{16} el/m^2. It should be noted that we are using local time (LT) to develop the spheric harmonic (SH) model. Since most of the GNSS stations used in the model are defined in a specific longitudinal section (over the Brazilian region), the LT and UT are very similar among the stations. That is why using 24 hours of data is not including huge problems in the estimation. Another point is that we use the 15th order spherical harmonic expansion to estimate only the ambiguity and instrumental delay term related to non-calibrated TEC. Since the ambiguities and DCBs remain constant over several hours, the remaining 24 LT data merging errors are averaged out.

Figure 4.2 is presented in order to show an example of the resulting spherical harmonic model with single frequency GNSS data in terms of latitude and local time for the Brazilian region in the Day of Year (DOY) 024 of 2014. This map covers several latitudes since stations located in the Southern and Northern hemispheres were required for the harmonic expansion. However, the spherical harmonic estimations are more precise in the South America region due to the higher coverage. It may be noted that several ionospheric dynamics are represented, including the daily and seasonal ionospheric variations.

Figure 4.2 – Example of Spherical harmonic model with single frequency GNSS data in terms of latitude and local time at 0h LT for the Brazilian region for January 24, 2014.

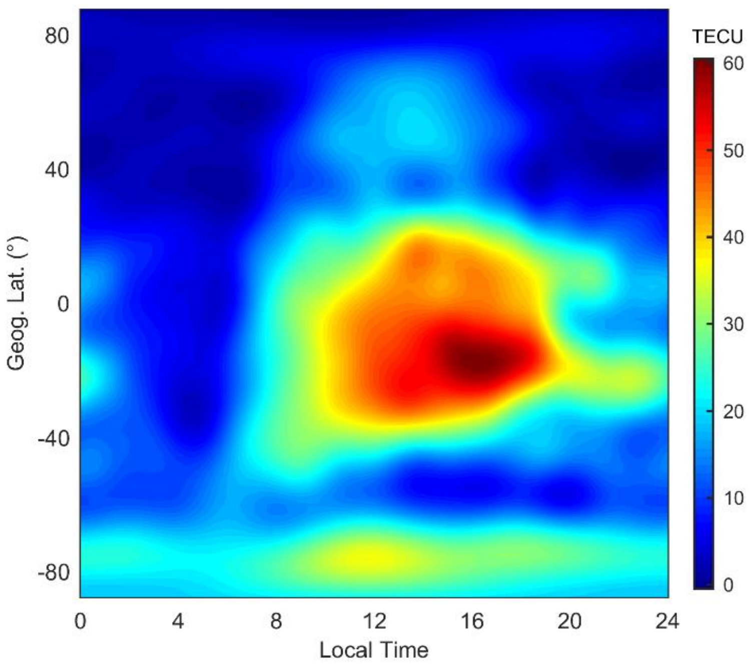

4.2.3 Regional Interpolation

Once the ambiguity and instrumental delay terms are calculated for all transmitter-receiver phase continuous arcs (i.e. without cycle-slips), the next step is carried out to estimate the absolute (i.e. calibrated) TEC values and interpolate them on a regional scale. The TEC single frequency value in a single epoch is directly calculated using the following equation:

$$TEC = (k \times CMC) - B \tag{4.8}$$

where only arcs with a minimum of 50 epochs of continuous data and with a cutoff angle of 20° were used in the experiments.

Given the calibrated single frequency TEC measurements, a conversion to VTEC is performed with the standard mapping function and a spatial interpolation is carried out over the region of interest. The grid over the Brazilian region is constructed with a horizontal resolution of 1° in latitude and 1° in longitude, with an ionospheric shell height of 450 km in altitude and temporal resolution of 6 minutes. To cover the entire area with VTEC values, the inverse distance interpolation was applied over the IPPs. Figure 4.3 presents IPPs over the Brazilian region at 01:30 UT on January 03, 2014. The total number of IPPs was 14671. It may be noticed that there are different IPPs densities for each region. The southeast is followed by the northeast as the region with the highest density of IPPs, containing 4410 and 3939 IPPs, respectively. The southwest region presented a relatively high-density with 3882 IPPs. However, a few IPPs were available in the northwest region, 2440 IPPs, due to the low number of GNSS receivers, mainly in the Amazon forest region.

Figure 4.3 – Spatial distribution of the IPPs over the Brazilian region during the night of January 03, 2014 (DOY003); the dashed line indicates the geomagnetic equator.

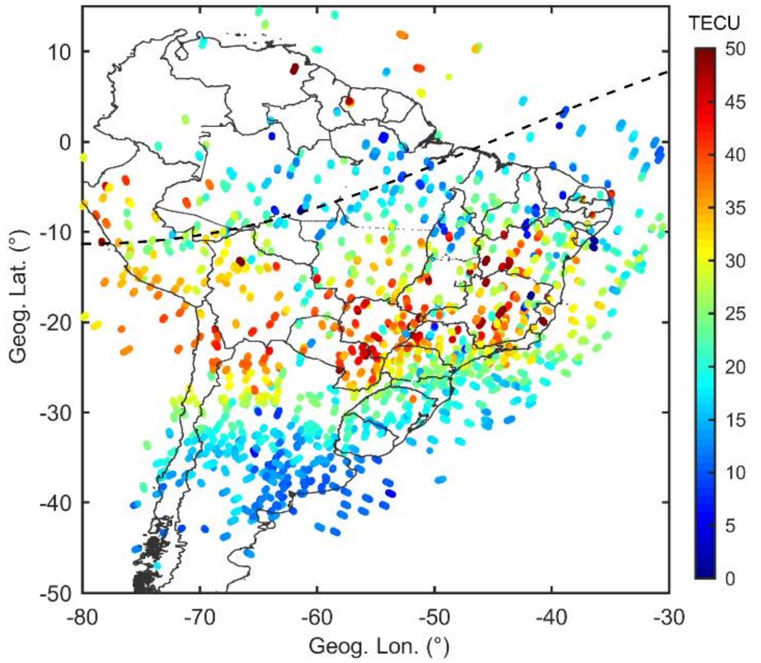

4.3 Results

The validation of the single-frequency TEC measurements as a feasible data source to map plasma bubbles is presented in this Section. The next sub-section presents a comparative example of single-frequency VTEC maps and the corresponding airglow images. Then, the proposed method is validated by comparing the airglow and VTEC maps in terms of keograms. Additionally, discussions are presented to analyze the estimated drift velocities of the ionospheric bubbles.

For the experiments, the data used in this study are based on TEC single frequency measurements obtained by the developed method. The analyzed period is referred to as the maximum of the solar cycle 24. Days with clear evidence of plasma bubbles over the Brazilian region with optical instruments were selected. The days chosen were DOYs 3-9, as well as 21-31 of 2014. Three optical instruments were used. Two of them are located in the low-latitude, at Boa Vista (2.8° N, 60.7° W) and São João do Cariri (7.4° S, 36.5° W). The other station is located near the EIA south crest at Cachoeira Paulista (22.7° S, 45.0° W). In the optical images (OI) from 630.0 nm atomic oxygen emission, i.e., OI 630 nm all-sky images, are the main bands to show the intensity of the depletions associated to plasma bubbles. The airglow images are publicly available at the INPE (Instituto Nacional de Pesquisas Espaciais) data archive. The images cover an area of approximately 1280 km x1280 km with a pixel resolution of 2.5 km.

4.3.1 Case study: DOY 003, 2014

Figure 4.4 shows a comparative example of VTEC maps and the corresponding airglow images. Figure 4.4 (left) shows a VTEC map obtained with single-frequency data and Figure 4.4 (middle) shows a dual-frequency VTEC map in DOY 003 at 1:30h UT (Universal Time). The TEC maps cover an area of 30°–75° W and 10° N–35° S with a temporal resolution of 6 min. It is possible to identify in both maps four plasma bubble signatures almost aligned with the geomagnetic field in the VTEC maps, indicated by the dashed lines. The depletions shown on both VTEC maps coincide with the depletions shown in the airglow images, characterized by dark bands. It is clear that the airglow and VTEC maps are observing the same plasma bubbles. In addition, it can be noted a great discrepancy between the VTEC maps in the region of approximately 10°N, 65°W. In the single frequency VTEC map (Figure 4.4 left), the values reached 50 TECU, whereas in dual frequency (Figure 4.4 middle), these values did not reach 40 TECU. This is mainly due to the low number of GNSS stations in this region. According to our method, as the number of GNSS stations increases, the discrepancies decrease. However, it is important to highlight that code noise and multipath issues from the CMC combination could not impair plasma bubble imaging. In addition, Figure 4.4 (right) shows the plasma bubbles as dark bands. Notice a slight difference between the plasma bubbles detected with TEC data (represented by black dashed lines) and airglow images (represented by red dashed lines). This can be explained by the tilted westward motion of the plasma bubbles with increasing height. As Takahashi et al. (2015) mentioned, the longitudinal discrepancy between the instruments due to this effect is approximately 1°, corresponding to about 111 km.

Figure 4.4 – Comparative example between plasma bubble signature in VTEC maps and airglow images. Both images were obtained on the night of January 03, 2014 (DOY003), at 01:30h UT. The left and middle panels show the TEC maps obtained by the proposed method, using single frequency (GPS L1 signal) and dual frequency (GPS L1 and L2 signal), respectively. The black line represents the position of the geomagnetic equator, and the dashed line represents the ionospheric bubble locations. The right panel shows the plasma bubbles as dark bands of the airglow observations. OI 630 nm images and the grayscale are given in units of normalized intensity (NI); the red dashed line represents the ionospheric plasma bubbles region.

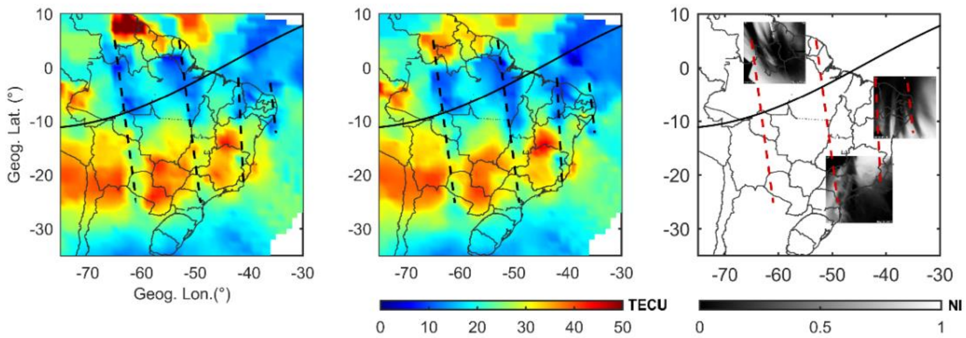

Figure 4.5 (left) shows an example of day 003 of 2014 of the STEC values obtained by the proposed method with dual and single frequency for station BOAV. Figure 4.5 (middle) shows a visual comparison of one arc of STEC data. As expected, the STEC values obtained with single frequency are noisier than the dual frequency values. Figure 4.5 (right) shows the satellite elevation angle and the STEC difference between dual and single frequency calculated for the arc data presented in Figure 4.5 (middle). It should be noted that the difference varies between ±2.5 TECU, where this difference corresponds to the overall noise level of code measurements. The largest errors are associated with low satellite elevations. According to visual comparison, the single-frequency TEC data agree with dual-frequency data. In addition, the residual statistics were computed and the mean error between single and dual frequency was -1.23 TECU. The standard deviation and the root mean squared differences were ±1.41 and 2.82 TECU, respectively.

Figure 4.5 – Comparative example of STEC values obtained with single and dual frequency. The left panel shows STEC data obtained with single and dual frequency for day DOY003 of 2014 at station BOAV. The middle panel visually compares one arc STEC data obtained with single and dual frequency. Dark blue and red lines represent STEC values obtained with single and dual frequency, respectively. The right panel shows the discrepancies between dual and single frequency for the STEC arc data presented in the middle panel.

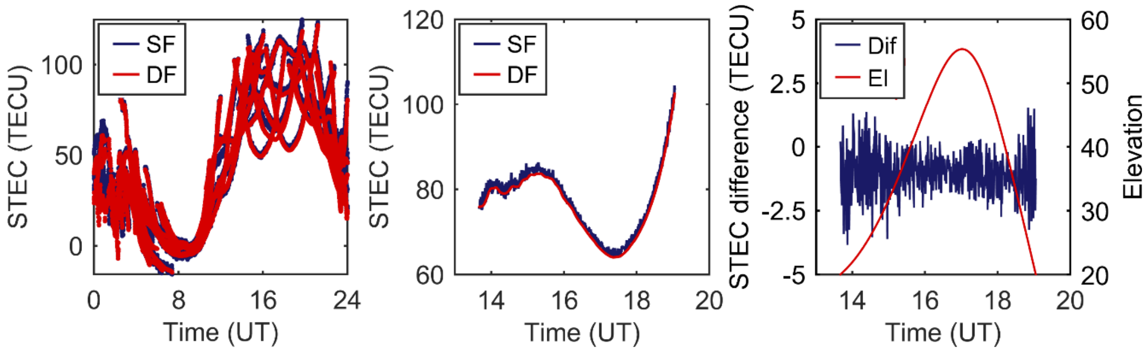

To show more details of the comparison between TEC and airglow images, Figure 4.6 shows an example of a plasma bubble detection in DOY 003 of 2014 over Cachoeira Paulista (CHPI). A white line is included in the longitudinal sector of the station in order to analyze the longitudinal discrepancy presented by Takahashi et al. (2015) and Prol et al. (2018b). It is possible to notice that the plasma bubble detection methods agree. It can clearly see the presence of ionospheric bubbles in the VTEC map and all-sky optical instruments. Additionally, it can note that the plasma bubbles orientation estimated with the TEC maps followed the same orientation shown by the airglow images. There is a northwest tilt of the plasma bubbles in both airglow and TEC images. Thus, it can observe that the plasma bubbles estimated with TEC single frequency are similar in location and orientation. However, it can also notice some relevant differences between the images. Considering the airglow images, it can note higher resolutions, showing two bifurcations in the plasma bubbles. On the other hand, the same cannot be seen on the TEC maps. Another difference is that, at 2h UT, there is a plasma bubble passing exactly over the station, i.e., the white line is located in the middle of the airglow image, while the central part of the bubble did not reach over the station in the TEC maps. As previously mentioned, this longitudinal difference can be explained by the tilted westward motion of the plasma bubbles with increasing height.

Figure 4.6 – Plasma bubbles propagation through Cachoeira Paulista in DOY 003 of 2014 at 2 and 2.2h UT detected by TEC maps using single frequency GNSS data (top panel) and using airglow images (bottom panel) (OI 630 nm).

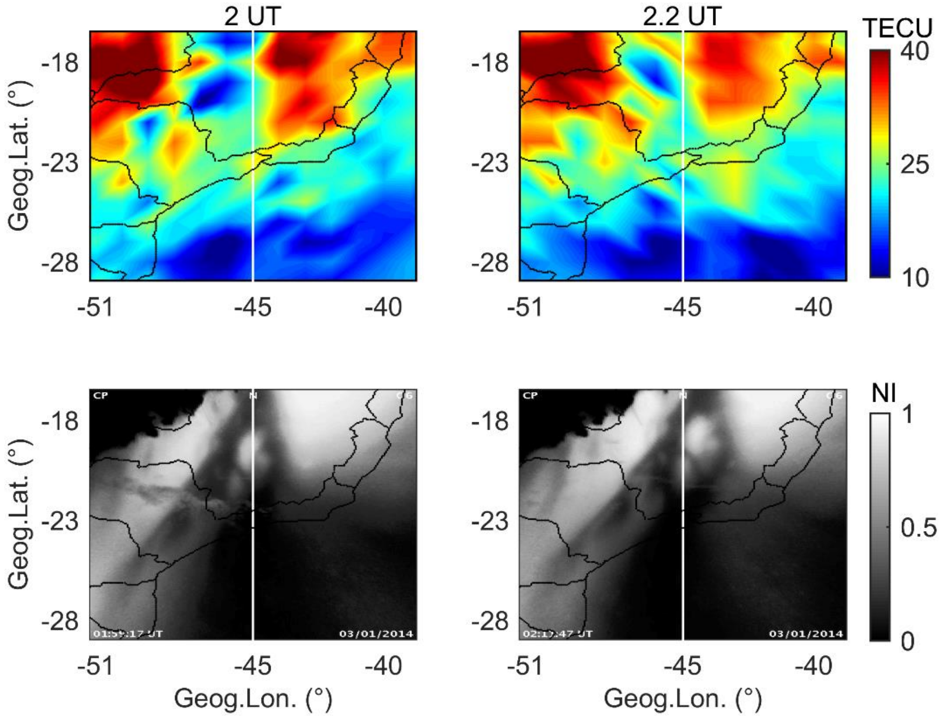

4.3.2 Efficiency of the Plasma Bubble Detections by Single-Frequency TEC Keograms

In order to give an overview of the efficiency of plasma bubble detection using single-frequency TEC data, the keograms obtained from the TEC and airglow images were compared. For this, four cases were created: Case (1) the plasma bubbles can be seen only in keograms with airglow data; Case (2) the plasma bubbles can be seen only in keograms with TEC data; Case (3) the plasma bubbles can be seen in both keograms and Case (4) the plasma bubbles cannot be seen in any keogram. It is worth pointing out that the latitude of the keograms is fixed to the location of the station; for instance, in the BOAV station, the latitude was fixed at 2.8N.

The classification of each keogram was made according to the authors' interpretation. Figure 4.7 shows an example of the case (1), where it can be clearly seen the presence of plasma bubble signatures with airglow data, whereas it is not possible to identify the presence of ionospheric bubbles with TEC data. It can be noted that there is not a good agreement between the keograms obtained TEC values and airglow images. This is likely due to the few IPPs in Boa Vista station. Figure 4.8 is an example of case (2), where it is possible to identify the presence of plasma bubbles only in the keogram with TEC data. It can be seen two plasma bubbles signatures in the keogram with TEC data, with a general motion progressing eastward throughout the night. Regarding the keogram using airglow data of Figure 4.8 (left), it is not possible see the presence of plasma bubbles. In addition, there is a lack of data between 00-01h UT, represented by the dark blue color. Figure 4.9 shows case (3), which is the best situation since the plasma bubbles signatures can be seen in both keograms. Figure 4.10 is an example of case (4), which is the worst case possible since it is impossible to identify the ionospheric plasma bubbles in any keogram, although the presence of plasma bubbles was detected when looking at the entire Brazilian region. In the end, 54 images with two keograms were analyzed considering three all-sky stations. The result of the classification is summarized in Table 4.1.

Figure 4.7 – Example of Case (1): The plasma bubble can be detected only in keogram with airglow data. The left panel shows the keogram with airglow data and the right panel shows the keogram with TEC data, for Boa Vista station DOY 027, 2014.

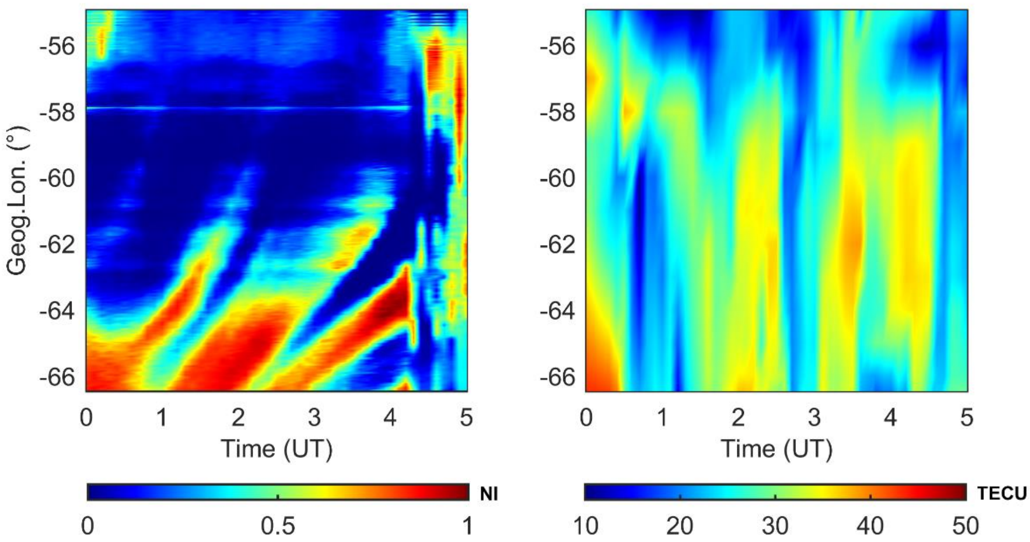

Figure 4.8 – Example of Case (2): The plasma bubble can be detected only in keogram with TEC data. The left panel shows the keogram with airglow data, and the right panel shows the keogram with TEC data for São João do Cariri station on DOY 007, 2014.

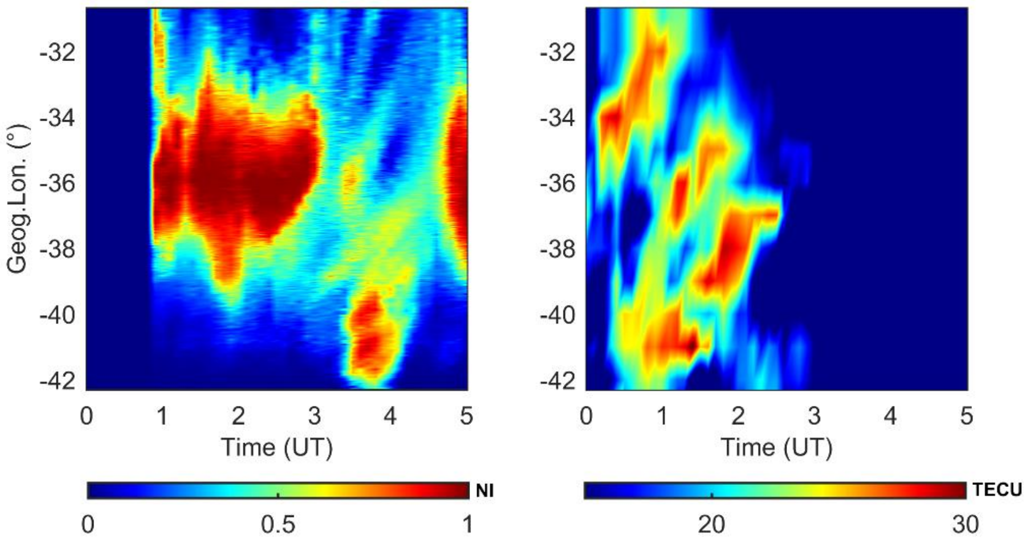

Figure 4.9 – Example of Case (3): The plasma bubble can be detected in both keograms. The left panel shows the keogram with airglow data and the right panel shows the keogram with TEC data, for Cachoeira Paulista station DOY 028, 2014. The black dashed line represents the ionospheric plasma bubbles.

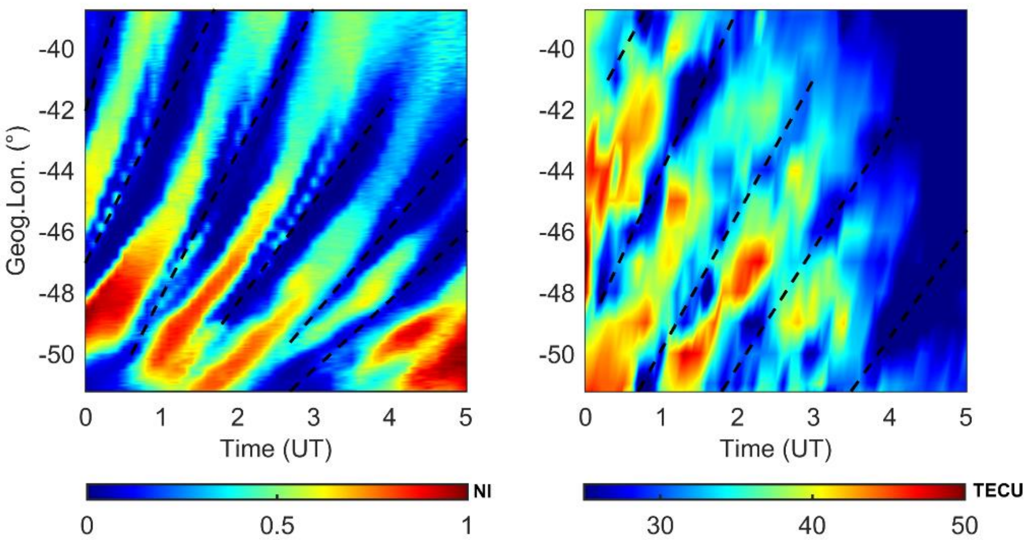

Figure 4.10 – Example of Case (4): the plasma bubble detection is negative in both keograms. The left panel shows the keogram with airglow data and the right panel shows the keogram with TEC data, for Boa Vista station DOY 007, 2014.

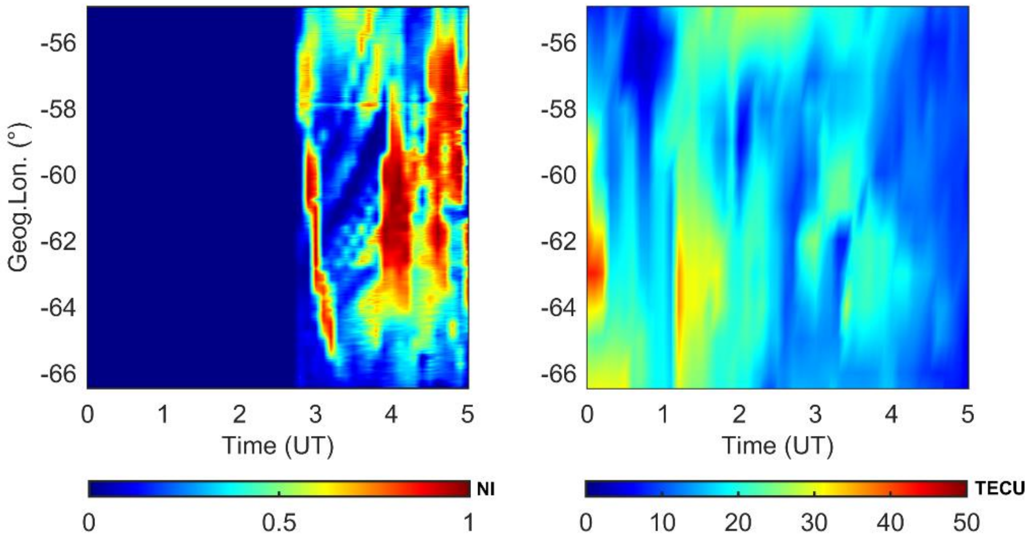

Table 4.1 – Rate of success of plasma bubbles detection in keograms using airglow and TEC data. Case 1: Plasma bubbles only seen in airglow data; Case 2: Plasma bubbles are only seen in TEC data; Case 3: Plasma bubbles seen in both keograms; Case 4: Plasma bubbles not seen in keograms.

CASE 1	CASE 2	CASE 3	CASE 4
BOAV_DOY005	CHPI_DOY003	CHPI_DOY004	BOAV_DOY003
BOAV_DOY006	CHPI_DOY007	CHPI_DOY005	BOAV_DOY004
BOAV_DOY021	CHPI_DOY021	CHPI_DOY006	BOAV_DOY007
BOAV_DOY022	SJCI_DOY005	CHPI_DOY008	BOAV_DOY008
BOAV_DOY024	SJCI_DOY007	CHPI_DOY009	BOAV_DOY009
BOAV_DOY025	SJCI_DOY008	CHPI_DOY022	BOAV_DOY023
BOAV_DOY026	SJCI_DOY009	CHPI_DOY023	CHPI_DOY027
BOAV_DOY027	SJCI_DOY024	CHPI_DOY024	
BOAV_DOY028	SJCI_DOY027	CHPI_DOY025	
BOAV_DOY029		CHPI_DOY026	
BOAV_DOY030		CHPI_DOY028	
BOAV_DOY031		CHPI_DOY029	
		CHPI_DOY030	
		CHPI_DOY031	

		SJCI_DOY003	
		SJCI_DOY004	
		SJCI_DOY006	
		SJCI_DOY021	
		SJCI_DOY022	
		SJCI_DOY023	
		SJCI_DOY025	
		SJCI_DOY026	
		SJCI_DOY028	
		SJCI_DOY029	
		SJCI_DOY030	
		SJCI_DOY031	
22%	17%	48%	13%

From Table 4.1, a rate of success of 65% (48% + 17%) was obtained to detect plasma bubbles by the developed method, where the detection is simultaneous in the airglow and TEC data at 48% of the times. In 22% of the cases analyzed, it was possible to detect the presence of the ionospheric bubbles only in keograms using airglow data, followed by the 17% of cases where it is only possible to detect the bubbles only in the TEC keograms. This is an important point, because it is slightly easier to detect plasma depletions in keograms using airglow data when compared to TEC keograms. However, it must be considered that exist meteorological limitations of the airglow data. Finally, in only 13% of the images analyzed, it could not see the presence of ionospheric bubbles in any keograms. This small percentage is able to show the good efficiency of the keogram method in plasma bubbles imaging.

Boa Vista (BOAV) was the unique station classified only in cases (1) or (4). It reveals that it was not possible to obtain images of ionospheric bubbles using keograms with TEC data for this region. This behavior can be explained by the few IPPs in this region. Boa Vista station is located near the Amazon region, where there is a low density of GNSS stations. Moreover, this region presents high cloudiness for the month of the analysis (January), making it difficult to obtain plasma bubbles images using the all-sky technique. In addition, it may be noted that the plasma bubbles were slightly easier to detect in the Cachoeria Paulista station. From the 18 days analyzed, in 14 days, it was possible to detect the presence of ionospheric bubbles in both keograms for station CHPI, whereas this number was around 12 for station SJCI. This can be explained by more GNSS stations in CHPI, so the proposed method using single-frequency TEC data behaved satisfactorily at regions with enough GNSS coverage.

The results presented here can be confronted with the results by Prol et al. (2018b), which has used dual frequency GNSS observations to map the ionosphere. The authors highlighted that a few TEC observations were collected at the station CHPI due to the region's high occurrence of ionospheric scintillations. The presence of intense scintillations has decreased the performance of the plasma bubble detections by the method developed by Prol et al. (2018b), which has mainly affected the tomographic geometry. However, the opposite is observed. CHPI was the best region to detect plasma bubbles. This is well justified by two points. The first point is related to TEC estimation. Prol et al. (2018b) used dual-frequency data, which is more sensitive to ionospheric scintillations. Our single-frequency approach is more robust, in particular, at station CHPI. A second point is related to the imaging method used to analyze the plasma bubbles. Prol et al. (2018b) have used visual inspection to detect plasma bubbles over the VTEC maps. In this investigation, the plasma bubbles were detected over keograms. Instead of analyzing a unique VTEC snapshot, it was taken into account several hours to evaluate the occurrence of plasma bubbles. Therefore, the keograms have proved to be less sensitive to local variabilities of the ionosphere.

4.3.3 Drift Velocities by Single-Frequency TEC Keograms

In order to investigate the similarity between the drift velocities computed for the different data sources, the velocities estimated using TEC and airglow keograms were compared. The velocities were estimated for all stations and days that were classified in case 3, i.e. where it was possible to detect the ionospheric bubbles with both techniques. The plasma bubble velocities were estimated considering the slope of the black dashed lines segmented over the keograms (see Figure 4.9, for instance), representing zonal drift velocities in the eastward direction. It is worth mentioning that the slope of the trend line over the keograms is determined by visual judgments according to plasma bubbles signatures. Figure 4.11 shows the drift velocities estimated for the plasma bubbles presented in Figure 4.9. In this particular example, it was possible to estimate the drift velocity of 6 plasma bubbles with airglow data, while only 5 bubbles were detected by the TEC maps since the low density of IPPs makes it difficult to detect the plasma bubbles with fine structures. The 6 plasma bubbles shown in the airglow data are producing a zonal velocity of 254.3 m/s, 150.5 m/s, 145.2m/s, 102.3 m/s, 88.4m/s and 69.7m/s respectively. The 5 plasma bubbles estimated using TEC data show a velocity of 141.8m/s, 164.4 m/s, 139.7 m/s 119.3 m/s and 96.6 m/s. The general view of the zonal drift velocities presented a common feature in both methods: the zonal velocities tend to decrease throughout the night. These observations are in agreement with previous studies reported at equatorial and low-latitude regions (Liu et al. 2015; Souza et al. 2021; Muella et al. 2013, 2017). Besides, this result was expected since the electric field is very intense after sunset and decreases with time due to a reduced neutral wind velocity (Terra et al. 2004). Based on Figure 4.11, it can be seen that the results between airglow and TEC maps are consistent, except for the first plasma bubble (PB1), where the drift velocity estimated using airglow data is almost double the velocity with TEC data. This behavior was recurrent for other stations and days, which is well justified by the difficulty in determining the bubble signature at the edges of the keogram.

Figure 4.11 – Plasma bubble drift velocities estimated using TEC and airglow keograms for station Cachoeira Paulista, DOY 028, 2014.

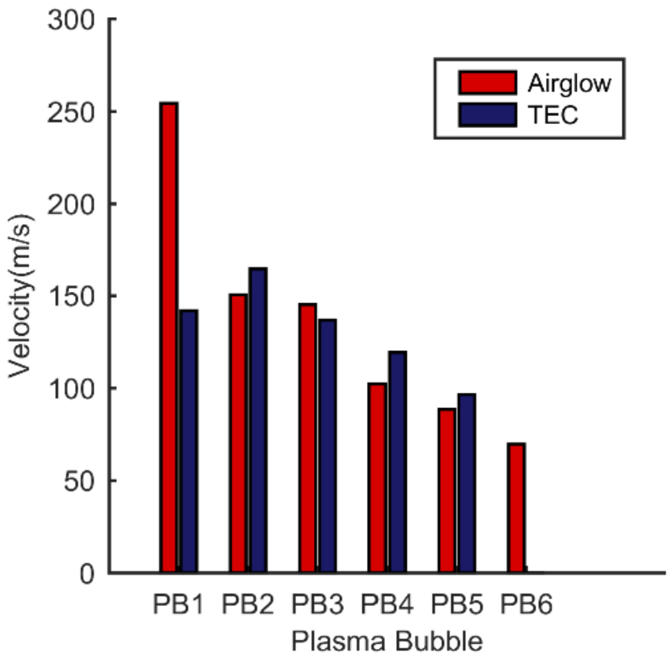

Figure 4.12 presents the variability (scatterplot) of the plasma bubble drift velocities from the stations CHPI (left panel) and SJCI (right panel). This figure was

generated considering all plasma bubbles identified as Case (3). Only the plasma bubble at the keogram's edges that was not considered to infer the statistical analysis. The mean drift velocities estimated using keograms with airglow data were 111.48 m/s and 117.10 m/s whereas the mean velocities with TEC data were 115.98 m/s and 117.94 m/s, for CHPI and SJCI, respectively. The results showed that the mean zonal drift velocities derived from the keograms with TEC are quite similar to the mean velocities estimated from the keograms with airglow data. Besides, the computed mean error between the velocities was -4.50 m/s and -0.84m/s for Cachoeira Paulista and São João do Cariri, respectively. The standard deviations of the errors were 31.90m/s and 35.32m/s. The root mean square of the errors was 31.68 m/s and 34.74 m/s for Cachoeira Paulista and São João do Cariri, respectively. Comparing the statistics results, it was found that the velocities estimated for CHPI presented smaller STD and RMS errors compared to velocities computed in São João do Cariri. However, the velocities estimated for station SJCI gave smaller values for the mean error. Thus, in terms of STD and RMS error, it can be affirmed that the method of estimating velocities using keograms from single-frequency TEC data performs slightly better in regions with high ionospheric variability. The correlation between the velocities obtained by TEC and airglow data were 60% and 71% for Cachoeira Paulista and São João do Cariri, respectively. These values show a moderate positive and linear correlation. It may be noted that the correlations between the stations are similar, which is justified by the similar number of IPPs between the regions.

Figure 4.12 – Scatterplots of the plasma bubble velocities obtained by the TEC and airglow keograms of stations Cachoeira Paulista (left panel) and São João do Cariri (right panel). The trend line is represented in red.

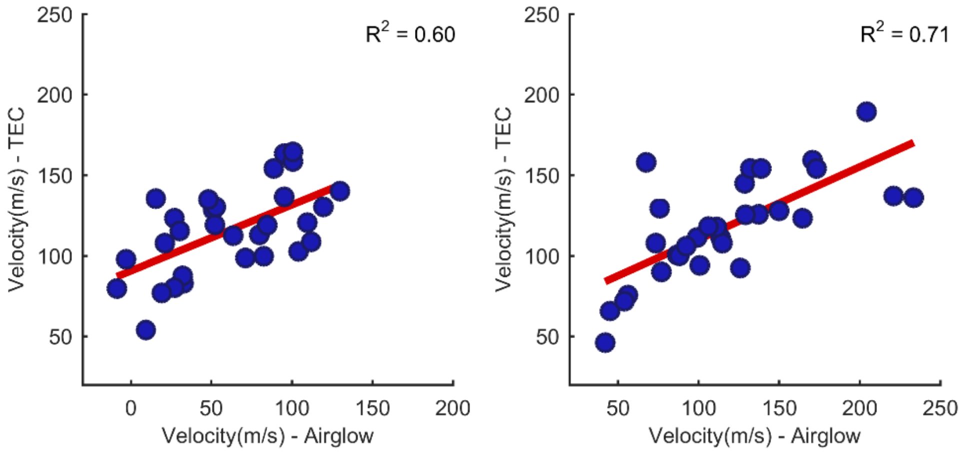

4.4 Conclusion

From the results, it has been confirmed the possibility to detect ionospheric plasma bubbles by single frequency TEC data in regions with high number of GNSS stations. The developed method was capable of diagnosing the spatial and temporal progress of ionospheric plasma bubbles, both in VTEC maps and keograms. The results were confirmed by comparing the estimated TEC depletions with accurate airglow images. In addition, it can be seen a good agreement between the STEC data obtained with dual and single frequency. The discrepancies corresponded to code noise and multipath error levels due to the combination of the observables (CMC).

Concerning the efficiency of the ionospheric plasma bubble detection by keograms using TEC and airglow data, the rate of success with airglow data was around 70%, while using TEC data was 65%. These results suggest that it is slightly easier to detect plasma depletions using airglow data than TEC data. However, it must be taken into account that, due to meteorological limitations of the airglow technique, it was not possible to see the plasma bubbles in the airglow keograms in 17% of cases.

For the Amazon region, the single-frequency TEC technique presented the lowest rate of success in detecting the plasma bubbles, which can be explained by the low number of IPPs in this region. Cachoeira Paulista was an easier region to detect plasma bubbles, in which it was possible to detect the presence of ionospheric bubbles in 77% of the days analyzed. While for the region of São João do Cariri station this percentage was around 66%. This behavior shows that the proposed method using single-frequency TEC data behaved satisfactorily at regions with enough GNSS coverage.

The drift velocities of the plasma bubbles estimated using TEC keograms are in agreement with the estimated velocities by airglow data. Expected daily features were observed, such as the drift velocity decrease after local midnight hours due to the natural decay of the eastward motion of the plasma bubbles. In terms of variability analysis, Cachoeira Paulista presented smaller STD and RMS errors than São João do Cariri. However, the velocities estimated for SJCI gave smaller values for the mean error. Thus, in terms of STD and RMS error, it can be affirmed that the method of estimating velocities using keograms from single-frequency TEC data performs slightly better in regions with high ionospheric variability.

CHAPTER 5

PPP AT LOW LATITUDES WITH IONOSPHERIC MODEL EXCLUSIVELY BASED ON SINGLE FREQUENCY GNSS MEASUREMENTS

5 SCOPE

Chapter 5 shows the performance of the new ionospheric model (Christovam et al 2023b). This chapter presents the evaluation by means of single frequency PPP, comparing the positioning results against the correction using dual-frequency GPS signals, as well as compared to the corrections provided by GIMs produced by the IGS.

5.1 Overview

In satellite-based navigation and positioning, the ionospheric delay is considered a crucial error source. In low latitudes, for instance, the precise point positioning (PPP) accuracy is severely affected by the high ionospheric variability (Veettil et al., 2020). Autonomous receivers that operate on two or more frequencies can eliminate up to 99.9% of the ionospheric delay by using the so-called ionospheric free combination. However, single frequency receivers are not capable to form the dual frequency combinations and are therefore dependent on the ionospheric delay derived by ionospheric models (Rovira-Garcia et al., 2020).

Global Ionospheric Maps (GIMs) are products based on Global Navigation Satellite System (GNSS) data vastly used to represent the ionosphere and improve single frequency positioning. Since 1998, the GIMs are computed by the Ionosphere Associated Analysis Centers (IAACs) and provided by the International GNSS Service (IGS) (Hernández-Pajares et al., 2009). Currently, there are eight IAACs that provide GIMs: the Center for Orbit Determination in Europe (CODE), European Space Agency (ESA), Jet Propulsion Laboratory (JPL), Universitat Politecnica de Catalunya (UPC), Chinese Academy of Science (CAS), Wuhan University (WHU), Natural Resources Canada (NRCan), and Operational Tool for Ionospheric Mapping And Prediction/Deutsches Geodätisches Forschungsinstitut- Technische Universität München (OPTIMAP/DGFI-TUM) (Feltens and Schaer, 1998; Roma-Dollase et al., 2018; Goss et al., 2019). Different estimation techniques have been developed by each center. CODE, ESA, NRCan, and WHU generate GIMs using spherical harmonic (SH) series expansion (Goss et al. 2020;

Li et al. 2015; Roma-Dollase et al., 2018). The technique adopted by JPL is bi-cubic splines whereas UPC adopted the tomographic approach (Mannucci et al., 1998; Hernandez-Pajares et al. 1999). The OPTIMAP use polynomial B-spline for the ionospheric modeling (Goss et al. 2020). Common to all products is the data distribution provided in IONosphere map EXchange (IONEX) format with a spatial resolution 5º × 2.5° in longitude and latitude, respectively, and with a temporal resolution from 15 min to 2h (Schaer et al., 1998; Hernández-Pajares et al., 2017). The GIMs provide Total Electron Content (TEC) from hundreds of worldwide permanent GNSS receivers, normally computed from dual frequency measurements (Schaer et al. 1996; Mannucci et al. 1998; Hernández-Pajares et al. 1999). Carrier phase ambiguities and DCBs are essential parameters estimated by IAACs. The process for estimating DCBs and ambiguities is known as the TEC calibration method, which can be performed either network-wide, such as in the case of GIMs, or with individual GNSS stations (Ciraolo et al. 2007; Prol et al. 2018; Shaikh, 2023).

The performance of GIMs generated by IGS is consistent within the IAACs (Hernández-Pajares et al., 2009), but usually provides lower performance in low latitude regions, especially during ionospheric scintillation events. Prol et al. (2018a), for instance, evaluate the performance of TEC calibration procedures by analyzing the improvement in single frequency PPP considering several latitudes. The authors found a worse PPP performance in low latitudes, mainly due to the ionospheric variability associated with the Equatorial Ionization Anomaly (EIA) and ionospheric scintillation. Rovira-Garcia et al., (2020) additionally assess the quality of the ionospheric models by GNSS positioning and showed larger positioning errors in receivers located at latitudes close to the geomagnetic equator.

One of the main challenges in ionospheric modeling at low latitudes is the presence of ionospheric irregularities that can result in the lack of continuous GNSS operation, especially in GPS L2 frequency. The influence of the ionosphere is different for each frequency since the ionosphere is a dispersive medium, where higher frequencies are less affected when compared with lower frequencies. Delay et al. (2015) show that, during the presence of ionospheric irregularities, the probability of interrupted tracking was larger on GPS L2 and L5 than on the L1 signal frequency. Similarly, Moraes et al. (2017) also present that during the ionospheric irregularities' occurrence, the GPS L1 signal is less sensitive to loss of locks than the L2 frequency.

Given that GPS L1 performs better than GPS L2 frequency, it is reasonable to investigate the possibility to develop ionospheric models exclusively based on GPS L1 frequencies. In this regard, Christovam et al. (2023) present a regional ionospheric model developed for the low latitude region only using single-frequency data. The main disadvantage is that the single frequency TEC measurements is highly dependent on the code noise. Nevertheless, Christovam et al. (2023) have shown that models exclusively based on GPS L1 can be used to detect and analyze equatorial plasma bubbles, despite of the code noise and multipath, which can be strongly mitigated for single-frequency ionospheric monitoring (Hernández-Pajares et al., 2018). Built on this previous work, we intend here to verify whether models exclusively based on GPS L1 frequencies can also be used to improve the single-frequency PPP performance. The main goal is to verify if the single frequency PPP based on single frequency ionospheric model can provide comparable level to those ionospheric models obtained by dual frequency GNSS measurements. In this intend, the PPP performance obtained with the model developed by Christovam et al. (2023) is compared with the single frequency PPP results aided by other consolidated models.

5.2 Method

Section 5.2.1 presents an overview of the ionospheric model proposed by Christovam et al. (2023) exclusively based on single frequency data, as well as the adaptations required to run the same model using dual frequency data. The dual frequency model is presented here to have a base for comparison purposes. Additionally, Section 2.2 shows the configuration used to run the single frequency PPP solutions. The PPP algorithm is used as main indicator to evaluate the proposed model.

5.2.1 Modeling

Christovam et al. (2023) developed an ionospheric regional model to calibrate GNSS single frequency measurements and derive ionospheric maps showing plasma bubble in one of most challenging condition, the Brazilian region. The authors have shown, for the first time, that it is possible to detect ionospheric bubbles using single frequency GNSS data. In addition, the authors also present a comparison of the STEC values obtained with single and dual frequency. The results showed that single frequency STEC data agree with dual frequency data, with differences varying between ±2.5 TECU. This difference corresponds to the overall noise level of code measurements, since the single frequency STEC values are computed based on combination between the observables called Code-Minus-Carrier (CMC).

In this section we present an overview of the ionospheric model proposed by Christovam et al. (2023) along with the necessary adaptations to utilize dual-frequency data with the same model. The mathematical formulation to extract TEC data using GNSS observations was developed in three stages. In the first step, the conversion of GNSS observations to non-calibrated TEC data was performed. The second refers to ambiguity estimation by spherical harmonic modeling. The third step is carried out to estimate the absolute (i.e., calibrated) TEC values and carry out a regional interpolation.

The main difference between the regional modeling using single or dual frequency is related to GNSS measurements combinations. TEC data estimated using dual-frequency GNSS measurements is performed by the geometry free combination $L_1 - L_2$. It eliminates all the terms independent on the frequencies, such as the tropospheric delay, clocks, and geometric distance. When using single frequency, the combination between the observables $P_1 - L_1$ named CMC is used since it eliminates all geometry-dependent components. The combinations used to compute TEC using single (TEC_{SF}) and dual frequency (TEC_{DF}), respectively, can be summarize as follows:

$$TEC_{SF} = k \times (P_1 - L_1\lambda_1 + B_{SF}) \tag{5.1}$$

$$TEC_{DF} = F \times (\lambda_2 L_1 - \lambda_2 L_2 + B_{DF}) \tag{5.2}$$

where P_i and L_i are the GNSS pseudorange and carrier phase, respectively; λ_i is the wavelength in meters; B_{SF} and B_{DF} bias term that represents the ambiguity term, and instrumental delay term affected by the multipath and thermal noise and the residual term for single and dual frequency respectively. The k and F terms convert meters of delay to the electrons/m2 units, being $k = \left({f_{L1}}^2/(2 \times 40.3)\right)$ and $F = \left(f_{L1}^2\, f_{L2}^2/40.3 \times (f_{L1}^2 - f_{L2}^2)\right)$, with f_{L1} and f_{L2} representing the frequencies for L1 and L2, respectively.

The non-calibrated TEC represents the combination between the calibrated TEC, the ambiguity term, and instrumental delay term affected by the multipath and thermal noise. The ambiguity and instrumental delay can be solved together as a unique bias term (B_{SF}) for single frequency and B_{DF} for dual frequency. This term is solved in the second step using a spherical harmonic expansion model. The spherical harmonic model adopted was the same developed by Schaer (1999); however, 24 hours of GNSS data in local time (LT) is used. The model obtains enough spatial information to accurately estimate the coefficients of spherical harmonics with a high order of harmonics. Then, gets the necessary coverage to estimate the spherical harmonic coefficients with a typical harmonic order of 15 degrees. The use of 24 hours of data does not involve huge problems in the estimation, since most of the GNSS stations used in the model are defined over the Brazilian region, i.e., the LT and UT are very similar among the stations, just implying a slight smoothing effect. It is relevant to mention that cycle slips and gross errors in the carrier phase observations must be eliminated before using TEC_{SF} or TEC_{DF} in the spherical harmonic model. For this purpose, we used the non-calibrated TEC values. The non-calibrated TEC values are compared epoch-by-epoch, and the discrepancy between the epochs should not be higher than the adopted threshold (4 TEC Units (TECU), being 1 TECU = 10^{16} el/m².) The ambiguity and instrumental delay term was computed with the following equation for single and dual frequencies, respectively:

$$MF \times TEC_{SF} = \sum_{n=0}^{n_{max}} \sum_{m=0}^{n} \widetilde{P}_{nm} \left(sen\varphi_m^{ip}\right)\left[A_{nm}cos\left(m\lambda_s^{ip}\right) + B_{nm}sin\left(m\lambda_s^{ip}\right)\right] \quad (5.3)$$

$$MF \times TEC_{DF} = \sum_{n=0}^{n_{max}} \sum_{m=0}^{n} \widetilde{P}_{nm} \left(sen\varphi_m^{ip}\right)\left[A_{nm}cos\left(m\lambda_s^{ip}\right) + B_{nm}sin\left(m\lambda_s^{ip}\right)\right] \quad (5.4)$$

where φ_m^{ip} is the latitude of the ionospheric pierce point (IPP), λ_s^{ip} is the longitude of IPP in terms of LT, n_{max} is the maximum degree of expansion, $A_{nm}$and B_{nm} are the ionosphere model coefficients, $\tilde{P}_{nm}$ are the normalized Legendre polynomials of degree$n$ and order m, and MF is the standard mapping function (Schaer, 1999). The number of parameters is calculated by (n_{max}+1)², where A_{nm}, B_{nm} , B_{DF} and B_{SF} are unknown parameters to be estimated by the least square method.

The third step is carried out to estimate the absolute (i.e., calibrated) TEC values, which can be directly calculated after the ambiguity and instrumental delay terms are calculated for all continuous arcs. The third step also perform a regional interpolation in the Brazilian region. The spatial interpolation of the calibrated VTEC values is carried out based on the inverse of the distance. It is considered a grid over the Brazilian region with a horizontal resolution of 1° in latitude and 1° in longitude, with an ionospheric shell height of 450 km in altitude and temporal resolution of 6 minutes. The shell height adopted is the same as that adopted by the CODG and UQRG models, which can be considered approximately the median height of electron density for a typical daytime profile (Mannucci et al. 1998).

The model is executed using data from approximately 200 ground-based receivers from the continuous operating GNSS stations throughout America, especially over the Brazilian region. The data from RBMC (Brazilian Network for Continuous GNSS Monitoring), IGS, GNSS NavAer (De Paula et al., 2022), LISN (Low latitude Ionospheric Sensor Network), and RAMSAC (Red Argentina de Monitoreo Satelital Continuo) are used. The location of the GNSS stations used in regional model are presented in Figure 5.1 (left).

Figure 5.1 – Location of GNSS stations used in regional model (left panel) and GNSS stations used in positioning assessment (right panel). The dashed line represents the Magnetic Equator

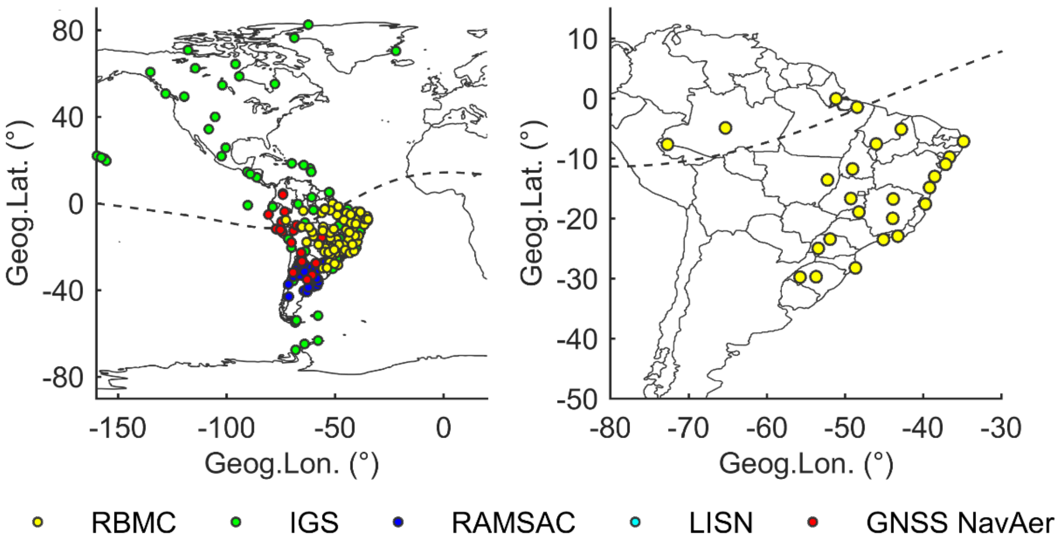

5.2.2 PPP Settings

The GNSS precise point positioning with single frequency data is an important strategy to evaluate the ionospheric models (Rovira-Garcia et al., 2020), complementing the direct assessment in the ionospheric domain (Hernández-Pajares et al. 2017). The main point is to evaluate the quality of the ionospheric delay based on direct corrections over carrier phase and pseudorange measurements. In this work, the evaluation is performed to assess the quality of the developed regional ionospheric model when using single frequency TEC data and compare it with the results obtained by the same model, when using dual frequency GNSS data. The most usual ionospheric products for GNSS applications, i.e., GIMs provided by IGS, UQRG and CODG, are also included in the positioning analysis. The UQRG and CODG products are selected because they have shown some of the best results in terms of GNSS positioning (Jerez et al. 2023).

Once the single and dual frequency TEC values are obtained by the proposed method, VTEC grids are exported in IONEX format with the previously mentioned resolution (1º x 1º in latitude and longitude, updated every 6 minutes). To analyze the performance of the ionospheric models, as applied to the GNSS positioning, the RTKLib is used (Takasu and Yasuda, 2009). Single frequency PPP in kinematic positioning method is chosen to evaluate the ionospheric models, as the kinematic mode directly applies the ionospheric delay to correct the GNSS observations epoch by epoch. The overall PPP settings is defined as:

1) combined solutions obtained by forward and backward filters;
2) cutoff angle 10°;
3) earth tides corrections;
4) estimation of tropospheric delays during PPP;
5) precise ephemerides (sp3) and satellite clock corrections (clk_5s) acquired from IGS products;
6) global positioning system (GPS) constellation;
7) correction of the phase center variation of both transmitter and receiver antennas;
8) phase wind up corrections;
9) no strategy for ambiguity solution;
10) corrections of differential instrumental bias between the civil and precise codes (CI-P1).

For the analysis, 37 stations from RBMC are used (Figure 1 (b)). It is important to mention that the stations used to the validation were chosen to cover several latitudes in the Brazilian region. The days chosen are DOYs 3-9, as well as 21-31 of 2014. These days are selected because they have clear evidence of plasma bubbles occurrence over the Brazilian region. The main analysis is performed to evaluate the improvement that the TEC obtained from the proposed model offers to PPP during the presence of plasma bubbles. In the following section, we show the PPP results when applying the proposed method. Three parameters were used to evaluate the three-dimensional (3-D) PPP error: mean error, standard deviation (STD), and the root mean-square error (RMS) of the estimations. The main 3-D error is computed by taking the differences between the coordinates obtained in the PPP processing and the reference coordinates. The reference coordinates were obtained from final solution of the SIstema de Referencia Géocentrico para las Americas (SIRGAS) at epoch 2014.

5.3 Results

Section 5.3.1 presents an initial validation of TEC values obtained by the single and dual frequency models. Section 5.3.2 presents brief discussion about ionospheric variability impact on GPS frequencies. Section 5.3.3 shows the single frequency PPP assessment based on single frequency ionospheric model

5.3.1 VTEC plasma bubbles maps with analyzed models

In order to perform an initial validation, a visual comparison of the ionospheric models is presented in Figure 5.2. This example shows snapshot VTEC maps obtained from ionospheric models for the Brazilian region in DOY 003 of 2014 at 02h UT. Top panels shows the maps available from the IGS (CODG and UQRG) whereas the bottom panel present the maps obtained by the proposed methods. Due to the different spatial resolution, the maps provided by the proposed method are quite different from the maps available from IGS In the maps available from IGS, the presence of the northern and southern crest of the EIA are clearly observed, where these two regions are characterized by higher electron density values. For the maps obtained with the proposed methods, it is also possible to see the crests of EIA, however with several irregularities in the region. In addition, two well-defined VTEC depletion (plasma bubbles) can be seen aligned with the geomagnetic meridian. Notice that the main difference between the ionospheric maps is the ability to detect plasma bubbles. This difference can be explained by the spatial and temporal resolution differences. CODG and UQRG produce ionospheric maps with a spatial resolution of 2.5° in latitude and 5° in longitude and a temporal resolution of 2 h and 15 min, respectively. The grid size used by the IGS models are larger than the scale size of the plasma bubbles detected by ground-based observations. Indeed, the scale size of the plasma bubbles are in level of 100 m to a few kms (Bhattacharyya, 2022).

Figure 5.2 – Example of ionospheric models for the Brazilian region, for DOY 003 of 2014 at 02h UT. The top panel corresponds to CODG (left) and UQRG (right) and the bottom panel corresponds to models obtained with L1(left) and L1L2(right).

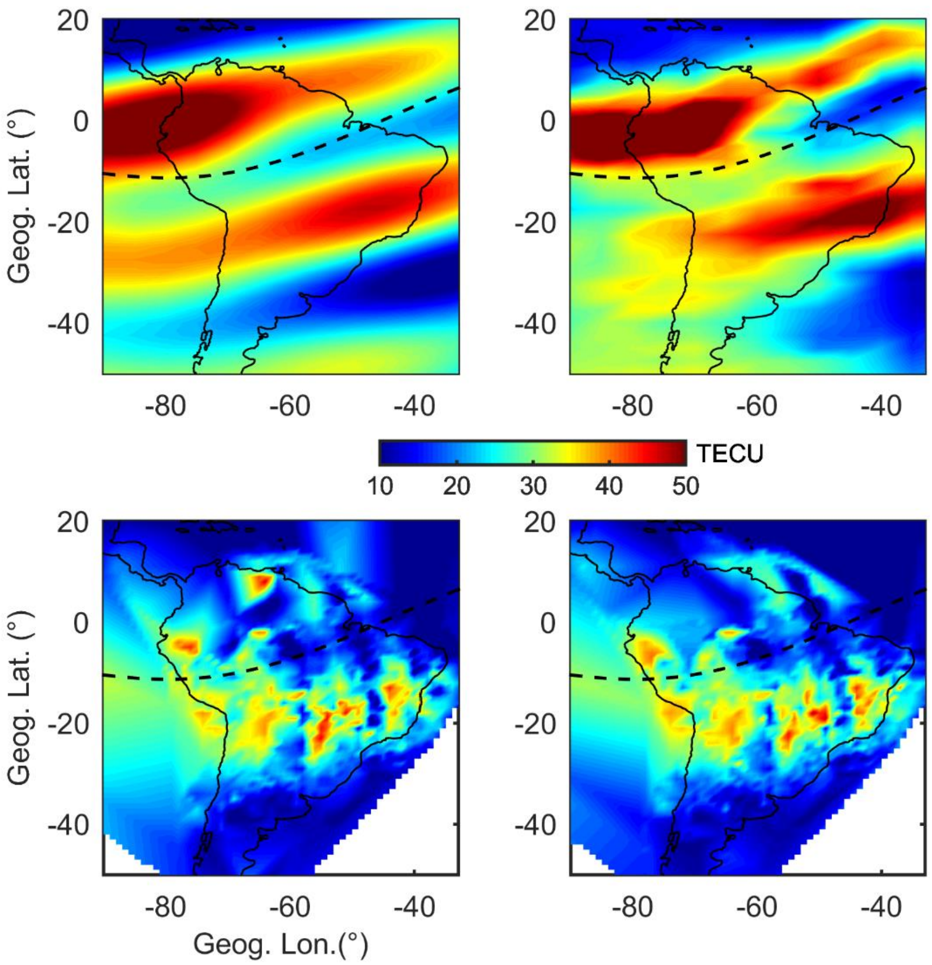

5.3.2 Ionospheric variability on GPS frequencies

During strong ionospheric events, the GPS L1 signal is less sensitive to loss of lock than using dual frequency data (GPS L1 and L2). Therefore, in regions susceptible to strong ionospheric events, more TEC data are expected to be observed with single frequency data. In such case, single frequency data can therefore improve the imaging of ionospheric bubbles due to the provided better data coverage. One way to analyze this point is counting the number of IPPs observed by dual and single frequency data. To perform this comparison, the Brazilian region is divided into 4 sub-regions (quadrants). Figure 3 shows a comparative example of VTEC maps and spatial distribution of IPPs between single and dual frequency data. In this experimental analysis, the total number of IPPs counted for single frequency data was 27970, whereas 27008 IPPs were observed for dual frequency data. It may be noticed that there are different IPPs densities for each quadrant. A summary of the number of IPPs for each quadrant (Q) with single and dual frequency data is listed in Table 5.1. For the period considered, except for a few instances after the plasma bubble passage (around 02h UT), the number of IPPs for single frequency is considerably higher than those for dual frequency. The lower number of IPPs occurs because, as previously mentioned, the L2 frequency is more susceptible to ionospheric effects, which produces GNSS loss of lock and reinitializations of the TEC estimation. The main difference of the IPP numbers between the L1 and L1L2 is, therefore, the loss of lock of the L2 measurements. As expected, better coverage of IPPs is obtained with single frequency TEC data when compared with dual frequency.

Figure 5.3 – Comparative example the VTEC maps and spatial distribution of IPPs over the Brazilian region in DOY 003 of 2014 at 1.2h UT between single and dual frequency. The dashed line indicates the geomagnetic equator. The continuous line represents the division of the map into quadrants. The data used in top panel are single frequency (L1) whereas in bottom panel are dual frequency (L1 and L2).

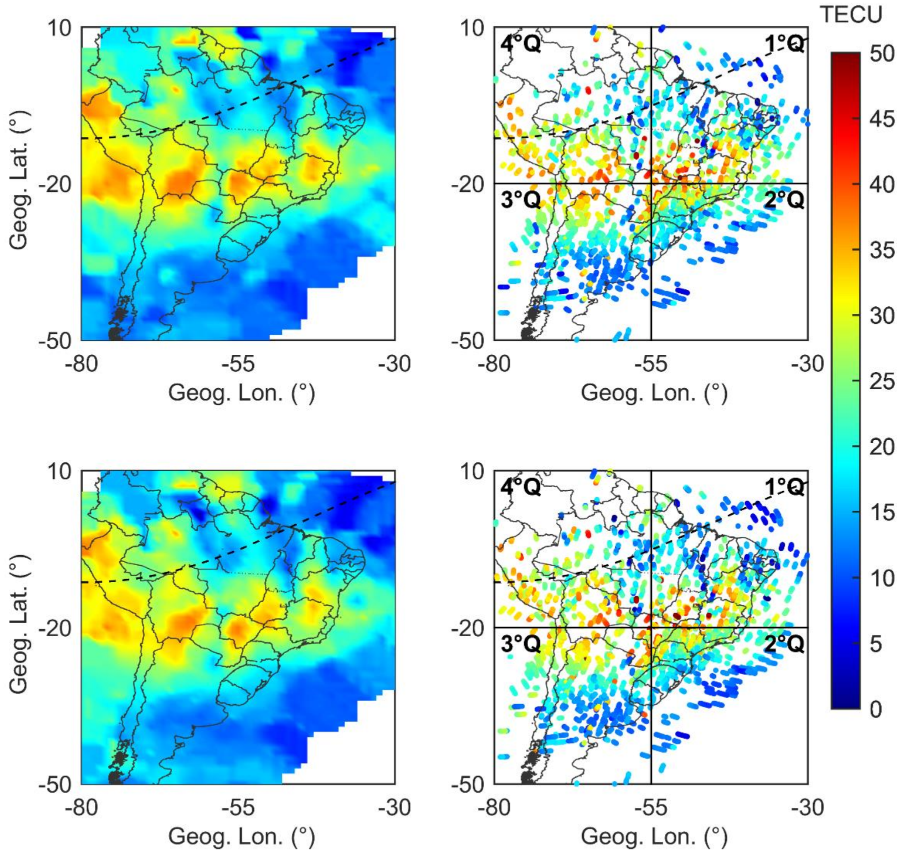

Table 5.1 – Number of IPPs per quadrant during one hour period over Brazilian region for DOY 003 of 2014.

Time (UT)	Frequencies	1°Q	2°Q	3°Q	4°Q
1.0 h	L1	**6715**	**6746**	**8583**	**4388**
	L1L2	6495	6548	8841	4381
1.2 h	L1	**7517**	**7123**	**8745**	**4585**
	L1L2	6824	6992	8608	4584
1.4 h	L1	**7830**	**7441**	**8855**	**4850**
	L1L2	7129	7035	8843	4789
1.6 h	L1	**7673**	**7649**	**8727**	**5206**
	L12	7178	7357	8651	5201
1.8 h	L1	**7456**	**7812**	**8672**	**5789**
	L1L2	7499	7383	8258	5595
2.0 h	L1	7735	**7935**	**8750**	5560
	L1L2	**7747**	7825	8788	**5923**

5.3.3 Assessment by single frequency PPP

In a preliminary evaluation, it is analyzed the results of a single day to show details of the PPP accuracy when applying the TEC provided by different models to account for the ionospheric delay. Figure 5.4 shows a comparison between the 3-D positioning errors throughout the day together with a correspondent keogram for Cachoeira Paulista (CHPI) station (22.7º S, 45.0º W), and the ionospheric scintillation S_4 index at the same latitudinal sector, located in the southern crest of the EIA. In order to apply the keogram technique, it is required to fix the latitude, and then stack the west-east slices of the reconstructed VTEC maps data to form one image (Silva et al. 2019; Prol et al., 2018b). In this case, they were generated with the developed single frequency ionospheric model. According to the daily behavior, the initial (00-04h UT) and final (22-24h TU) hours showed the highest 3D error values, which are caused by depletions in the ionospheric plasma density, as seen in the keograms. This behavior occurs due to ionospheric plasma instability (Rayleigh-Taylor instability), which triggers plasma depletions (bubbles) after the sunset (Takahashi et al. 2015). In the keograms, we can see the general plasma bubble motion progressing from west to east, represented by a tilted dark blue region relative to the temporal axis of the figure, well connected with the highest PPP errors in the initial and final hours of the day. At the same time, it can be seen the higher values to ionospheric scintillation index (S_4). This result confirms the close relationship between the ionospheric plasma bubbles occurrences and the ionospheric scintillation, causing high errors in positioning. Under strong ionospheric scintillations caused by the ionospheric plasma bubbles, the GNSS receiver tracking loop performance is degraded, causing low positioning accuracy. It is important to point out that the increased positioning errors during the 00-04h UT are not associated with the convergence of the single frequency kinematic PPP since we used combined solutions obtained by forward and backward filtering.

Figure 5.4 – Keogram of the VTEC values for the latitudinal section of 22.7°S (CHPI station) in terms of longitude and hours (top panel), 3-D error for the same GNSS station (middle panel) and S_4 index at latitudinal section of (23.2° S) for DOY003 of 2014.

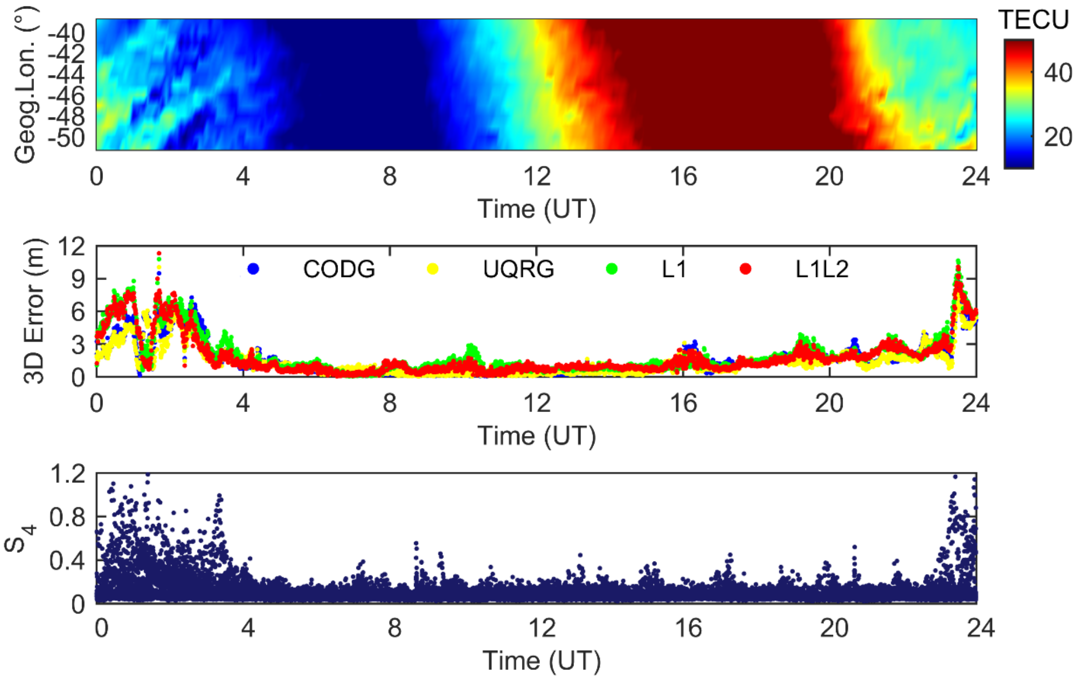

After understanding the correspondence between the plasma bubble keograms and PPP performance for one station, six representative stations were chosen to evaluate different latitudinal regions of the ionosphere. The selected stations were BRAZ (15.9° S, 47.9° W); CHPI (22.7° S, 45.0° W); BOAV (2.8° N, 60.7° W); PBJP (07.1° S, 34.9° W); POAL (30.1° S, 51.1° W) and SMAR (29.7° S, 53.7°W). Figure 5 presents the 3D error calculated for each epoch, and for each model, in the representative stations. Again, larger positioning errors are noticed in the initial and final hours of the day, when the ionospheric irregularities associated to equatorial plasma bubbles impacted the GNSS observations more effectively. It is important to highlight that the magnitudes of 3D errors are considered high for PPP, reaching up to 3 meters.

Considering the entire day of data (24h), the mean error, STD, and RMS for each model are summarized in Table 5.2. According to the statistics, the UQRG presented a better performance compared to the others model in terms of mean and RMS, whereas the proposed model using dual frequency presented a better performance in terms of STD. When we compare the statistics results between the models, the difference is at the decimeter level, while the error is at the meter level. Therefore, it is possible to conclude that the proposed models showed results compatible with the models available from the IGS, including the single frequency model.

Figure 5.5 – 3-D error in meters for DOY 003 of 2014

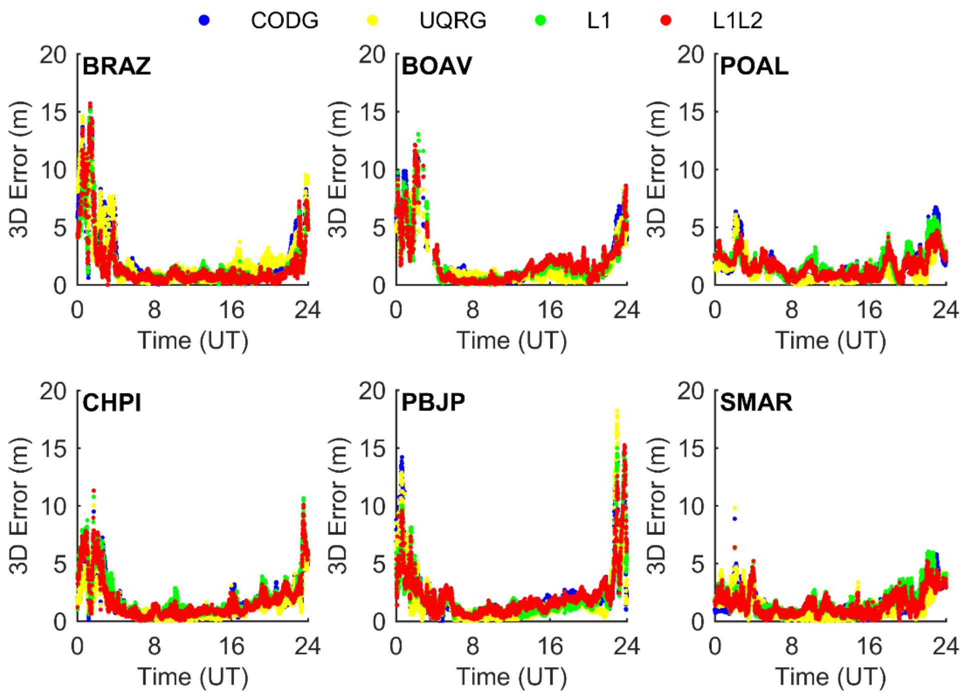

Table 5.2 – Mean, standard deviation and root mean square 3-D error during 24h of data, considering each model for DOY003, 2014.

Model	Mean (m)	STD (m)	RMS (m)
CODG	1.56	1.91	2.47
UQRG	1.55	1.87	2.44
L1	1.76	2.06	2.72
L1L2	1.70	1.82	2.49

As the main goal of the proposed model is to provide a feasible data source to map the plasma bubbles, the next evaluation is carried out only in periods of ionospheric plasma bubbles occurrence. In this regard, Figure 5.6 shows the 3D error obtained in PPP and calculated during the periods with plasma bubble occurrences (00 – 06 h UT). As a result, stations BRAZ, PBJP, CHPI and BOAV, located in regions with high ionospheric activity, presented a 3D error around 15 m whereas the error is around 5 m and 10 m in POAL and SMAR stations, respectively. This difference among the stations occurs because BRAZ, PBJP, CHPI, and BRAZ are in the crests of the EIA, where ionospheric scintillations are more effective, while POAL and SMAR are closer to the mid-latitude region. The corresponding mean, STD, and RMS of the 3D errors in each model are summarized in Table 5.3. Analyzing the statistics, the model proposed with single frequency presented the best performance, followed by the proposed model with dual frequency and UQRG. In this case, CODG presented the worst performance.

Figure 5.6 – 3-D error in meters during plasma bubble occurrence (00 – 06 h UT) for DOY 003 of 2014.

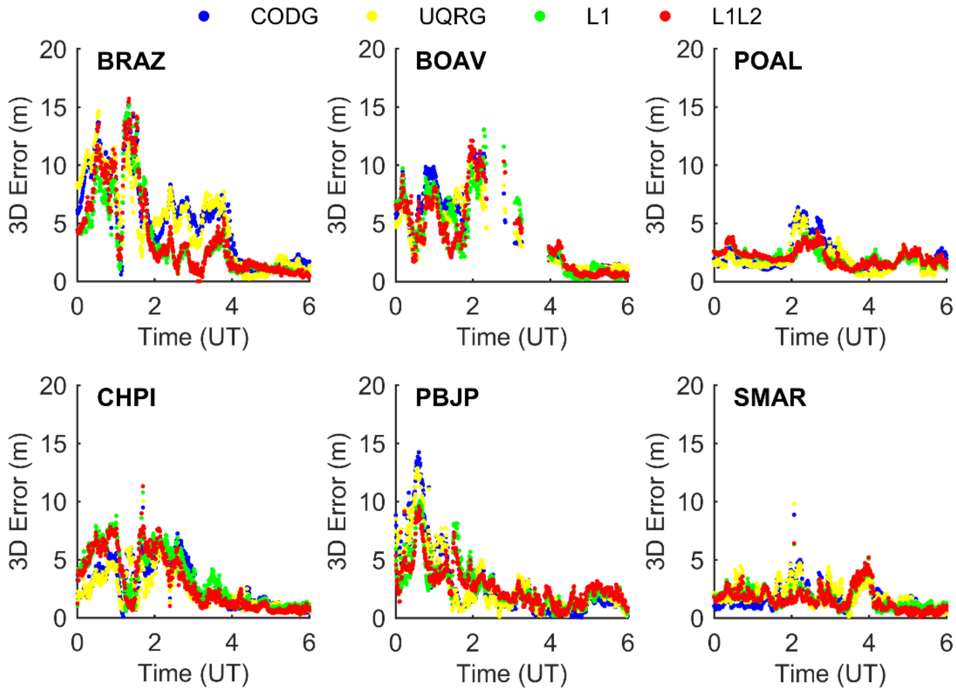

Table 5.3 – Mean, standard deviation and root mean square 3-D error during plasma bubble occurrence (00 – 06 h UT), considering each model for DOY003, 2014.

Model	Mean (m)	STD (m)	RMS (m)
CODG	2.87	2.21	3.63
UQRG	2.74	2.20	3.52
L1	2.72	2.09	3.45
L1L2	2.75	2.15	3.51

In addition, the proposed model was also evaluated during a day characterized by low ionospheric activity DOY 171. Figure 5.7 presents the 3D error obtained in PPP for 24h of data for non-disturbed day. It can be seen that for all representative stations, the

3D error did not exceed 5 m. Additionally, a similar behavior between the models can be observed. Table 5.4 summarize the corresponding mean, STD and RSM values of 3D errors for each model. According to the statistics, the proposed models using single and dual frequency presented similar mean, STD and RMS values. The CODG presented a better performance in terms of mean and RMS, whereas, in this case, the URQG presented the worst performance. It is important to point out that the difference is negligible. Therefore, it can be inferred that the proposed models demonstrated results consistent with the models provided by IGS.

Figure 5.7 – 3D error in meters for DOY 171 of 2014

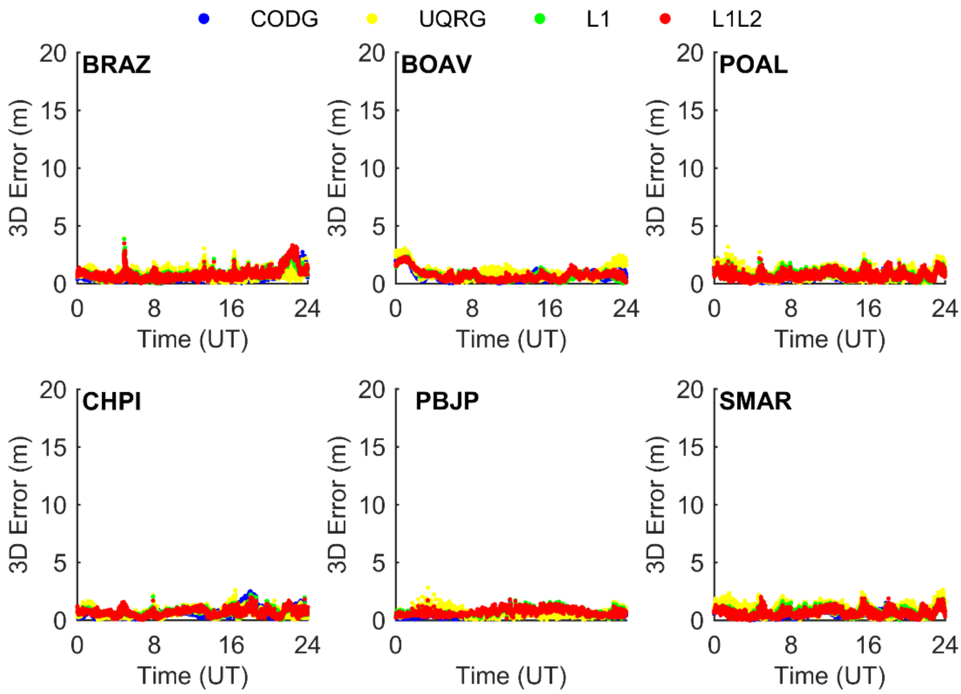

Table 5.4 – Mean, standard deviation and root mean square 3D error during 24h of data, considering each model for a day with low ionospheric activity, DOY171, 2014.

Model	Mean (m)	STD (m)	RMS (m)
CODG	0.66	0.39	0.77
UQRG	0.81	0.41	0.91
L1	0.79	0.36	0.87
L1L2	0.77	0.36	0.86

To provide an overview of the model performance considering several days and stations, we also estimated the statistics using the 37 stations selected during the disturbed days. The results are shown in Figure 5.8. Comparing the statistical results between the results obtained with 24 hours of data and only the period of plasma bubble occurrences, it is noted that, in the period that bubbles are occurring, the results are more dispersed, especially in terms of RMS since the largest errors occur in this period. The results using 24 hours of data are smoothed out by the period when no ionospheric irregularities are present. In addition, considering the latitudinal distribution, we can note a pattern. For the stations near the latitude of 15° S, close to the Southern EIA crest, the errors among the stations tend to converge to a common value. This behavior reveals that the models presented a stable behavior in the worst region to map the ionospheric plasma bubbles, which likely means that the ionospheric delay was equally hard to be computed by all models in the most affected regions.

Figure 5.8 – Mean 3-D error (left), standard deviation 3-D error (middle) and root mean square 3-D error (right), in top panel considering all day (24h) and in bottom panel considering time plasma bubble occurrence (00–06 h UT).

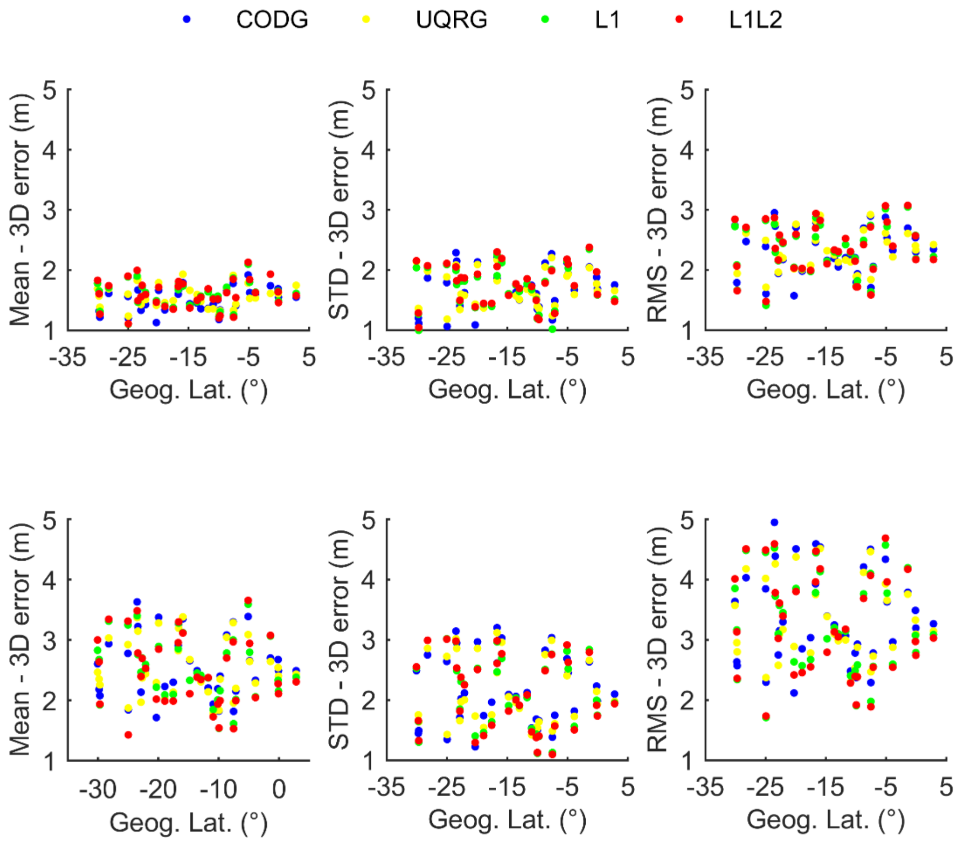

Figure 5.9 shows the cumulative distribution of the 3D positioning errors when considering all stations during the disturbed days. We compare the cumulative distribution considering 24 hours of data (left panel) and considering only the ionospheric bubble occurrence period (00–06 h UT) (right panel). In general, the analyzed models show similar accuracy for both cases. This can be considered a good result, since the proposed single frequency model also show similar results to the dual frequency models. The cumulative distribution using the 24 hours of data, at one-sigma significance level (~68%), has shown that the errors were less than 1.3 m for CODG, while less than 1.4 m for the UQRG, L1L2, and L1 models. For the two-sigma significance level (~95%), the error for all models is about the same, at around 5.2 m. Considering the cumulative distribution for plasma bubble time occurrence at one-sigma significance level, the errors are less than 3.3 m for the CODG and L1L2 models, while the errors are 3.4 m for the UQRG and L1 models. At two-sigma significance level, the error is approximately 7.8m for L1L2, L1 and UQRG, while the error is 8.2m for CODG. Furthermore, it is noticeable that the 3D errors are larger for the time when plasma bubble occurrences were evident. For one-sigma significance level, the 3D error during the plasma bubble occurrence were worse by 40% when compared to 24 hours of data, whereas at two-sigma significance level, it was 65% worse. We can conclude that no model presented a clear better performance in instances with ionospheric irregularities. However, we can infer that proposed model using single frequency presented performance in agreement to the dual frequency models. This can be considered as an advantage, mainly in regions that are directly affected by the ionosphere, since the L1 signal is less sensitive to loss of locks than using dual frequency.

Figure 5.9 – Cumulative distribution of the 3-D positioning errors considering 24 hours of data (left panel) and time plasma bubble occurrence (00–06 h UT) (right panel) for all days and stations selected.

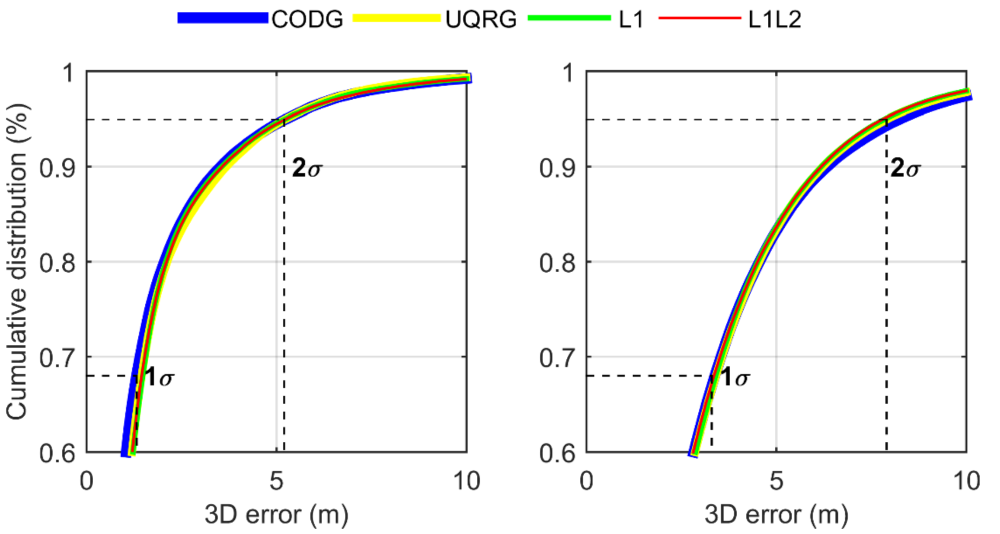

5.4 Conclusion

A new regional ionospheric model using GNSS single frequency data was successfully assessed for the Brazilian region in terms of GPS positioning. The assessment was performed using a single frequency PPP algorithm. We compared the proposed method against a dual frequency regional model, as well as against CODG and UQRG models from IGS. As the ionospheric model using single frequency aims to detect the ionospheric plasma bubbles, three approaches were tested. The models were compared using 24 hours of data collection and during the occurrence of the ionospheric plasma bubbles (00 - 06 h UT). Furthermore, the proposed model was evaluated not only for days characterized by high ionospheric variability but also compared with a day of low activity.

In a preliminary analysis, we presented the comparison between the ionospheric models. The main difference is detection capability of the plasma bubbles for the proposed model using single and dual frequency. In addition, we also compared the 3-D positioning errors throughout the day together with a correspondent keogram and the ionospheric scintillation index S_4. The higher 3-D positioning errors were detected at the same time that it was possible to see the ionospheric plasma bubbles in the keograms and the higher values of the ionospheric scintillation index. This result confirms the strong correlation between the ionospheric plasma bubbles occurrence and ionospheric scintillations, that induces a large positioning error.

In terms of statistical analysis, the mean, STD, and RMS values of the 3-D error between the models were similar. The proposed model presented a comparable performance to the other models in the positioning level. This result was also confirmed by the cumulative distribution analysis. In general, the results demonstrate the feasibility of the regional ionospheric model using single frequency to be used in positioning approaches over the Brazilian region. The results were promising since the proposed method showed a similar behavior to the models provided by IGS.

In the future, the following investigations are recommended: (1) to perform an assessment of single frequency ionospheric models using other evaluation techniques, like using ionosonde data (Jerez et al. 2020) and dSTEC values (Zhao et al. 2021) and (2) to perform the estimation of VTEC single frequency uncertainties since they can provide an additional improvement in the single frequency PPP (Jerez et al. 2022), in particular for low latitude regions.

CHAPTER 6
FINAL REMARKS

In this work, a methodology capable to detect equatorial plasma bubbles using only GPS single frequency measurements was proposed. For this purpose, it was investigated which GPS signal frequency is best suited to detect equatorial plasma bubbles. Two TEC single frequency estimation procedures were presented. Finally, the quality of TEC obtained by the proposed method was evaluated based on PPP.

Chapter 2 presented the results of a quantitative analysis of the scintillation amplitude of GPS signals at L1, L2 and L5 frequencies, aiming to evaluate the impact of the ionospheric scintillations on the GPS frequencies. During ionospheric scintillations, a smaller magnitude was observed for the GPS L1 frequency. Therefore, it can be concluded that L1 frequency is the most suitable signal for ionospheric plasma bubble imaging, since it is the least affected by the ionosphere.

Chapters 3 and 4 answer if it is possible to detect plasma bubbles using single frequency measurements of GNSS. In Chapter 3, TEC single frequency calibration procedure was proposed. TEC single frequency was calibrated using TEC values retrieved by global ionospheric models. As expected, TEC values obtained with single frequency are noisier than the dual frequency values, due to the combination between the observables CMC. However, it is important to highlight that code noise and multipath issues from the combination were not able to impair the plasma bubble imaging. Therefore, it can be confirmed that it is possible to detect ionospheric plasma bubbles by single frequency TEC data. The calibration procedure is an alternative to estimate TEC with less computational effort. This approach can provide new opportunities, particularly for ionospheric sounding. In addition, an increasing interest in the precise positioning with low-cost receivers is recognized. The number of low-cost GNSS receivers has been continuously increasing, especially with the growing number of cell phones that make single frequency GPS receivers with performance available for positioning (Gikas and Perakis 2016, Hernandez-Pajares et al. 2018). In future, it would be relevant to evaluate the capabilities of the proposed calibration method with low-cost cell phone data.

Although the calibration method requires less computational effort, it also requires external information, which was estimated using dual frequencies. Therefore, in order to estimate the TEC using exclusively single frequency data, a regional model to calibrate the single frequency GNSS measurements and derive TEC values was proposed in

Chapter 4. The regional model also confirmed the possibility to detect ionospheric plasma bubbles by single frequency TEC data in regions with high number of GNSS stations. The developed method was capable of diagnosing the spatial and temporal progress of ionospheric plasma bubbles in VTEC maps and keograms. The results were confirmed by comparing the estimated TEC depletions with accurate airglow images. In addition, it can be seen a good agreement between the STEC data obtained with dual and single frequency.

Finally, Chapter 5 presents an evaluation of the performance of the regional model based on single frequency measurements. The assessment is made by means of single frequency PPP, comparing the positioning results against the correction using dual-frequency GPS signals, as well as compared to the corrections provided by GIMs produced by IGS. As a result, the positioning performance using single frequency model presented similar accuracy to the dual frequency models and, at the same time, provided less observations affected by ionospheric scintillations. These results demonstrate the feasibility of using single frequency GNSS data to develop ionospheric models and to improve the positioning over low latitudes. In the future, the following investigations are recommended: (1) to perform an assessment of single frequency ionospheric models using other evaluation techniques, like using ionosonde data (Jerez et al. 2020) and dSTEC values (Hernadez-Pajares et al, 2017; Zhao et al. 2021) and (2) to perform the estimation of TEC single frequency uncertainties since they can provide an additional improvement in the single frequency PPP (Jerez et al. 2022), in particular for low latitude regions.

With the GNSS modernization program, the new frequencies present more complex signal structure with specific functionalities. Therefore, it would be interesting investigate the performance of the ionospheric model proposed for different channels/codes at L1 modernized signal (e.g., L1C(D), L1C(P), L1C(D+P), L1(Y), L1(M)).

The regional ionospheric model proposed was based on VTEC estimation, where the conversion between VTEC and STEC was performed through a mapping function related to satellite elevation and thin layer ionospheric height. In this conversion, the ionosphere is assumed to be an infinitely thin fixed-height layer, i.e., the ionospheric variation is not considered. As a future recommendation, it would be interesting to explore methods that consider the spatial variability of the ionosphere, both horizontally and vertically. In addition, it would be interesting to carry out future work to verify the possibility of adapting the developed method for real-time applications. Real-time approaches are highly relevant for GNSS positioning applications and space climate monitoring.

REFERENCES

AA E.; ZOU S.; EASTES R.; KARAN D. K.; ZHANG S. R.; ERICKSON P. J.; COSTER A. J. Coordinated ground-based and space-based observations of equatorial plasma bubbles. Journal of *Geophysical Research: Space Physics*, v. 125, n. 1, p. e2019JA027569, 2020. doi.org/10.1029/2019ja027569.

AARONS, J. Global morphology of ionospheric scintillations. *Proceedings of the IEEE*, v. 70, n. 4, p. 360-378, 1982. doi.org/10.1109/PROC.1982.12314

ABDU, M. A.; BATISTA, I. S.; TAKAHASHI, H.; MACDOUGALL, J.; SOBRAL, J. H.; MEDEIROS, A. F.; TRIVEDI, N. B. Magnetospheric disturbance induced equatorial plasma bubble development and dynamics: A case study in Brazilian sector. *Journal of Geophysical Research: Space Physics*, v. 108, n. A12, 2003. doi.org/10.1029/2002JA009721

ABDU, M. A.; ALAM KHERANI, E.; BATISTA, I. S.; DE PAULA, E. R.; FRITTS, D. C.; SOBRAL, J. H. A. Gravity wave initiation of equatorial spread F/plasma bubble irregularities based on observational data from the SpreadFEx campaign. In: *Annales Geophysicae*. Göttingen, Germany: Copernicus Publications, 2009. p. 2607-2622. doi.org/10.5194/angeo-27-2607-2009

ABDU, M. A.; BATISTA, I. S.; REINISCH, B. W.; MACDOUGALL, J. W.; KHERANI, E. A.; SOBRAL, J. H. A. Equatorial range spread F echoes from coherent backscatter, and irregularity growth processes, from conjugate point digital ionograms. *Radio Science*, v. 47, n. 06, p. 1-8, 2012 doi.org/10.1029/2012RS005002

ABDU, M. A. Electrodynamics of ionospheric weather over low latitudes. *Geoscience Letters*, v. 3, p. 1-13, 2016. doi.org/10.1186/s4056 2-016-0043-6

ANDRADE, L.S.; ALVES, D. B. M. Novas observáveis GPS e a melhoria na acurácia do posicionamento. *Revista Brasileira de Cartografia*, 68 (5), pp.991– 1004, 2016

AGYEI-YEBOAH E.; PAULINO, I.; MEDEIROS, A. F.; BURITI, R. A.; PAULINO, A. R.; LOMOTEY, S.O.; TAKAHASHI, H.; WRASSE, C. M. Seasonal variation of plasma bubbles during solar cycle 23–24 over the Brazilian equatorial region. *Advances in Space Research*, v. 64, n. 7, p. 1365-1374, 2019. doi.org/10.1016/j.asr.2019.06.041

ARAGON-ANGEL A.; ROVIRA-GARCIA, A.; ARCEDIANO-GARRIDO, E.; IBÁÑEZ-SEGURA, D. Galileo Ionospheric correction algorithm integration into the open-source GNSS Laboratory Tool Suite (gLAB). *Remote Sensing*, v. 13, n. 2, p. 191, 2021. doi.org/10.3390/rs13020191

ARIKAN, F. E. Z. A.; NAYIR, H.; SEZEN, U. M. U. T.; ARIKAN, O. Estimation of single station inter frequency receiver bias using GPS-TEC. *Radio Science*, v. 43, n. 04, p. 1-13, 2008. doi:10.1029/2007rs003785

Barros D, Takahashi H, Wrasse CM, Figueiredo CAO. (2018). Characteristics of equatorial plasma bubbles observed by TEC map based on ground-based GNSS receivers over South America. In *Annales geophysicae* (Vol. 36, No. 1, pp. 91-100). Göttingen, Germany: Copernicus Publications. doi.org/10.5194/angeo-36-91-2018

BARROS, D.; TAKAHASHI, H.; WRASSE, C. M.; FIGUEIREDO, C. A. O. Characteristics of equatorial plasma bubbles observed by TEC map based on ground-based GNSS receivers over South America. In: *Annales geophysicae*. Göttingen, Germany: Copernicus Publications, v. 36, n. 01, pp. 91-100, 2018. doi.org/10.5194/angeo-36-91-2018

BHATTACHARYYA, A. Equatorial plasma bubbles: a review. *Atmosphere*, v. 13, n. 10, p. 1637, 2022. doi.org/10.3390/atmos13101637

BRUNINI, C.; MEZA, A.; AZPILICUETA, F.; VAN ZELE, M.A.; GENDE, M.; DÍAZ, A. A new ionosphere monitoring technology based on GPS. *Astrophysics and space science,* v. 290, p. 415-429, 2004.

BURKE, W. J.; HUANG, C. Y.; Gentile, L. C.; Bauer, L. Seasonal-longitudinal variability of equatorial plasma bubbles. In: *Annales geophysicae*. Göttingen, Germany: Copernicus Publications, 2004. p. 3089-3098. doi:10.5194/angeo-22-3089-2004

CAMARGO, P.O.; MONICO, J. F. G.; FERREIRA, L. D. D. Application of ionospheric corrections in the equatorial region for L1 GPS users. *Earth, Planets and Space*, v. 52, p. 1083-1089, 2000.

CHRISTOVAM A. L.; PROL, F. S.; HERNANDEZ-PAJARES, M.; CAMARGO, P. O. Plasma bubble imaging by single-frequency GNSS measurements. *GPS Solutions*, v. 27, n. 3, p. 124, 2023. doi:10.1007/s10291-023-01463-z

CHRISTOVAM, A. L.; PROL, F. S.; JEREZ, G. O.; HERNANDEZ-PAJARES, M.; CAMARGO, P. O. PPP at low latitudes with ionospheric model exclusively based on single frequency GNSS measurements, 2023 (*Submitted to Space Weather*)

CIRAOLO, L.; AZPILICUETA, F.; BRUNINI, C.; MEZA, A.; RADICELLA, S. M. Calibration errors on experimental slant total electron content (TEC) determined with GPS. *Journal of Geodesy*, v. 81, p. 111–120, 2007. DOI 10.1007/s00190-006-0093-1

CONKER, R. S.; EL-ARINI; M. B.; HEGARTY, C. J.; HSIAO, T. Modeling the effects of ionospheric scintillation on GPS/satellite-based augmentation system availability. *Radio Science,* v. 38, n. 1, p. 1-1-1-23, 2003. doi.org/10.1029/2000RS002604.

COOPER, C.; MITCHELL, C. N.; WRIGHT, C. J.; JACKSON, D. R.; Witvliet, B. A. Measurement of ionospheric total electron content using single-frequency geostationary satellite observations. *Radio Science,* v. 54, n. 1, p. 10-19, 2019. doi.org/10.1029/2018RS006575

DELAY, S. H.; CARRANO, C. S.; GROVES, K. M.; DOHERTY, P. H. Statistical Analysis of GPS L1, L2, and L5 Tracking Performance During Ionospheric Scintillation. In: *Proceedings of the ION 2015 Pacific PNT Meeting*. 2015. p. 1-9.

DE PAULA E. R.; KHERANI, E. A.; ABDU, M.A.; BATISTA, I. S.; SOBRAL, J. H. A.; KANTOR, I. J.; TAKAHASHI, H.; REZENDE, L. F. C.; MUELLA, M. T. A. H.; RODRIGUES, F. S.; KINTNER, P. M.; LEDVINA, B. M.; MITCHELL, C.; GROVES, K. M. Characteristics of the ionospheric irregularities over Brazilian longitudinal sector, *Indian Journal of Radio Space*, 36:268–277, 2007.

EASTES, R.W.; SOLOMON, S. C.; DANIELL, R. E.; ANDERSON, D.N.; BURNS, A. G.; ENGLAND, S. L.; MARTINIS, C. R.; MCCLINTOCK, W. E. Global-scale observations of the equatorial ionization anomaly. *Geophysical Research Letters*, v. 46, n. 16, p. 9318-9326, 2019. doi.org/10.1029/2019GL084199

ENGEL, U. A theoretical performance analysis of the modernized GPS signals. *In: 2008 IEEE/ION Position, Location and Navigation Symposium*. IEEE, 2008. p. 1067-1078. doi.org/10.1109/PLANS.2008.4570114

ESTEY, L. H.; MEERTENS, C. M. TEQC: the multi-purpose toolkit for GPS/GLONASS data. *GPS solutions*, v. 3, n. 1, p. 42-49, 1999. doi.org/10.1007/PL00012778

FAGUNDES P.R.; PILLAT, V. G.; BOLZAN, M. J. A.; BECKER-GUEDES, F.; ABALDE, J. R.; ARANHA S. L. Observations of F layer electron density profiles modulated by planetary wave type oscillations in the equatorial ionospheric anomaly region. Journal of Geophysical Research: *Space Physics*, v. 110, n. A12, 2005. doi:10.1029/2005JA011115

FELTENS, J. Chapman profile approach for 3-D global TEC representation, IGS presentation. In: *Proceedings of the 1998 IGS analysis centers workshop*, ESOC, Darmstadt, Germany, 9–11 Feb 1998, pp 285–297. 1998

GEORGIADIOU, Y. Modelling the ionosphere for an active control network of GPS stations. In: LGR series 7. Delft: Delft Geodetic Computing Centre, 1994.

GIKAS, V.; PERAKIS, H. Rigorous performance evaluation of smartphone GNSS/IMU sensors for ITS applications. *Sensors*, v. 16, n. 8, p. 1240, 2016. doi.org/10.3390/s1608 1240

GOSS, A.; SCHMIDT, M.; ERDOGAN, E.; GÖRRES, B.; SEITZ, F. High-resolution vertical total electron content maps based on multi-scale b-spline representations. *Annales Geophysicae*, *37*(4), p. 699–717, 2019. https://doi.org/10.5194/angeo-37-699-2019

GOSS, A.; HERNÁNDEZ-PAJARES, M.; SCHMIDT, M.; ROMA-DOLLASE, D.; ERDOGAN, E.; SEITZ, F. High-resolution ionosphere corrections for single-frequency positioning. *Remote Sensing*, v. 13, n. 1, p. 12, 2020. https://doi.org/10.3390/rs13010012

GUO, K.; AQUINO, M.; VADAKKE VEETTIL, S. Ionospheric scintillation intensity fading characteristics and GPS receiver tracking performance at low latitudes. *GPS Solutions*, v. 23, p. 1-12, 2019. https://doi.org/10.1007/s10291-019-0835-1

GUO, K.; AQUINO, M.; VADAKKE VEETTIL, S. Effects of GNSS receiver tuning on the PLL tracking jitter estimation in the presence of ionospheric scintillation. *Space Weather*, v. 18, n. 7, 2020. doi.org/10.1029/2019SW002362

HAASE, J.S.; DAUTERMANN, T.; TAYLOR, M. J.; CHAPAGAIN, N.; CALAIS, E.; PAUTET, D. Propagation of plasma bubbles observed in Brazil from GPS and airglow data. *Advances in Space Research*, v. 47, n. 10, p. 1758-1776, 2010. doi:10.1016/j.asr.2010.09.025

HEIN, W.Z.; GOTO, Y.; KASAHARA, Y. Estimation method of ionospheric TEC distribution using single frequency measurements of GPS signals. *International Journal of Advanced Computer Science and Applications*, v. 7, n. 12, 2016. doi:10.14569/ijacsa.2016.071201

HEGARTY, C.; EL-ARINI, M.B.; KIM, T.; ERICSON, S. Scintillation modeling for GPS-wide area augmentation system receivers. *Radio Science,* v. 36, n. 5, p. 1221-1231, 2001. doi.org/10.1029/1999RS002425.

HERNÁNDEZ-PAJARES, M.; JUAN, J. M.; SANZ, J. New approaches in global ionospheric determination using ground GPS data. *Journal of Atmospheric and Solar-Terrestrial Physics,* v. 61, n. 16, p. 1237-1247, 1999. doi.org/10.1016/S1364-6826(99)00054-1

HERNÁNDEZ-PAJARES, M.; JUAN, J.M.; SANZ, J.; ORUS, R.; GARCIA-RIGO, A.; FELTENS, J. The IGS VTEC maps: a reliable source of ionospheric information since 1998. *Journal of Geodesy,* v. 83, p. 263-275, 2009. doi.org 10.1007/s00190-008-0266-1

HERNÁNDEZ-PAJARES, M.; ARAGÓN-ÁNGEL À.; DEFRAIGNE P.; BERGEOT N., PRIETO-CERDEIRA R., GARCÉA-RIGO A. Distribution and mitigation of higher-order ionospheric effects on precise GNSS processing. *Journal of Geophysical Research: Solid Earth*, v. 119, n. 4, p. 3823-3837, 2014. doi:10.1002/2013JB010568.

HERNÁNDEZ-PAJARES, M.; ROMA-DOLLASE, D.; KRANKOWSKI, A.; GARCÍA-RIGO, A.; ORÚS-PÉREZ, R. Methodology and consistency of slant and vertical assessments for ionospheric electron content models. *Journal of Geodesy*, v. 91, n. 12, p. 1405-1414, 2017. doi.org/10.1007/s00190-017-1032-z

HERNÁNDEZ-PAJARES, M.; ROMA-DOLLASE, D.; GARCIA-FERNÀNDEZ, M.; ORUS-PEREZ, R.; GARCÍA-RIGO, A. Precise ionospheric electron content monitoring from single-frequency GPS receivers. *GPS solutions,* v. 22, n. 4, p. 102, 2018. doi.org/10.1007/s10291-018-0767-1

JEREZ G. O.; HERNÁNDEZ-PAJARES, M.; GOSS, A.; DA SILVA, C. M.; ALVES, D. B.; MONICO, J. F. G. Impact and synergies of GIM error estimates on the VTEC interpolation and single-frequency PPP at low latitude region. *GPS Solutions*, v. 26, n. 2, p. 40, 2022. doi.org/10.1007/s10291-022-01228-0

JEREZ, G. O.; HERNÁNDEZ-PAJARES, M.; PROL, F. S.; ALVES, D. B.; MONICO J. F. G. Assessment of global ionospheric maps performance by means of ionosonde data. *Remote sensing*, v. 12, n. 20, p. 3452, 2020. https://doi.org/10.3390/rs12203452

JEREZ, G. O.; HERNÁNDEZ-PAJARES, M.; GOSS, A.; PROL, F. S.; ALVES, D. B. M.; MONICO J. F. G.; SCHMIDT, M. Two-way assessment of ionospheric maps performance over the Brazilian region: Global versus regional products. *Space Weather*, v. 21, n. 2, 2023. doi.org/10.1029/2022SW003252

KARAN, D. K.; DANIELL, R. E.; ENGLAND, S. L.; MARTINIS, C. R.; EASTES, R. W.; BURNS, A. G.; MCCLINTOCK, W. E. First zonal drift velocity measurement of Equatorial Plasma Bubbles (EPBs) from a geostationary orbit using GOLD data. *Journal of Geophysical Research: Space Physics*, v. 125, n. 9, 2020. https://doi.org/10.1029/2020JA02817.

KELLEY, M. C. The Earth's Ionosphere*: Plasma Physics & Electrodynamics*. 2. ed. Ithaca: Academic Press, 2009. 556 p.

LEE C. C.; SU, S. Y.; REINISCH, B. W. Concurrent study of bottomside spread F and plasma bubble events in the equatorial ionosphere during solar maximum using digisonde and ROCSAT-1. *In Annales Geophysicae*. Göttingen, Germany: Copernicus Publications, p. 3473-3480, 2005. https://doi.org/10.5194/angeo-23-3473-2005

LEICK, A. *GPS Satellite Surveying*, 3rd ed., John Wiley & Sons, Inc, p. 464, ISBN 0-471-05930-7, 2004.

LI, Z.; YUAN, Y.; WANG, N.; HERNANDEZ-PAJARES, M.; HUO, X. SHPTS: towards a new method for generating precise global ionospheric TEC map based on spherical harmonic and generalized trigonometric series functions. *Journal of Geodesy*, v. 89, p. 331-345, 2015. doi:10.1007/s00190-014-0778-9

LI, G.; NING, B.; OTSUKA, Y.; ABDU, M. A.; ABADI, P.; LIU, Z.; WAN, W. Challenges to equatorial plasma bubble and ionospheric scintillation short-term forecasting and future aspects in east and southeast Asia. *Surveys in Geophysics*, v. 42, p. 201-238, 2021. doi.org/10.1007/s10712-020-09613-5

LIU, K.; LI, G.; NING, B.; HU, L.; LI, H. Statistical characteristics of low-latitude ionospheric scintillation over China, *Advances in Space Research*, v. 55, n. 5, p. 1356-1365, 2015. https://doi.org/10.1016/j.asr.2014.12.001

MACHO, E. P.; CORREIA, E.; SPOGLI, L.; MUELLA, M. T. D. A. H. Climatology of ionospheric amplitude scintillation on GNSS signals at south American sector during solar cycle 24. *Journal of Atmospheric and Solar-Terrestrial Physics*, v. 231, p. 105872, 2022. doi.org/10.1016/j.jastp.2022.105872

MAKELA, J. J.; LEDVINA, B. M.; KELLEY, M. C.; KINTNER, P. M. Analysis of the seasonal variations of equatorial plasma bubble occurrence observed from Haleakala, Hawaii. In: *Annales Geophysicae*. p. 3109-3121, 2004. https://doi.org/10.5194/angeo-22-3109-2004, 2004

MANNUCCI, A. J.; WILSON, B. D.; EDWARDS, C. D. A. New Method for Monitoring the Earth's Ionospheric Total Electron Content Using the GPS Global Network, *Proceedings of the 6th International Technical Meeting of the Satellite Division of The Institute of Navigation (ION GPS 1993)*, Salt Lake City, UT, pp. 1323-1332, 1993.

MANNUCCI, A. J.; WILSON, B. D.; YUAN, D. N.; HO, C. H.; LINDQWISTER, U. J.; RUNGE, T. F. A global mapping technique for GPS-derived ionospheric total electron content measurements. *Radio science*, v. 33, n. 3, p. 565-582, 1998. doi.org/10.1029/97RS02707

MONTENBRUCK, O; HAUSCHILD, A.; STEIGENBERGER, P. Differential code bias estimation using multi-GNSS observations and global ionosphere maps. *Navigation: Journal of the Institute of Navigation,* v. 61, n. 3, p. 191-201, 2014. doi.org/10.1002/navi.64

MORAES, A. O.; COSTA, E.; ABDU, M. A.; RODRIGUES, F. S.; DE PAULA, E. R.; OLIVEIRA, K., PERRELLA, W. J. The variability of low-latitude ionospheric amplitude and phase scintillation detected by a triple-frequency GPS receiver. *Radio Science*, v. 52, n. 4, p. 439-460, 2017. doi:10.1002/2016RS006165

MORAES, A. O.; VANI, B. C.; COSTA, E.; ABDU, M. A.; DE PAULA, E. R.; SOUSASANTOS, J.; SHIMABUKURO, M. H. GPS availability and positioning issues when the signal paths are aligned with ionospheric plasma bubbles. *GPS Solutions,* v. 22, p. 1-12, 2018. doi.org/10.1007/s10291-018-0760-8.

MUELLA, M. T. A. H.; DUARTE-SILVA, M. H.; MORAES, A. O.; DE PAULA, E. R.; DE REZENDE, L. F. C.; ALFONSI, L.; AFFONSO, B. J. Climatology and modeling of ionospheric scintillations and irregularity zonal drifts at the equatorial anomaly crest region. In: *Annales Geophysicae*, p. 1201-1218, 2017. doi.org/10.5194/angeo -35-1201-2017

NIE, W.; XU, T.; ROVIRA-GARCIA, A.; JUAN ZORNOZA, J. M.; SANZ SUBIRANA, J.; GONZÁLEZ-CASADO, G.; XU, G. Revisit the calibration errors on experimental slant total electron content (TEC) determined with GPS. *GPS solutions*, v. 22, n. 3, p. 85, 2018. doi.org/10.1007/s10291-018-0753-7

NISHIOKA, M.; SAITO, A.; TSUGAWA, T. Occurrence characteristics of plasma bubble derived from global ground-based GPS receiver networks. *Journal of Geophysical* Research: Space Physics, v. 113, n. A5, 2008. doi:10.1029/2007ja012605

OLIVEIRA, C. B. A. D.; ESPEJO, T. M. S.; MORAES A. O.; COSTA, E.; SOUSASANTOS, J.; LOURENCO, L. F. D.; ABDU, M. A. Analysis of plasma bubble signatures in total electron content maps of the low-latitude ionosphere: A simplified methodology. *Surveys in geophysics,* v. 41, n. 4, p. 897-931, 2020. https://doi:10.1007/s10712-020-09584-7.

PENG, S.; MORTON, Y.; PELGRUM, W.; VAN GRAAS, F. High latitude ionosphere scintillations at GPS L5 band. In: *Proceedings of the 24th International Technical Meeting of the Satellite Division of The Institute of Navigation (ION GNSS 2011). p. 597-607, 2011*.

PROL, F. S.; CAMARGO, P. O. Estimativa da tendência diferencial do código nos receptores GNSS. *Boletim de Ciências Geodésicas*, v. 20, p. 735-749, 2014. doi.org/10.1590/S1982-21702014000400042

PROL F. S.; CAMARGO, P. O.; MONICO J. F. G.; MUELLA, M. T. D. A. H. Assessment of a TEC calibration procedure by single-frequency PPP. *GPS Solutions*, v. 22, p. 1-11, 2018a. doi.org/10.1007/s10291-018-0701-6

PROL, F.S.; HERNANDÉZ-PAJARES, M.; MUELLA, M. T. A. H.; CAMARGO, P. O. Tomographic imaging of ionospheric plasma bubbles based on GNSS and radio occultation measurements. *Remote Sensing*, v. 10, n. 10, p. 1529, 2018b. https://doi:10.3390/rs10101529.

ROMA-DOLLASE, D.; HERNÁNDEZ-PAJARES, M.; KRANKOWSKI, A; KOTULAK, K.; GHODDOUSI-FARD, R.; YUAN, Y.; GÓMEZ-CAMA, J. M. Consistency of seven different GNSS global ionospheric mapping techniques during one solar cycle. *Journal of Geodesy*, v. 92, p. 691-706, 2018. https://doi.org/10.1007/s00190-017-1088-9

ROVIRA-GARCIA, A.; IBÁÑEZ-SEGURA, D.; ORÚS-PEREZ, R.; JUAN, J. M.; SANZ, J.; GONZÁLEZ-CASADO, G. Assessing the quality of ionospheric models through GNSS positioning error: methodology and results. *GPS solutions*, v. 24, n. 1, p. 4, 2020. doi.org/10.1007/s10291-019-0918-z

SAHAI, Y.; FAGUNDES, P. R.; BITTENCOURT, J. A. F-region ionospheric plasma bubbles: solar cycle effects. *Journal of Atmospheric and Solar-Terrestrial Physics,* v. 62, n. 15, p. 1377-1383, 2000.

SCHAER, S.; BEUTLER, G.; ROTHACHER, M.; SPRINGER, T. A. Daily global ionosphere maps based on GPS carrier phase data routinely produced by the CODE Analysis Center, In: *Proceedings of the IGS AC Workshop, Silver Spring, MD, USA*. p. 181-192. 1996.

SCHAER, S.; GURTNER, W.; FELTENS, J. IONEX: The ionosphere map exchange format version 1. In: *Proceedings of the IGS AC workshop, Darmstadt, Germany*. 1998.

SCHAER, S. *Mapping and predicting the Earth's ionosphere using the Global Positioning System*. 205 p. Tese (Doutorado) — University of Berne, Berne, 1999.

SCHÜLER, T.; OLADIPO, O. A. Single-frequency GNSS retrieval of vertical total electron content (VTEC) with GPS L1 and Galileo E5 measurements. *Journal of Space Weather and Space Climate*, v. 3, p. A11, 2013. doi.org/10.1051/swsc/2013033

SEEBER, G. Satellite Geodesy: foundations, methods and applications. 2. ed. Berlin: Walter de Gruyter, 2003. 589 p.

SKONE, S.; KNUDSEN, K.; DE JONG, M. Limitations in GPS receiver tracking performance under ionospheric scintillation conditions. *Physics and Chemistry of the Earth, Part A: Solid Earth and Geodesy*, v. 26, n. 6-8, p. 613-621, 2001. doi.org/10.1016/S1464-1895(01)00110-7

SOBRAL, J. H. A.; ABDU, M. A.; SAHAI, Y. Equatorial plasma bubble eastward velocity characteristics from scanning airglow photometer measurements over Cachoeira Paulista. *Journal of atmospheric and terrestrial physics*, v. 47, n. 8-10, p. 895-900, 1985.

SPOGLI, L.; ALFONSI, L.; ROMANO, V.; DE FRANCESCHI, G.; MONICO, J. F. G.; SHIMABUKURO, M. H.; AQUINO, M. Assessing the GNSS scintillation climate over Brazil under increasing solar activity. *Journal of Atmospheric and Solar-Terrestrial Physics*, v. 105, p. 199-206, 2013. doi.org/10.1016/j.jastp.2013.10.003

SPOGLI, L.; CESARONI, C.; DI MAURO, D.; PEZZOPANE, M.; ALFONSI, L.; MUSICÒ, E.; FLOURY, N. Formation of ionospheric irregularities over Southeast Asia during the 2015 St. Patrick's Day storm. *Journal of Geophysical Research: Space Physics*, v. 121, n. 12, p. 12,211-12,233, 2016. doi.org/10.1002/2016ja023222

SOUSASANTOS, J.; MORAES, A. O.; SOBRAL, J. H. A.; MUELLA, M. T. A. H.; DE PAULA, E. R.; PAOLINI, R. S. Climatology of the scintillation onset over southern Brazil. I In: *Annales Geophysicae. Göttingen*. p. 565-576, 2018. doi.org/10.5194/angeo-36-565-2018

SOUZA, A. L. C.; CAMARGO, P. O.; MUELLA, M. T. A. H.; TARDELLI-COELHO, F. Drift velocity estimation of ionospheric bubbles using GNSS observations. *Radio Science*, v. 56, n. 8, p. 1-18, 2021. doi.org/10.1029/2020RS007220

SOUZA, A. L. C.; JEREZ, G. O.; CAMARGO, P. D. O.; ALVES, D. B. M. Assessment of GPS positioning performance using different signals in the context of ionospheric scintillation: a month-long case study on São José dos Campos, Brazil. *Boletim de Ciências Geodésicas*, v. 28, 2022. doi.org/10.1590/s1982-2170202200040001

SREEJA, V.; AQUINO, M.; ELMAS, Z. G.; FORTE, B. Correlation analysis between ionospheric scintillation levels and receiver tracking performance. *Space Weather,* v. 10, n. 6, 2012. doi.org/10.1029/2012SW000769

TAKAHASHI, H.; WRASSE, C. M.; OTSUKA, Y.; IVO, A.; GOMES, V.; PAULINO, I.; SHIOKAWA, K. Plasma bubble monitoring by TEC map and 630 nm airglow image. *Journal of Atmospheric and Solar-Terrestrial Physics,* v. 130, p. 151-158, 2015. doi:10.1016/j.jastp.2015.06.003.

TAKAHASHI, H.; WRASSE, C. M.; DENARDINI, C. M.; PÁDUA, M. B.; DE PAULA, E. R.; COSTA, S. M. A.; SANT'ANNA, N. Ionospheric TEC weather map over South America. *Space Weather*, v. 14, n. 11, p. 937-949, 2016. doi.org/10.1002/2016SW001474

TAKASU, T.; YASUDA, A. Development of the low-cost RTK-GPS receiver with an open source program package RTKLIB. In: *International symposium on GPS/GNSS,* p. 1-6, 2009.

TERRA, P. M.; SOBRAL, J. H. A.; ABDU, M. A.; SOUZA, J. R.; TAKAHASHI, H. Plasma bubble zonal velocity variations with solar activity in the Brazilian region. In: *Annales Geophysicae.*, p. 3123-3128, 2004. doi.org/10.5194/angeo-22-3123-2004, 2004.

TEUNISSEN P.; MONTENBRUCK O. *Handbook of Global Navigation Satellite Systems*, Springer, Switzerland, 2017. 1335 p. doi.org/10.1007/978-3-319-42928-1

TSUNODA, R. T. Time evolution and dynamics of equatorial backscatter plumes 1. Growth phase. *Journal of Geophysical Research: Space Physics*, v. 86, n. A1, p. 139-149, 1981.

TONGKASEM, N.; MYINT, L. M. M.; SUPNITHI, P. Estimation and Validation of Ionospheric Delay using Standalone Single-Frequency observations. *IEEE Access*, v. 10, p. 103485-103495, 2022. https://doi: 10.1109/ACCESS.2022.3208102

VADAKKE VEETTIL, S.; AQUINO, M.; MARQUES, H. A.; MORAES, A. O. Mitigation of ionospheric scintillation effects on GNSS precise point positioning (PPP) at low latitudes. *Journal of Geodesy,* v. 94, n. 2, p. 15, 2020. doi.org/10.1007/s00190-020-01345-z

VANI, B.C.; SHIMABUKURO, M. H.; MONICO, J. F. G. Visual exploration and analysis of ionospheric scintillation monitoring data: The ISMR Query Tool. *Computers & Geosciences*, v. 104, p. 125-134, 2017. https://doi.org/10.1016/j.cageo.2016.08.022.

VANI, B. C.; FORTE, B.; MONICO, J. F. G.; SKONE, S.; SHIMABUKURO, M. H.; MORAES, A. O.; MARQUES, H. A. A novel approach to improve GNSS Precise Point Positioning during strong ionospheric scintillation: Theory and demonstration. IEEE Transactions on *Vehicular Technology,* v. 68, n. 5, p. 4391-4403, 2019. doi: 10.1109/TVT.2019.2903988.

XIA, R. Determination of absolute ionospheric error using a single frequency GPS receiver, In: *Proceedings of the 5th international technical meeting of the satellite division of the institute of navigation* (ION GPS 1992). 1992. p. 483-490.

XIONG, C.; STOLLE, C.; LÜHR, H. The Swarm satellite loss of GPS signal and its relation to ionospheric plasma irregularities. *Space Weather*, v. 14, n. 8, p. 563-577, 2016. doi.org/10.1002/2016SW001439

ZHAO, J.; HERNÁNDEZ-PAJARES, M.; LI, Z.; WANG, N.; YUAN, H. Integrity investigation of global ionospheric TEC maps for high-precision positioning. *Journal of Geodesy*, v. 95, p. 1-15, 2021. doi.org/10.1007/s00190-021-01487-8

YEH, K. C.; LIU, C. H. Radio wave scintillations in the ionosphere. *Proceedings of the IEEE*, v. 70, n. 4, p. 324-360, 1982. doi.org/10.1109/PROC.1982.12313

YUNCK, T. P. Coping with the atmosphere and ionosphere in precise satellite and ground positioning. In: *Environmental Effects on Spacecraft Positioning and Trajectories*, ed. by A.V. Jones (AGU, Washington) pp. 1–16, 1992.

WALTER, T. Effect of ionospheric scintillations on GNSS—a white paper. SBAS Ionospheric Working Group, 2010.

WILD, U. Ionosphere and satellite systems: permanent GPS tracking data for modelling and monitoring. *Geod-Geophys*. Arb. Schweiz, v. 48, 1994.

ZOLESI, B.; CANDER, L. R. *Ionospheric Prediction and Forecasting*. Berlin, Heidelberg: Springer Berlin Heidelberg. 2014. https://doi.org/10.1007/978-3-642-38430-1.